



Bruno Fernando Abreu de Melo

**Tweezers and Cavities: developing tools for an
Optomechanics Laboratory**

Dissertação de Mestrado

Dissertation presented to the Programa de Pós-Graduação em Física of PUC-Rio in partial fulfillment of the requirements for the degree of Mestre em Ciências – Física.

Advisor: Prof. Thiago Barbosa dos Santos Guerreiro

Rio de Janeiro
October 2019



Bruno Fernando Abreu de Melo

**Tweezers and Cavities: developing tools for an
Optomechanics Laboratory**

Dissertation presented to the Programa de Pós-Graduação em Física of PUC-Rio in partial fulfillment of the requirements for the degree of Mestre em Ciências – Física. Approved by the Examination Committee.

Prof. Thiago Barbosa dos Santos Guerreiro

Advisor

Departamento de Física PUC-Rio

Prof. Rodrigo Prioli Menezes

Departamento de Física – PUC-Rio

Prof. Antonio Zelaquett Khoury

UFF

Rio de Janeiro, October 24th, 2019

All rights reserved.

Bruno Fernando Abreu de Melo

Graduated in Electrical Engineering from Instituto Militar de Engenharia in 2017.

Bibliographic data

Melo, Bruno Fernando Abreu de

Tweezers and Cavities: developing tools for an Optomechanics Laboratory / Bruno Fernando Abreu de Melo; advisor: Thiago Barbosa dos Santos Guerreiro. – Rio de Janeiro: PUC-Rio, Departamento de Física, 2019.

v., 104 f: il. color. ; 30 cm

Dissertação (mestrado) - Pontifícia Universidade Católica do Rio de Janeiro, Departamento de Física.

Inclui bibliografia

1. Física – Teses. 2. Optomecânica – Teses. 3. Optomecânica;. 4. Feixes Gaussianos;. 5. Cavidades Ópticas;. 6. Pinças Ópticas;.

I. Guerreiro, Thiago Barbosa dos Santos. II. Pontifícia Universidade Católica do Rio de Janeiro. Departamento de Física. III. Título.

CDD: 530

Acknowledgments

Firstly, I would like to thank my advisor Thiago Guerreiro, who convinced me to give experimental physics a chance. With endless patience, he took the time to teach me everything from the beginning, until I could take the first steps by myself, and was always willing to help whenever there was an obstacle. Today, I can't think of a job that I would enjoy more than being an experimental physicist. For all of that, I'm truly grateful.

I would also like to thank the other professors for teaching me what I needed to learn in order to transition from an engineer to a physicist. In particular, I would like to thank Carla, who is directly responsible for the existence of this dissertation. I learnt a lot while writing it, so I'm thankful for her advices.

I would like to thank the administrative staff of the physics department. Without them, there is no department. In special, I would like to thank Giza, for being very patient with me and helping me whenever I needed.

I would like to thank Paulo Americo group, from UFRJ, and Antonio Zelaquett group, from UFF, for helping us with our research. Specially, I would like to thank Rafael and Luís, who contributed to this dissertation with equipments and, most importantly, with ideas.

I would like to thank my friends from IME who, despite being far away from Rio, some even in the jungle, can always find a way to make me laugh even in the toughest days. I would also like to thank my other friends. Although I can't be with them as much as I want to, I carry them with me, and having them in my life gives me the strength to carry on.

I would also like to thank my mother for the unconditional support throughout my entire life and, specially, throughout this work. I wouldn't have got here if it wasn't for her and for Rubinho, who was always there for me, not only as a father, but also as a friend.

I would like to thank my sister, for teaching me that studying can be fun and rewarding. Looking up to her developed in me the passion for numbers and, ultimately, led me to where I am right now. Along the same lines, I would like to thank my father for teaching me how to be curious about everything that surround us, and how interesting everything can be.

Finally, I would like to thank Costa, who supported me when I first considered studying for the IME/ITA exams. That was not only the start of my journey to IME, but was also the seed that grew into the love for physics that I now have and that is the reason why I completed this work.

I love physics and I love you all.

Thank you.

This study was financed in part by the Coordenação de Aperfeiçoamento de Pessoal de Nível Superior - Brasil (CAPES) - Finance Code 001. I would also like to thank the Conselho Nacional de Desenvolvimento Científico e Tecnológico (CNPq), the Fundação de Amparo à Pesquisa do Estado do Rio de Janeiro (FAPERJ) and Serrapilheira for also financing this study.

Abstract

Melo, Bruno Fernando Abreu de; Guerreiro, Thiago Barbosa dos Santos (Advisor). **Tweezers and Cavities: developing tools for an Optomechanics Laboratory**. Rio de Janeiro, 2019. 104p. Dissertação de Mestrado – Departamento de Física, Pontifícia Universidade Católica do Rio de Janeiro.

Optomechanics is a growing field that studies systems where light and mechanical motion are coupled via radiation pressure. In this work, we present the basic theory regarding optical cavities and optical tweezers, two important tools that are often used in optomechanical setups, as well as their experimental implementations. On the subject of optical cavities, we present the implementation of Fabry P erot cavities formed by one plane mirror and one spherical mirror and cavities formed by two spherical mirrors, both on the confocal and on the non-confocal configuration, and compare the performance of these different cavities. On the subject of optical tweezers, we present an optical tweezer capable of trapping micro-spheres in a water medium and use it to study the movement of trapped particles.

Keywords

Optomechanics; Gaussian Beams; Optical Cavities; Optical Tweezers;

Resumo

Melo, Bruno Fernando Abreu de; Guerreiro, Thiago Barbosa dos Santos. **Pinças e Cavidades: desenvolvendo ferramentas para um Laboratório de Optomecânica**. Rio de Janeiro, 2019. 104p. Dissertação de Mestrado – Departamento de Física, Pontifícia Universidade Católica do Rio de Janeiro.

A optomecânica é um campo em crescimento que estuda sistemas nos quais luz e movimento mecânico estão acoplados por meio de pressão de radiação. Neste trabalho apresentamos a teoria básica acerca de cavidades ópticas e pinças ópticas, duas importantes ferramentas frequentemente utilizadas em experimentos de optomecânica, bem como suas implementações práticas. No que diz respeito a cavidades ópticas, nós apresentamos a implementação de cavidades de Fabry Péroto formadas por um espelho plano e um espelho esférico e de cavidades formadas por dois espelhos esféricos, tanto na configuração confocal como na configuração não confocal, e comparamos a performance dessas diferentes cavidades. No que diz respeito a pinças ópticas, nós apresentamos uma pinça óptica capaz de aprisionar esferas micrométricas em um meio aquoso e a usamos para estudar o movimento de partículas aprisionadas.

Palavras-chave

Optomecânica; Feixes Gaussianos; Cavidades Ópticas; Pinças Ópticas;

Table of contents

1	Introduction	15
2	Gaussian beams and their propagation	19
2.1	The paraxial approximation	19
2.1.1	Gaussian Beams	19
2.1.2	Higher order transverse modes	23
2.2	Beam propagation through optical elements	25
2.2.1	ABCD matrix and the q parameter	25
2.2.2	ABCD calculation example	28
2.2.3	Beam collimation theory	29
2.2.4	Collimated beams in the laboratory	30
3	Optical cavities	33
3.1	The plane mirror optical cavity	33
3.1.1	Transmission and reflection coefficients	34
3.1.2	Important cavity parameters	35
3.1.3	Losses in the cavity	36
3.2	Gaussian beams and optical cavities	37
3.2.1	Cavity Modematching	38
3.2.2	Higher order modes resonance	40
4	Optical Cavities: Experiment	44
4.1	General aspects	45
4.1.1	Theory extensions	45
4.1.2	Experimental procedure	47
4.2	Plano-Concave cavity	49
4.3	Concave-concave cavity	54
4.4	Confocal cavity	56
4.4.1	Discussions	60
5	Optical Tweezers	62
5.1	Geometrical Optics Approximation	62
5.2	Dipole Approximation	65
5.2.1	Forces on an electric dipole	65
5.2.2	Numerical simulations for the dipole approximation	67
5.3	The intermediate regime	69
5.3.1	Generalized Mie theory	69
5.3.2	Numerical simulations for the intermediate regime	70
5.4	Trapped Particle Motion	72
5.4.1	Equations of motion for a trapped particle	72
5.4.2	Autocorrelation analysis of the trapped motion	74
5.4.3	Power Spectral Density	76
6	Optical Tweezers: Experiment	78

6.1	General Aspects	79
6.1.1	Real position measurements	79
6.1.2	Experimental procedure	81
6.2	Initial tests	84
6.3	Position Measurements	86
6.3.1	Power Spectral Density Analysis	86
6.3.2	Autocorrelation Function Analysis	88
6.3.3	Discussions	90
7	Conclusions and Perspectives	91
	Bibliography	98

List of figures

Figure 1.1	Conceptual schematics of our proposed optomechanical force sensor.	16
Figure 2.1	Transverse intensity profile for the Gaussian mode at $z = 0$.	22
Figure 2.2	Longitudinal profile of a Gaussian beam, defined as the beam width outline.	22
Figure 2.3	Transverse intensity profile for higher-order beams: (a) Hermite-Gauss beams; (b) Laguerre-Gauss beams.	24
Figure 2.4	Parameters h and θ for light rays in geometric optics: (a) definition of the parameters; (b) change in the parameters when the ray passes through a generic optical element.	26
Figure 2.5	Geometric laws used to derive the $ABCD$ matrices.	27
Figure 2.6	$ABCD$ matrices for four different optical elements.	28
Figure 2.7	Transformation of a beam by a thin lens of focal distance f positioned at z_L . The beam location is z_0 before the lens and z after the lens.	29
Figure 2.8	Theoretical collimation of a beam: (a) waist location as a function of the position of the lens; (b) waist size as a function of the position of the lens.	30
Figure 2.9	Approximations involving collimated beams: (a) transformation of a beam's waist; (b) transformation of collimated waist (telescope configuration).	31
Figure 3.1	Multiple reflection of a plane wave inside a plane mirror cavity. The rays are displayed at a slight angle with the mirror's normal in order to help visualization.	33
Figure 3.2	Spectra for a plane mirror cavity: (a) transmission spectrum; (b) reflection spectrum.	35
Figure 3.3	Transmission and reflection spectra for cavities formed by mirrors having the same loss coefficient, but different reflectances.	37
Figure 3.4	Representation of optical cavities as infinite arrays of lenses. Spherical mirrors are represented by thin lenses, while plane mirrors are represented as thin plates.	38
Figure 3.5	Cavity's waist as a function of the cavity's length.	40
Figure 3.6	Representation of misalignment situations: (a) misalignment between two spherical mirrors, implying a new cavity axis; (b) misalignment between the beam and the cavity axis.	42
Figure 4.1	Schematic of the setup implemented in our laboratory in order to study different types of cavities.	44
Figure 4.2	Initial steps for the implementation of the optical cavities. (a) Optical elements corresponding to Part I of Figure 4.1 (b) Measurement of the beam's waist and its location by the knife edging method.	47

- Figure 4.3 Optical elements corresponding to Part II of Figure 4.1.
 (a) Optical elements used to monitor the field transmitted by the cavity. (b) Cavity's mirrors are replaced by irises during the alignment procedure. (c) Implemented optical cavity. 48
- Figure 4.4 Complete optical setup used in the implementation of our optical cavities. 49
- Figure 4.5 Schematic showing the coordinates and parameters used in the modematching calculation. (a) Parameter q_0 at the coordinate z_0 of the beam waist. (b) Parameter q before and after a plane mirror of thickness d . 50
- Figure 4.6 Transmission and reflection spectra for the plano-concave cavity. (a) Plano-concave cavity's single transmission peak. (b) Plano-concave cavity's single reflection valley. (c) Plano-concave cavity's consecutive transmission peaks. (d) Transmission and reflection spectra for the plano-concave cavity. 51
- Figure 4.7 Cavity transmission patterns when the cavity is horizontally misaligned and the voltage is scanned around different resonant voltages. (a) Cavity transmission pattern corresponding to the fundamental mode. (b) Cavity transmission pattern corresponding to the $m = 1, n = 0$ Hermite-Gauss mode. 53
- Figure 4.8 Transmission and reflection spectra for the concave-concave cavity. (a) Concave-concave cavity's single transmission peak. (b) Concave-concave cavity's single reflection valley. (c) Concave-concave cavity's consecutive transmission peaks. (d) Transmission peaks corresponding to the resonance of the fundamental mode and a higher order mode in the concave-concave cavity. 56
- Figure 4.9 Transmission peaks for: (a) and (c) aligned confocal cavity; (b) and (d) misaligned confocal cavity. 58
- Figure 4.10 Comparison between the shape of transmission peaks when the cavity's length is varied. Confocal cavity's transmission peak when the cavity's length: (a) is greater than $2R$; (b) is equal to $2R$; (c) is less than $2R$. 59
- Figure 4.11 Confocal cavity's transmission pattern under different situations. (a) Transmission pattern when the cavity is aligned. (b) First type of transmission pattern when the cavity is misaligned. (c) Second type of transmission pattern when the cavity is misaligned. 59
- Figure 4.12 Possible configurations integrating a membrane to a Fabry-Pérot cavity: (a) Membrane acting as one of the cavity's mirrors; (b) Plano-concave analogous of the *membrane in the middle* configuration; (c) Membrane positioned in the middle of a cavity (*Membrane in the middle* configuration). 61
- Figure 5.1 Schematic of an optical tweezer, showing an objective lens focusing a laser beam, causing a sphere to be trapped at the focal region. 62

- Figure 5.2 Refraction of light rays (red arrows) by a sphere under the geometrical optics approximation and the forces generated by it (green arrows) when: (a) the sphere is at the focus; (b) the sphere laterally displaced; (c) the sphere is vertically displaced. The green arrows indicate the force acting on the sphere. 63
- Figure 5.3 Multiple reflections and refractions of a light ray that hits a sphere. 64
- Figure 5.4 Dipole approximation: (a) force in the z direction; (b) potential in the z direction. 67
- Figure 5.5 Dipole approximation: (a) force in the x direction; (b) potential in the x direction. 69
- Figure 5.6 Forces in the z and x direction under the intermediate regime for a particle trapped in: (a) and (b) water; (c) and (d) air. Aside from the medium's refractive index, all other parameters are the same. 71
- Figure 5.7 Minimum force in the z direction as a function of the sphere's radius for : (a) spheres trapped in air by beams having different numerical apertures; (b) spheres made of different materials trapped in water. 72
- Figure 5.8 Brownian motion simulation considering the existence of a harmonic force around the origin: (a) the first hundred points of the simulation; (b) all of the fifty thousand points of the simulation 74
- Figure 5.9 Comparison between the ACF calculated using the points from the previous simulation and the ACF predicted by the theory: (a) first 0.2 seconds; (b) first 0.01 seconds. 75
- Figure 5.10 PSD calculated using the points from the previous simulation and a Lorentzian function fitted to it. 77
- Figure 6.1 Schematic showing the optical setup we used in the implementation of our optical tweezer. 78
- Figure 6.2 Alignment procedure used in our implementation: (a) Coarse alignment of the beam and the objective's longitudinal axis; (b) Positioning of the camera and fine alignment of the beam; (c) Positioning of the PS detector; (d) Positioning of the second objective lens. The solid red arrows represent the trapping laser beam, while the dashed red arrows represent the back reflection. 82
- Figure 6.3 Back reflection pattern observed in the camera when: (a) the beam is not properly aligned; (b) the beam is properly aligned. 83
- Figure 6.4 Final configuration of the optical setup with a sample in place: (a) sample containing spheres immersed in water; (b) complete optical tweezer setup. The red arrows represent the trapping laser beam, while the yellow ones represent the light emitted by the LED. 83
- Figure 6.5 Trapped $2.47 \mu\text{m}$ Silica sphere. The time interval between frames is $1/15$ seconds and the sample is moving upwards. The red circle highlights the trapped particle, while the yellow circles highlight particles that are not trapped. 84

Figure 6.6	Micro-spheres of different diameters and materials in our optical trap. Polystyrene spheres: (a) $0.505\ \mu\text{m}$ at the first stable position; (b) $0.505\ \mu\text{m}$ at the second stable position; (c) $0.746\ \mu\text{m}$; (d) $1.925\ \mu\text{m}$; (e) $3.00\ \mu\text{m}$; (f) $4.52\ \mu\text{m}$. Silica spheres: (g) $1.15\ \mu\text{m}$; (h) $2.47\ \mu\text{m}$.	85
Figure 6.7	Attempt of trapping a $0.99\ \mu\text{m}$ Polystyrene sphere. The time interval between frames is $1/15$ seconds and the red circle indicates the particle's position.	86
Figure 6.8	Power spectral density of the position of the trapped particle in one direction for four different micro-spheres: (a) $1.15\ \mu\text{m}$ Silica sphere; (b) $1.925\ \mu\text{m}$ Polystyrene sphere; (c) $2.47\ \mu\text{m}$ Silica sphere; (d) $3.00\ \mu\text{m}$ Polystyrene sphere.	87
Figure 6.9	Characteristic frequency (κ/γ) as a function of the laser power for: (a) $1.15\ \mu\text{m}$ Silica and (c) $2.47\ \mu\text{m}$ Silica spheres; and mean squared displacement for: (b) $1.15\ \mu\text{m}$ and (d) $2.47\ \mu\text{m}$ Silica spheres.	89
Figure 7.1	Simplified setup for implementing a Pound-Drever-Hall stabilization scheme.	91
Figure 7.2	Reduced cost optical tweezer implementation: (a) $2.47\ \mu\text{m}$ Silica sphere trapped by an aspheric lens; (b) alternative setup for measuring a trapped particle's position.	93
Figure 7.3	Intensity pattern resulting from the interference between a Gaussian beam and a $l = 0, p = 1$ Laguerre-Gauss beam having a phase difference of π .	94
Figure 7.4	Intensity pattern resulting from the interference between a Gaussian beam and a $l = 0, p = 1$ Laguerre-Gauss beam having a phase difference of π .	95
Figure 7.5	Spheres inside our chamber and their trajectories, traced out by a software. Image courtesy of Igor Brandão.	96
Figure 7.6	Schematic of a setup in which the cavity's optical field, the membrane's motion and the sphere's motion are coupled.	97

List of tables

Table 3.1	Ratio between mode power and total power for different Hermite-Gauss modes and different angles between the beam's axis and the cavity's axis.	43
Table 6.1	Results obtained in the PSD analyses for four different spheres.	88
Table 6.2	Results obtained in the ACF analyses for two different spheres.	89

1 Introduction

The nature of light has been a question of major importance in the history of science [1]. Today, we know among other things that light carries momentum and that it can interfere.

Momentum transfer due to interaction with light is taking place all around us and at every moment, but it is just too small to be noticed in every-day life. Although some experiments have been able to demonstrate the force caused by momentum transfer between light and macroscopic objects in the beginning of the last century [2, 3], it wasn't until the 60's, when Maiman invented the laser [4], that the possibility of routinely observing this force, called radiation pressure, became a reality [5–7].

Lasers emit a large amount of photons of the same energy and momentum concentrated in a small region. This “coherent nature” of laser light can be used - as first demonstrated by Ashkin in 1970 - to accelerate and trap micron-sized particles [8]. In 1986, influenced by Steven Chu, who was also working in the Bell Laboratories and was trying to trap atoms, Ashkin built a setup capable of trapping dielectric particles using a single tightly focused laser beam [9]. Since both atoms and sub-micron sized dielectric particles can be treated as electric dipoles, this apparatus, which today is known as an optical tweezer, served as a *proof of principle* demonstration to what Chu was trying to accomplish.

An optical tweezer consists of a tightly focused laser beam that, due to the momentum transfer between the photons from the laser and the particle, pushes the particle towards the laser's focal region. Under the right circumstances, this focal point is a stable equilibrium position of the particle, enabling the manipulation of particles with sizes ranging from dozens of nanometers [10, 11] all the way to dozens of micrometers [12].

Another important feature of light is interference. This is the fundamental property behind a class of devices called optical resonators [13]. In these devices, the optical field can be amplified due to interference when the light's frequency matches the resonator frequency.

One possible realization of such device is the Fabry-Pérot cavity, which will be greatly exploited in this work: two mirrors are placed parallel to each other and a laser beam is directed to one of them [14]. The light that enters

this cavity will be reflected multiple times by the mirrors and, if it has the right frequency, constructive interference will take place building up the optical field inside the cavity [15, 16].

Radiation pressure and interference form, together, the basis of optomechanics, a branch of physics that studies systems in which light is coupled to mechanical motion [17]. In such systems, light exerts force upon a mechanical oscillator, which in turn can affect light resonance inside an optical resonator [18].

Together, cavities and tweezers span a wide range of possibilities in terms of optomechanics experiments [19, 20]. These include applications on quantum communication networks, quantum information and metrology protocols, as well as fundamental science [21–26]. One future aim of our laboratory is the execution of an experiment that unifies both tools in a highly sensitive force and displacement sensor aimed at fundamental physics tests.

A conceptual schematic of this sensor is shown in Figure 1.1: a dielectric sphere is trapped by an optical tweezer and placed close to a thin membrane, which is coupled to the resonant optical field present inside the cavity. If a force between the two objects arises, the membrane is deformed, affecting the cavity's resonance [27]. This could be useful in the search for new fundamental Yukawa-type forces of nature which would manifest at and below scales of a micrometer [28–30].

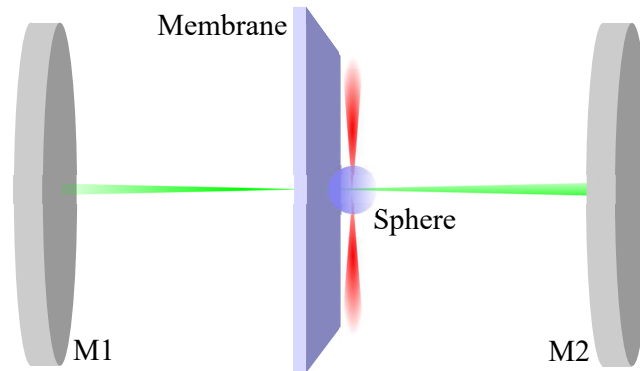


Figure 1.1: Conceptual schematics of our proposed optomechanical force sensor.

Implementing this fundamental physics experiment is a challenging task. We have therefore broken it down into two parts: the first one is to build an optical tweezer capable of trapping micro-spheres in vacuum; the second one is to build a *membrane-in-the-middle* optomechanical resonator. This work is dedicated to the very first steps towards these tasks and their full integration.

We have built an optical tweezer capable of trapping micro-spheres in water, as means to better comprehend this optical tool before moving on

to trapping spheres in vacuum. On the resonator side, we have built and studied Fabry-Pérot cavities formed by spherical mirrors, as it should be for a *membrane in the middle* configuration [27], and also cavities formed by a plane mirror and a spherical mirror, since this will be useful if we decide, in the future, to work with cavities having one moveable mirror [31].

In order to understand optical cavities and optical tweezers, it is important to understand the behaviour of the coherent radiation emitted by lasers. Therefore, we start, in Chapter 2, by demonstrating how the electromagnetic theory gives rise to Gaussian beams, Hermite-Gauss beams and Laguerre-Gauss beams. We also present a method for calculating how these beams propagate and interact with optical elements in the laboratory.

Once that is done, we have the tools to derive the basic theory regarding optical cavities, which is done in Chapter 3. Important cavity parameters are introduced and mathematically related to the optical properties of the cavity's mirrors. Then, we discuss what the cavity's parameter should be in order to be compatible with the used laser beam or conversely, what the beam's parameters should be in order to be compatible with a given cavity. This results in mathematical expressions that can be used to design a cavity setup.

This expressions are then used to implement our optical cavities, which are detailed on Chapter 4. As we've said previously, we implement both a cavity formed by a plane and a spherical mirror and a cavity formed by two spherical mirrors. We also implement the latter in the confocal configuration, in order to demonstrate the mode degeneracy inside the cavity. This concludes our work with optical cavities, and allows us to start the study of optical tweezers.

Just like we did for optical cavities, we start the study of optical tweezers with a theoretical chapter, which is Chapter 5. First, the three regimes in which optical trapping can take place are presented: the geometrical optics regime, which provides a simple picture of the interaction between a laser beam and a relatively large dielectric sphere, the dipole regime, which approximates a small particle to an electric dipole, resulting in explicit mathematical formulas relating all the tweezer's relevant quantities, and the Mie regime, which treats optical trapping in terms of the full electromagnetic theory. After that, the motion of trapped particles is discussed, and important measurable quantities regarding it are presented.

Once again following the approach used for optical cavities, we dedicate Chapter 6 to present the experimental implementation of an optical tweezer. In order to test the functionality of our apparatus, tweezer is used to trap spheres of different materials and different sizes. Once the optical tweezer passes this initial test, we study the brownian motion of particles confined by harmonic

potential by trapping spheres and measuring the autocorrelation function and the power spectral density of their movement. This allows us to calibrate our optical tweezer, making possible for it to be used in real force measurement experiments.

Finally, on chapter 7, we briefly review the experimental achievements resulting from the implementations presented in the previous chapters. Special attention is devoted, to present our perspectives regarding the force sensor already described and other branches which we would like to explore, such as optical tweezers in liquids, statistical mechanics with micro-spheres and cavity optomechanics.

2

Gaussian beams and their propagation

The fundamental concept underlying both optical cavities and optical tweezers is that of a Gaussian beam, which regards the specific intensity and phase structure that light assumes in most optics experiments. In this chapter, we are going to see how the laws of electromagnetism give rise to Gaussian beams, as well to Hermite-Gauss and Laguerre-Gauss beams, under certain assumptions. Since the existence of Gaussian beams relies on the wave nature of light, geometric optics is insufficient to calculate their propagation and, therefore, we will also present a method for performing such calculations. In the end of the chapter, we'll use the developed concepts and methods to discuss the real nature of collimated beams in a laboratory.

2.1

The paraxial approximation

2.1.1

Gaussian Beams

In the absence of charges and currents - which is the case of the experiments detailed in this work - the electromagnetic field dynamics can be described by Maxwell's equations, a set of four differential equations in which the electric field $\vec{\mathcal{E}}$ and the magnetic field $\vec{\mathcal{B}}$ are coupled [32]:

$$\nabla \cdot \vec{\mathcal{E}} = 0; \quad (2-1a)$$

$$\nabla \times \vec{\mathcal{E}} = - \frac{\partial \vec{\mathcal{B}}}{\partial t}; \quad (2-1b)$$

$$\nabla \cdot \vec{\mathcal{B}} = 0; \quad (2-1c)$$

$$\nabla \times \vec{\mathcal{B}} = \mu\epsilon \frac{\partial \vec{\mathcal{E}}}{\partial t}. \quad (2-1d)$$

where μ and ϵ are, respectively, the magnetic permeability and the electric permittivity of the medium.

In order to uncouple those equations and have better insight in how they dictate the electromagnetic field behaviour, the curl operator can be applied to equation 2-1b, yielding, after using the vector identity $\nabla(\nabla \cdot \vec{A}) =$

$\nabla(\nabla \cdot \vec{A}) - \nabla^2 \vec{A}$ together with equation 2-1d:

$$\nabla^2 \vec{\mathcal{E}} = \mu\epsilon \frac{\partial^2 \vec{\mathcal{E}}}{\partial t^2} \quad (2-2)$$

This has the form of the well-known wave equation. The most commonly used basis for the solutions of this equation is the set of plane wave solutions given by:

$$\vec{\mathcal{E}} = \vec{\mathcal{E}}_0 \sin(\vec{k}_m \cdot \vec{r} - \omega t) \quad (2-3)$$

Equation 2-3 describes a plane wave that propagates in the \hat{k}_m direction with frequency ω , wavelength $\lambda_m = 2\pi/k_m$ and velocity $c_m = 1/\sqrt{\mu\epsilon}$. As a matter of fact, any solution can be decomposed onto the plane wave basis set by taking the inverse Fourier transform of the electric field:

$$\vec{\mathcal{E}}(\vec{r}, t) = \int \vec{\mathcal{E}}(\vec{k}_m, \omega) e^{i\vec{k}_m \cdot \vec{r}} e^{i\omega t} d^3 \vec{k}_m d\omega \quad (2-4)$$

where ω and $|\vec{k}_m|$ are related by the dispersion relation:

$$(k_m^2 - \omega^2 \mu\epsilon) = 0, \quad (2-5)$$

In most applications we are concerned with monochromatic light, implying a constant ω (and, due the dispersion relation, a constant $|\vec{k}_m|$). Therefore, we can rewrite the electric field as $\vec{\mathcal{E}}(\vec{r}, t) = \Re(\vec{E}(\vec{r})e^{i\omega t})$, solve our problems considering only $\vec{E}(\vec{r})$ and then go back to $\vec{\mathcal{E}}(\vec{r}, t)$.

Of special interest in laser physics are the paraxial solutions for the electric field [33]. These are solutions that describe beams that propagate in a given direction and have a transverse profile that varies slowly in the longitudinal direction. Mathematically, if we consider a beam propagating along the z axis, this is equivalent to say that:

$$\left| \frac{\partial^2 |\vec{\mathcal{E}}|}{\partial z^2} \right| \ll \left| \frac{\partial^2 |\vec{\mathcal{E}}|}{\partial x^2} \right|, \left| \frac{\partial^2 |\vec{\mathcal{E}}|}{\partial y^2} \right|, k \left| \frac{\partial |\vec{\mathcal{E}}|}{\partial z} \right| \quad (2-6)$$

allowing for certain approximations to take place in Equation 2-2. Instead of carrying out these approximations, we shall focus on the Fourier decomposition of a paraxial beam.

In this decomposition, the longitudinal component of wave vector will be much larger than the transverse components of the wave vector. This allows for the approximation [34]:

$$k_{m,z} = \sqrt{k_m^2 - k_{m,x}^2 - k_{m,y}^2} \approx k_m - \frac{k_{m,x}^2 + k_{m,y}^2}{2k_m} \quad (2-7)$$

This paraxial approximation can be used to calculate the electric field in all points of space provided that the field distribution at a given transverse plane is known. If the electric field at the plane $z = 0$ is given by:

$$\vec{E}(x, y, 0) = \sqrt{\frac{2}{\pi}} \frac{\vec{E}_0}{\omega_0} e^{-\rho^2/\omega_0^2} \quad (2-8)$$

then its Fourier transform in the xy plane reads:

$$\vec{E}(k_{m,x}, k_{m,y}, 0) = \frac{\vec{E}_0 \omega_0}{(2\pi)^{3/2}} \exp \left[-\frac{\omega_0^2}{4} (k_{m,x}^2 + k_{m,y}^2) \right] \quad (2-9)$$

Now each of these components must be propagated through space, which is done by multiplying 2-9 by an exponential factor $e^{i\vec{k}_m \cdot \vec{r}}$. The resultant electric field will then be given by:

$$\vec{E}(x, y, z) = \int \vec{E}(k_{m,x}, k_{m,y}, 0) e^{i\vec{k}_m \cdot \vec{r}} d\vec{k}_m \quad (2-10)$$

Plugging equation 2-9 into 2-10 and using 2-7 to substitute $k_{m,z}$ gives the electric field of a Gaussian beam:

$$\vec{E}^G(x, y, z) = \vec{E}_0 e^{ik_m z} u_{00}(x, y, z) \quad (2-11)$$

where $u_{00}(x, y, z)$ is the fundamental Gaussian mode, given by:

$$u_{00}(\rho, z) = \sqrt{\frac{2}{\pi}} \frac{1}{\omega(z)} \exp \left(-\frac{\rho^2}{\omega(z)^2} - i\zeta(z) + ik_m \frac{\rho^2}{2R(z)} \right) \quad (2-12)$$

where $\omega(z)$, $R(z)$, $\zeta(z)$ and z_R are called beam width, wavefront radius, Gouy phase shift and Rayleigh range, respectively, and are given by:

$$\omega(z) = \omega_0 \sqrt{1 + \frac{z^2}{z_R^2}} \quad (2-13a)$$

$$R(z) = z \left(1 + \frac{z_R^2}{z^2} \right) \quad (2-13b)$$

$$\zeta(z) = \arctan \frac{z}{z_R} \quad (2-13c)$$

$$z_R = \frac{\pi \omega_0^2}{\lambda_m} \quad (2-13d)$$

The electric field expression shown in equation 2-11 reveals some important beam parameters. The first of them is the beam width $\omega(z)$. To see why this parameter is a measure of the width of the beam, it is useful to calculate the intensity of the electromagnetic field :

$$I(x, y, z) = \frac{c\epsilon}{2} |\vec{E}^G|^2 = I_0 \frac{\omega_0^2}{\omega(z)^2} \exp \left(-\frac{2\rho^2}{\omega(z)^2} \right) \quad (2-14)$$

As it can be seen, the beam width $\omega(z)$ gives the distance from the z axis at which the intensity is reduced to $1/e^2$ of the intensity at the center of the beam. Figure 2.1 shows the intensity distribution at the plane $z = 0$. This figure and all other simulations and theoretical plots presented in this work were made using the software Mathematica.

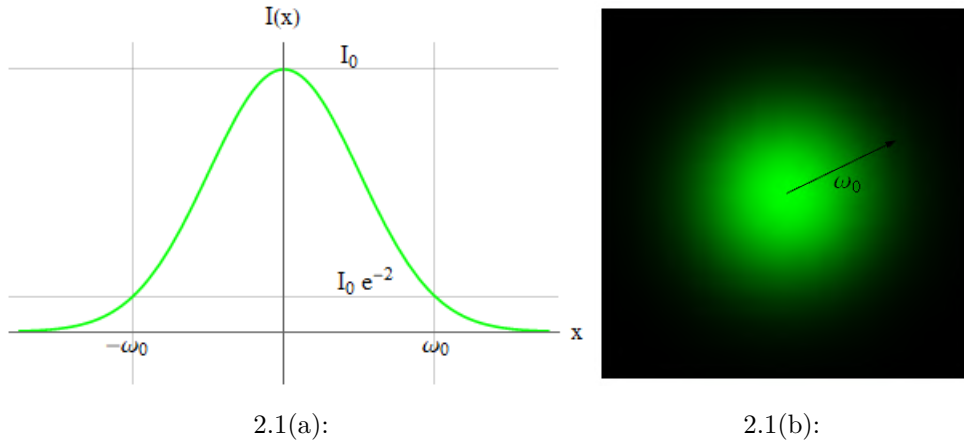


Figure 2.1: Transverse intensity profile for the Gaussian mode at $z = 0$.

From equation 2-13a, we can see that the beam width has a minimum ω_0 at $z = 0$. This is called the beam waist. Also, it can be seen that for $z \gg z_R$, the dependence of the beam width with z becomes linear:

$$\omega(z) \approx \frac{\lambda_m}{\pi\omega_0} z \quad (2-15)$$

Therefore, the parameter z_R gives the range of non-linear behavior of the beam longitudinal profile.

The linear coefficient of equation 2-15 is called the Numerical Aperture (NA), and it gives a measure of how divergent a beam is:

$$NA = \frac{\lambda_m}{\pi\omega_0} \quad (2-16)$$

Finally, $R(z)$ gives the radius of curvature of the wave front, which is nearly spherical close to the beam axis [34]. Figure 2.2 shows a Gaussian beam longitudinal profile, highlighting the parameters presented above.

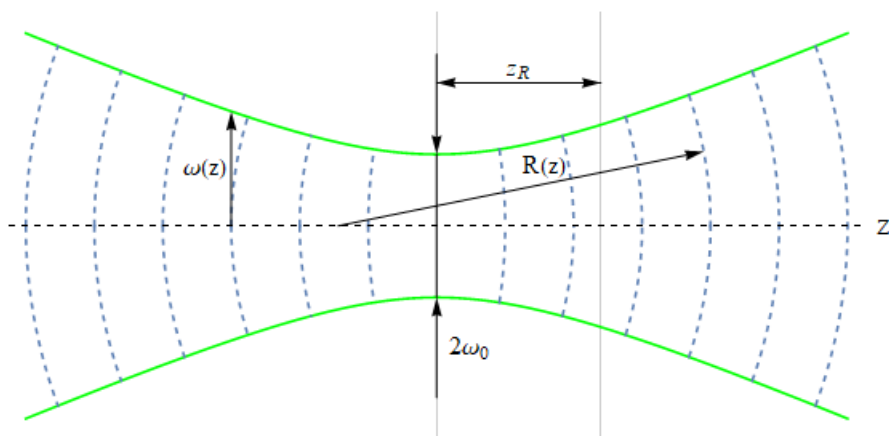


Figure 2.2: Longitudinal profile of a Gaussian beam, defined as the beam width outline.

2.1.2

Higher order transverse modes

The Gaussian solution to the paraxial equation is one of many possible solutions. More general solutions are the Hermite-Gauss solutions and the Laguerre-Gauss solutions, which have a electric field distribution given, respectively, by [34]:

$$\vec{E}_{m,n}^{HG}(x, y, z) = \vec{E}_0 e^{ik_m z} u_{m,n}^{HG}(x, y, z) \quad (2-17a)$$

$$\vec{E}_{l,p}^{LG}(x, y, z) = \vec{E}_0 e^{ik_m z} u_{l,p}^{LG}(x, y, z) \quad (2-17b)$$

where $u_{m,n}^{HG}$ and $u_{l,p}^{LG}$ are the Hermite-Gauss and the Laguerre-Gauss modes, respectively, which are given by:

$$u_{m,n}^{HG}(x, y, z) = c_{m,n}^{HG} H_m \left(\frac{\sqrt{2}x}{\omega(z)} \right) H_n \left(\frac{\sqrt{2}y}{\omega(z)} \right) e^{-i(m+n)\zeta(z)} u_{00}(x, y, z) \quad (2-18a)$$

$$u_{l,p}^{LG}(x, y, z) = c_{l,p}^{LG} \left(\frac{\sqrt{2}\rho}{\omega(z)} \right)^{|l|} L_p^l \left(\frac{2\rho^2}{\omega(z)^2} \right) e^{-i(2p+l)\zeta(z)} e^{il\phi} u_{00}(x, y, z) \quad (2-18b)$$

where $c_{m,n}^{HG}$ and $c_{l,p}^{LG}$ are normalization constants.

In equation 2-18a, H_m and H_n are the Hermite polynomials of order m and n , respectively, with $m, n \in \mathbb{N}$. In equation 2-18b, L_l^p is the generalized Laguerre polynomial with $l \in \mathbb{Z}$ and $p \in \mathbb{N}$ [35]. The values of m, n or l, p determine the order of the mode. For a Hermite-Gauss mode, the order is given by $N = m + n$, while for a Laguerre-Gauss mode the order is given by $N = 2p + |l|$. The transverse intensity profile for $m, n, l, p \in 0, 1, 2$ are shown in Figure 2.3.

As it can be seen, m and n determine how many dark voids will appear in the horizontal and in the vertical direction, respectively. For the Laguerre-Gauss modes, p determines the number of dark rings in the profile, while $l \neq 0$ determines the presence of a dark singularity at the center of the beam.

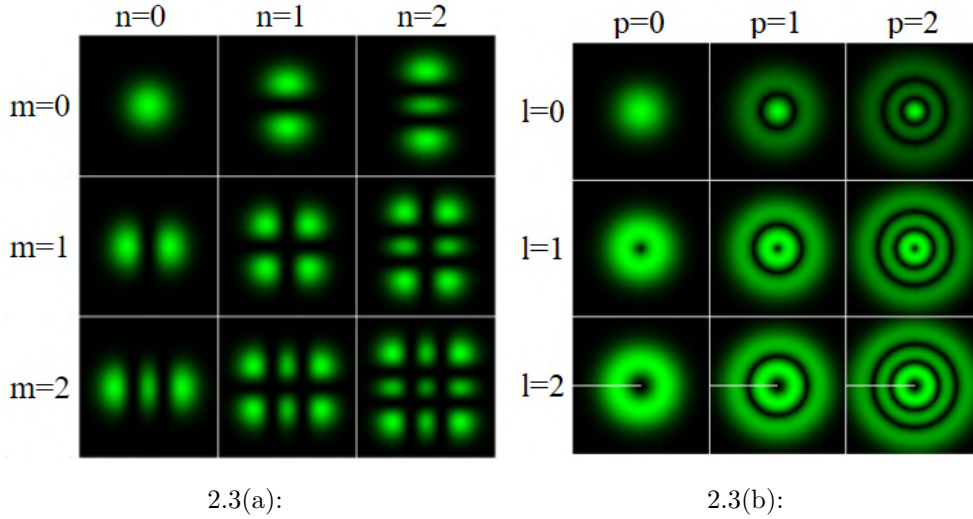


Figure 2.3: Transverse intensity profile for higher-order beams: (a) Hermite-Gauss beams; (b) Laguerre-Gauss beams.

The set of all Hermite-Gauss modes - as well as the set of all Laguerre-Gauss modes - is a complete orthonormal basis for the paraxial solutions of the electric field wave equation 2-2. That means that any paraxial solution can be decomposed as a superposition of Hermite-Gauss modes - or Laguerre-Gauss - modes [34].

As an example, let $\vec{F}(\vec{r}) = F(\vec{r})e^{ik_m z}\hat{e}$ be a generic electric field in the paraxial approximation. We can write $F(\vec{r})$ as a superposition of Hermite-Gauss modes:

$$F(x, y, z) = \sum_{m,n=0}^{\infty} C_{m,n}^F u_{m,n}^{HG}(x, y, z) \quad (2-19)$$

Equation 2-19 must hold for all values of z . Taking $z = 0$, multiplying both sides by $[u_{m',n'}^{HG}(x, y, 0)]^*$ and integrating over all x and y , we find:

$$C_{m,n}^F = \int_{-\infty}^{\infty} \int_{-\infty}^{\infty} F(x, y, 0) [u_{m',n'}^{HG}(x, y, 0)]^* dx dy \quad (2-20)$$

In order to calculate the coefficients $C_{m,n}^F$ we need to know the normalization constants $c_{m,n}^{HG}$. These values can be calculated by integrating $|u_{m,n}^{HG}(x, y, z)|^2$ over x and y and imposing that the result is equal to 1. This yields:

$$c_{m,n}^{HG} = (2^{m+n} m! n!)^{-1/2} \quad (2-21)$$

By taking the squared absolute value of both sides of 2-19 and integrating over all x and y we find, after using the orthonormality of the Hermite-Gauss modes, that the total power at any given z plane will be given by the sum of the powers of each mode, which in turn is given by:

$$P_{mn} = \frac{c\epsilon}{2} |C_{m,n}^F|^2 \quad (2-22)$$

Similar calculations can be carried out in order to decompose a generic paraxial solution onto the Laguerre-Gauss basis and to calculate the power of each component [36].

2.2

Beam propagation through optical elements

2.2.1

ABCD matrix and the q parameter

Although equation 2-11 gives the electric field of a Gaussian beam in its full form, there is a better formalism to be used in order to calculate how a beam propagates through a series of optical elements. By the definitions of the beam width and the wave front radius, given by equations 2-13a and 2-13b respectively, we can see that, for a beam having a waist at z_0 :

$$\left(\frac{1}{R(z - z_0)} - i \frac{\lambda}{\pi\omega(z - z_0)^2} \right)^{-1} = z - z_0 + iz_R \quad (2-23)$$

That means that the quantity in the left side of 2-23 evolves linearly with z . Moreover, its real part is null at the waist of the beam and the imaginary part contains the information, according to the definition in equation 2-13d, about the beam waist size itself. This is very useful, because looking at equation 2-11 we can see that the electric field is completely defined by the wavelength, the beam waist and the beam waist position. Therefore, it is convenient to define the left side of equation 2-23 as a quantity $q(z)$ that evolves linearly with z and use this quantity when propagating a Gaussian beam through space:

$$\begin{cases} q(z) = q_0 + z - z_0 \\ \text{Re}[q(z')] = 0 \longleftrightarrow z = z_0 \\ \text{Im}[q(z)] = \frac{\pi\omega_0^2}{\lambda} \end{cases} \quad (2-24)$$

Equation 2-24 also holds for Hermite-Gauss and Laguerre-Gauss beams, since the definition of beam width and wave front radius for those beams is the same as those for a Gaussian beam.

It is necessary to calculate how $q(z)$ transforms when the beam goes through optical elements, like lenses and mirrors. To do so, it is useful to make a small digression and study how light rays propagate through these elements in the geometrical optics theory.

In geometrical optics, a ray propagating in a plane free of optical elements is completely defined by the distance from the ray to a given axis at a given

point and the angle the ray makes with that axis. That is, if we specify the quantities h and θ at the point P for the ray in Figure 2.4(a) we can reconstruct its path in the entire plane [37].

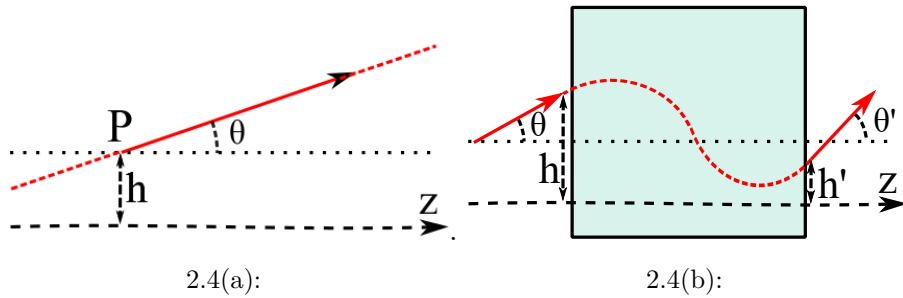


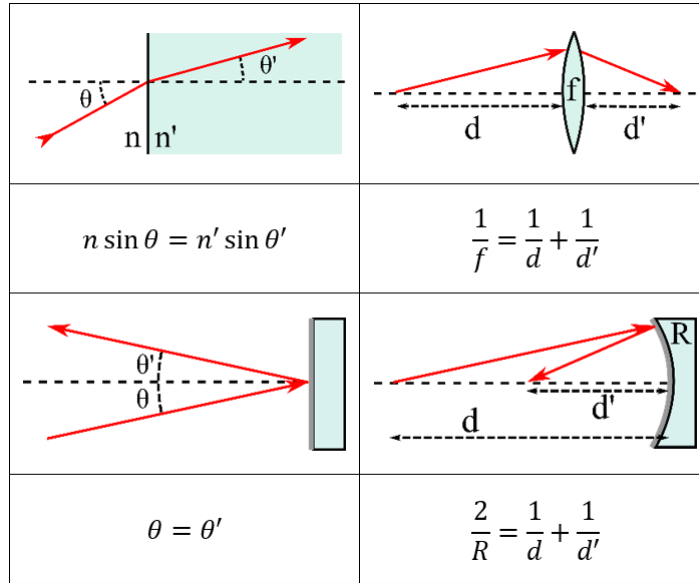
Figure 2.4: Parameters h and θ for light rays in geometric optics: (a) definition of the parameters; (b) change in the parameters when the ray passes through a generic optical element.

If an optical element is introduced, the ray's path will be altered, and it will have, generally, different h and θ before the element and after the element, as shown in Figure 2.4(b). The values of these quantities at the output depend on the element properties and on the values of these quantities at the input. If θ is small - that is, if the ray is a paraxial ray - this dependence will be linear, and can be written in the form [38]:

$$\begin{bmatrix} h' \\ \theta' \end{bmatrix} = \begin{bmatrix} A & B \\ C & D \end{bmatrix} \begin{bmatrix} h \\ \theta \end{bmatrix} \quad (2-25)$$

The specific values of A, B, C, D for different elements can be calculated, in general, using simple geometrical optics laws, which are presented in Figure 2.5.

It is worth noticing that the law for lenses and spherical mirrors are very similar. In fact, it is often useful to treat a reflection by a spherical mirror as a transmission through a lens with focal distance equal to half the radius of curvature of the mirror. This equivalence also holds for the plane mirror, and will be explored in more detail when optical cavities are introduced.

Figure 2.5: Geometric laws used to derive the $ABCD$ matrices.

By making use of the relations presented in Figure 2.5, it is possible to calculate the matrices for a variety of optical elements. For the purposes of this work, there are three matrices in which we are interested: the matrix for a thin lens, the matrix for a plane mirror, the matrix for a spherical mirror and the matrix for a homogeneous medium with refractive index n . Each of those elements are shown in Figure 2.6. The equivalence mentioned in the previous paragraph between lenses is applied to the mirrors matrices.

Now that the $ABCD$ matrices have been introduced, we can go back to discussing the propagation of Gaussian beams. It can be proven that when a beam passes through the optical elements we are interested in, its parameter q transforms according to [37]:

$$q' = \frac{Aq + b}{Cq + D} \quad (2-26)$$

where the values of A , B , C and D are the same as the values of A , B , C and D of the matrix that represents the optical element in geometrical optics. Therefore, one can calculate how a Gaussian beam will propagate through a series of optical elements only by using the matrices derived from geometrical optics and the relations shown in 2-24.

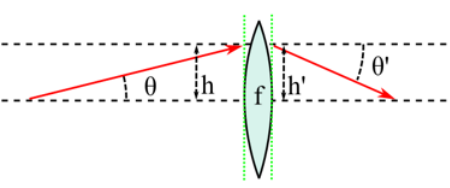
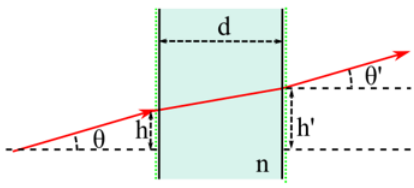
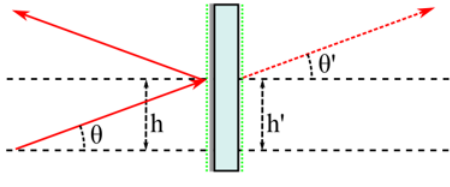
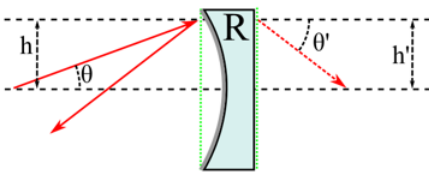
	
$\begin{bmatrix} A & B \\ C & D \end{bmatrix} = \begin{bmatrix} 1 & 0 \\ -1/f & 1 \end{bmatrix}$	$\begin{bmatrix} A & B \\ C & D \end{bmatrix} = \begin{bmatrix} 1 & d/n \\ 0 & 1 \end{bmatrix}$
	
$\begin{bmatrix} A & B \\ C & D \end{bmatrix} = \begin{bmatrix} 1 & 0 \\ 0 & 1 \end{bmatrix}$	$\begin{bmatrix} A & B \\ C & D \end{bmatrix} = \begin{bmatrix} 1 & 0 \\ -2/R & 1 \end{bmatrix}$

Figure 2.6: $ABCD$ matrices for four different optical elements.

2.2.2 ABCD calculation example

To exemplify the $ABCD$ method, consider a beam that has a waist ω_0 at z_0 , as shown in Figure 2.7. The parameter q at z_0 is, according to equation 2-24, $q_0 = i\pi\omega_0^2/\lambda$. If a lens is positioned at z_L , the beam will have a new waist at a new position after going through the lens. In order to calculate the parameter q at a point $z > z_L$, the propagation can be divided in three parts:

1. A propagation over a distance $z_L - z_0$ through a medium with $n = 1$;
2. A passing through the lens;
3. A propagation over a distance $z - z_L$ through a medium with $n = 1$.

The total $ABCD$ matrix will be the product $M_3M_2M_1$ of the $ABCD$ matrices of each part. Therefore:

$$\begin{aligned}
 M &= \begin{bmatrix} 1 & z - z_L \\ 0 & 1 \end{bmatrix} \begin{bmatrix} 1 & 0 \\ -1/f & 1 \end{bmatrix} \begin{bmatrix} 1 & z_L - z_0 \\ 0 & 1 \end{bmatrix} = \\
 &= \frac{1}{f} \begin{bmatrix} f - z + z_L & f(z - z_0) + (z - z_L)(z_0 - z_L) \\ -1 & f + z_0 - z_L \end{bmatrix} \quad (2-27)
 \end{aligned}$$

Since the parameter q_0 at z_0 is known, Equation 2-26 can be used, together with the values provided by the matrix M from equation 2-27 to calculate the parameter $q(z)$ for any $z > z_L$. By making use of the relations

presented in 2-24 involving the real and imaginary parts of q , we can calculate the waist and the waist location after the lens.

Similar calculations hold for more complex situations where more optical elements are present. Each optical element can be represented by a matrix and the q parameter can be calculated as described above. This method will be specially useful when calculations regarding optical cavities are performed in Chapter 3.

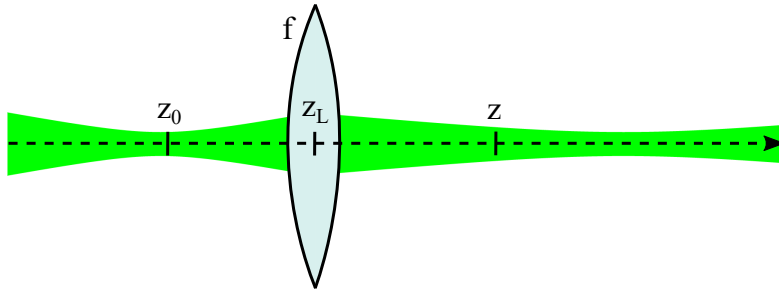


Figure 2.7: Transformation of a beam by a thin lens of focal distance f positioned at z_L . The beam location is z_0 before the lens and z after the lens.

2.2.3 Beam collimation theory

In geometric optics, a collimated beam is a beam consisting of parallel light rays. Since the rays are parallel, the beam doesn't diverge, and the beam is often said to be "focused to infinity". When working with Gaussian beams, a perfectly collimated beam cannot exist, since it is not a solution to the paraxial equation. In order to understand what we mean, in this work, by a collimated Gaussian beam, it is useful to consider the collimation of a beam at the output of an optical fiber.

Let us consider that a fiber output is positioned at $z = 0$, and a lens with focal distance 15.36 mm is positioned at $z = z_L$. If the fiber's output numerical aperture is 0.12 and the beam's wavelength is 532 nm, then the beam's waist is $1.41 \mu\text{m}$, and the q parameter at $z = 0$, which is the beam's waist location, is $q_0 = 1.18 \times 10^{-5}$. Using Equation 2-27 we can find the parameter q at any coordinate $z > z_L$. Equating the real part of this parameter to 0 and solving for z , we find the waist's location as a function of z_L , and equating the imaginary part to $\pi\omega^2/\lambda$ we can find the new beam's waist.

Figure 2.8(a) shows the waist's location z as a function of the lens position z_L . Although z diverges when z_L approaches infinity, this is an unrealistic situation, since an infinite distance between the fiber's output and the lens

would require the lens to have an infinite radius in order to collect all the light exiting the fiber. Therefore, we focus on $z_L \approx 15.36$ mm, which is the lens position necessary for collimation according to geometrical optics. In the interval shown, z has a maximum of 10.06 m for $z_L = 15.372$ mm. That means that this should be the lens position if we want to focus the beam as far as possible. For this value of z_L , the beam's waist is 1.303 mm.

Figure 2.8(b) shows the size of the beam's waist as a function of z_L . The waist has a maximum value of 1.843 mm for $z_L = 15.36$ mm. Since a larger waist implies smaller numerical aperture, this should be the lens position if we want the smallest beam divergence. For this value of z_L , we have $z = 3.07$ cm.

In our laboratory, collimation is performed by focusing the beam in a screen placed as far from the lens as possible, and then tilting the lens in the direction that would make the beam focus even further. Therefore, we work with the Gaussian beam analogue of "focusing to infinity".

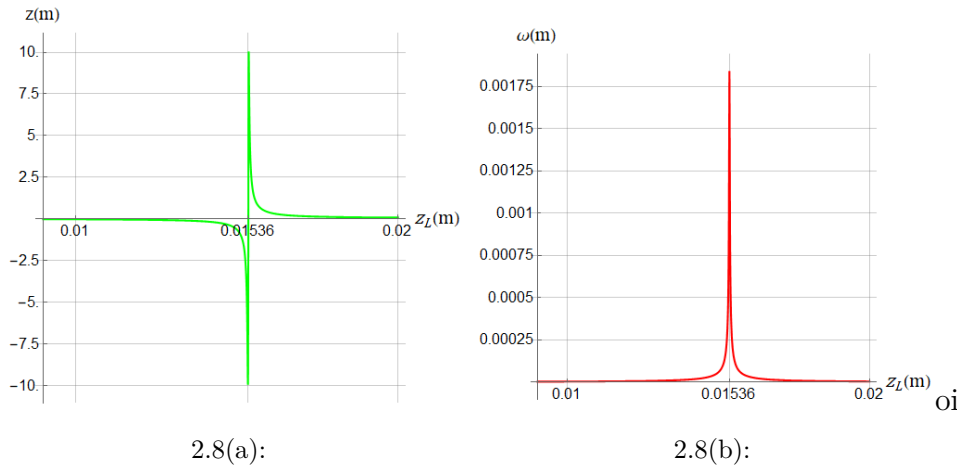


Figure 2.8: Theoretical collimation of a beam: (a) waist location as a function of the position of the lens; (b) waist size as a function of the position of the lens.

2.2.4 Collimated beams in the laboratory

A more practical calculation method arises from the asymptotic behavior of the Gaussian beam for $z > z_R$. As we have seen, far from the focus the beam width evolves linearly with z . The angle of expansion of the beam can be calculated from the numerical aperture definition given by equation 2-16. If we know the beam width at the output (input) of a lens and the output (input) beam waist location, we can calculate the output (input) beam waist.

This is of particular interest in situations where the output (input) of a lens is collimated, in the previously discussed sense. In this case, the distance from the lens to the input (output) waist location is approximately equal to the lens focal distance.

There are two recurrent situations when dealing with laser beams. In the first of them, a beam having waist ω_0 passes through a lens with focal length f_1 , becomes collimated and is then focused by a second lens with focal length f_2 , as shown in Figure 2.9(a). The collimated beam width ω_c will be given by the width of the beam right before the first lens. This can be calculated from the first triangle in Figure 2.9(a), where the angle θ is given by equation 2-16:

$$\omega_c = f_1 \tan \theta = \frac{f_1 \lambda}{\pi \omega_0} \quad (2-28)$$

After the second lens, the beam is focused again, this time with a beam waist ω'_0 . This can be calculated from the second triangle together with the numerical aperture definition once more:

$$\omega'_0 = \frac{\lambda}{\pi NA} = \frac{\lambda f_2}{\pi \omega_c} = \frac{f_2}{f_1} \omega_0 \quad (2-29)$$

The second commonly encountered situation is shown in Figure 2.9(b). A beam initially collimated is brought to a focus by a lens with focal length f_1 and is then collimated again by a lens with focal length f_2 . The quantities of interest are, usually, the collimated beam width ω_c before the lens and the collimated beam width ω'_c after the lens. A simple triangle similarity is enough to calculate one of those quantities provided that the other is known:

$$\frac{\omega_c}{f_1} = \frac{\omega'_c}{f_2} \quad (2-30)$$

If the beam's waist between the lenses is of interest, its calculation can be easily performed by using the numerical aperture definition as discussed in the first situation.

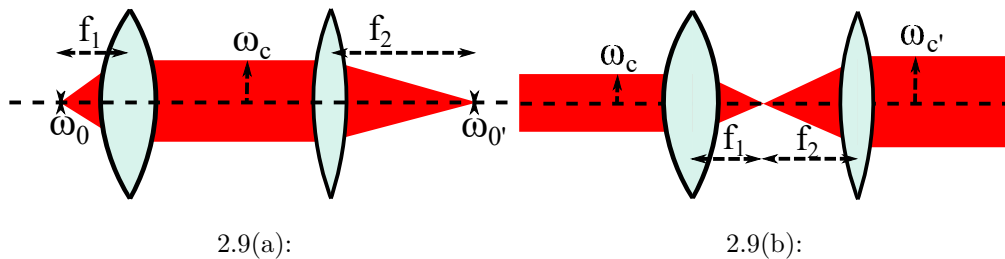


Figure 2.9: Approximations involving collimated beams: (a) transformation of a beam's waist; (b) transformation of collimated waist (telescope configuration).

The concepts and methods introduced in this chapter will be used

throughout this entire work. In the next chapter, they will be used to study optical cavities and to calculate relevant quantities regarding them.

3 Optical cavities

An optical cavity is a structure that allows light to resonate under the right circumstances. One of the simplest realization of such a structure are two mirrors placed parallel to each other [16]. If light is directed towards this structure, it has a probability of entering it, and, once inside it, it will be reflected multiple times, having a certain probability of leaving the cavity at each reflection. Due to the wave nature of light, this process will cause light to interfere inside the cavity, and if it has the appropriate wavelength, constructive interference will take place, giving rise to resonance.

This chapter is dedicated to the study of this kind of optical cavity, to calculate how the various parameters present in it affect light resonance and to discuss what these parameters should be in order for the cavity to have certain desired characteristics

3.1 The plane mirror optical cavity

To understand how an optical cavity works, it is useful to consider the case of a cavity formed by two plane mirrors and the propagation of a plane wave through it. This situation is shown in Figure 3.1, with the wave slightly oblique so that the different rays can be easily visualized. The incoming electric E_0 will undergo multiple reflections, resulting in a transmitted electric field and a reflected electric field.

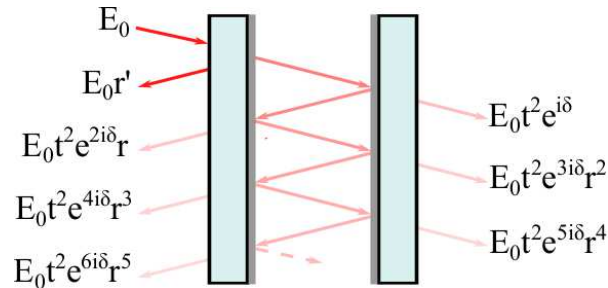


Figure 3.1: Multiple reflection of a plane wave inside a plane mirror cavity. The rays are displayed at a slight angle with the mirror's normal in order to help visualization.

3.1.1 Transmission and reflection coefficients

Let r and r' be the reflection coefficients for the air-glass and glass-air interfaces, respectively, t be the transmission coefficient and δ be the phase gained by the wave when it goes from one mirror to the other. The resultant transmitted electric field will be the sum of electric fields that undergo different numbers of reflections by the mirror before exiting the cavity. The terms on the right side of Figure 3.1 represent those different electric fields. Summing all of those terms, we get the following expression for the transmitted electric field:

$$E_t = E_0 \frac{t^2 e^{i\delta}}{1 - r^2 e^{2i\delta}} \quad (3-1)$$

For the reflected electric field, a similar calculation can be made. The difference is that, instead of a term $E_0 t^2 e^{i\delta}$ representing the transmission through the cavity without any reflection, there will be a term $E_0 r'$ representing the reflection of the electric field by the glass-air interface of the entry mirror. The relation between r and r' is $r = -r'$, a consequence of the 180 degrees phase shift that takes place in a reflection by the interface air-glass. By using this relation, the sum of the terms on the left of Figure 3.1 yields the following expression for the reflected electric field:

$$E_r = E_0 r \left(-1 + \frac{t^2 e^{2i\delta}}{1 - r^2 e^{2i\delta}} \right) \quad (3-2)$$

For an ideal mirror, we have $r^2 + t^2 = 1$, that is, all of the light is either reflected or transmitted by the mirror. Because real mirrors are not perfect, in addition to reflection and transmission through the mirror, we can also consider that part of the light is lost in other processes, such as scattering, absorption and diffraction due to finite size of the mirrors. Because energy must be conserved, we write $r^2 + t^2 = 1 - s^2$, where s^2 is the fraction of the light that is lost. Substituting this conservation relation in equations 3-1 and 3-2 we find the following expressions for the transmission and reflection coefficients of the cavity:

$$T = \frac{|E_t|^2}{|E_0|^2} = \frac{(1 - s^2 - r^2)^2}{(1 - r^2)^2 + 4r^2 \sin^2 \delta} \quad (3-3a)$$

$$R = \frac{|E_r|^2}{|E_0|^2} = r^2 \frac{s^4 + 4(1 - s^2) \sin^2 \delta}{(1 - r^2)^2 + 4r^2 \sin^2 \delta} \quad (3-3b)$$

The transmission coefficient has a maximum for $\delta = n\pi$, while the reflection coefficient has a minimum for that same value. Since δ depends on the cavity length d according to $\delta = kd$, we find the resonance condition for the plane cavity:

$$d = \frac{n\lambda}{2} \quad (3-4)$$

where $n \in \mathbb{Z}$. Figure 3.2 shows the reflection and transmission coefficients as a function of δ for different values of the mirror reflectance $R_m = r^2$, for a cavity with the coefficient $s^2 = 0$.

As it can be seen in Figure 3.2, the larger the mirror reflectance, the narrower the peak -or valley - in the transmission - or reflection - coefficient. The resonance condition can be written in terms of the wave frequency ν :

$$\nu_n = n \frac{c}{2d} \quad (3-5)$$

Since δ is proportional to ν , the dependency of R and T on ν is very similar as the one displayed in Figure 3.2.

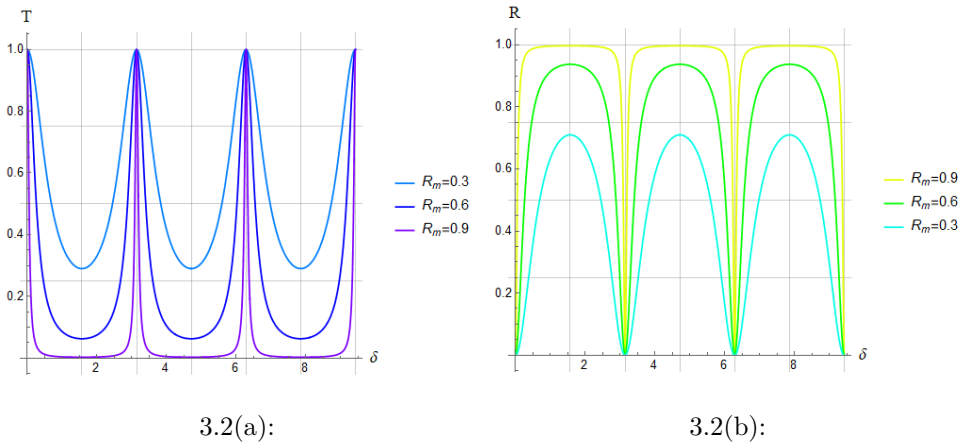


Figure 3.2: Spectra for a plane mirror cavity: (a) transmission spectrum; (b) reflection spectrum.

3.1.2

Important cavity parameters

At this point, it is useful to introduce some important quantities. The first of these quantities is the free-spectral range ν_{FSR} . It is the frequency difference between two resonance frequencies. From equation 3-5 it is easy to see that, for the plane mirror cavity:

$$\nu_{FSR} = \frac{c}{2d} \quad (3-6)$$

The second quantity is the full width at half maximum ν_{FWHM} . As the name suggests, it is the width of the resonance peak measured where the transmission coefficient value is half of its maximum value.

The third quantity is the cavity finesse F . It is given by the ratio between the free spectral range and the full width at half maximum. It is

solely dependent on the cavity losses, not being affected by the cavity length. Mirrors with high reflectance will form high finesse cavities, since their losses are small. Although the finesse can be calculated directly from equations 3-3a and 3-6, there is an approximation that simplifies such calculation.

For large values of mirror reflectance ($R_m \approx 1$), T will be constant and approximately equal to 0 far from the resonance condition, while R will be constant and approximately equal to 1. Both T and R will only vary when the frequency is near a resonance frequency. Therefore, the sine functions in equation 3-11 can be expanded around ν_n , yielding the following expressions for the reflection and transmission coefficients near the n^{th} resonance frequency, for $s = 0$:

$$T_{HR}(\nu) = \frac{((1 - R_m)c/4\pi\sqrt{R_m}d)^2}{((1 - R_m)c/4\pi\sqrt{R_m}d)^2 + (\nu - \nu_n)^2} \quad (3-7a)$$

$$R_{HR}(\nu) = \frac{(\nu - \nu_n)^2}{((1 - R_m)c/4\pi\sqrt{R_m}d)^2 + (\nu - \nu_n)^2} \quad (3-7b)$$

Equation 3-7a for $T_{HR}(\nu)$ is a Lorentzian function in ν centered at ν_n . Therefore, the full width at half maximum is given by:

$$\nu_{FWHM} = 2 \left(\frac{(1 - R_m)c}{4\pi\sqrt{R_m}} \right) \quad (3-8)$$

From equations 3-8 and 3-6, we can write down the following expression for the cavity finesse:

$$F = \frac{\nu_{FSR}}{\nu_{FWHM}} = \frac{\pi\sqrt{R_m}}{1 - R_m} \quad (3-9)$$

Equation 3-9 is consistent with the idea that the finesse is a measurement of how small the cavity losses are, depending solely on the mirror reflectance R_m .

When $s^2 = 0$, the coefficients R and T satisfy $R + T = 1$. Therefore, the transmission spectrum will be given by 1 minus a Lorentzian function. Thus, in order to measure the full width at half maximum of a cavity, both the transmission and reflection spectra can be analyzed.

3.1.3

Losses in the cavity

Finally, let us consider equations 3-3a and 3-3b with $s^2 \neq 0$. Since s only appears in the denominator of these equations, the calculations that led to equation 3-9 for the finesse of a cavity formed by high reflectance mirrors are still valid. Therefore, provided that R_m is fixed, an increase in s^2 won't

decrease the cavity finesse. The main change occurs in the maximum and minimum values of R and T .

The maximum value of T will be reduced from 1 to:

$$T_{max} = \frac{(1 - s^2 - R_m)^2}{(1 - R_m)^2} \quad (3-10)$$

while the minimum and maximum values of R become:

$$R_{min} = \frac{R_m s^4}{(1 - R_m)^2} \quad (3-11a)$$

$$R_{max} = \frac{R_m (s^2 - 2)^2}{(R_m^2 + 1)^2} \quad (3-11b)$$

Furthermore, we note that:

$$R = (1 - s^2) \left(1 - \frac{(1 - R_m)^2 - R_m s^4 / (1 - s^2)}{(1 - R_m)^2 + 4R_m \sin^2 \delta} \right) \quad (3-12)$$

which shows that the reflection spectrum is, in the high reflectance approximation, a constant value minus a Lorentzian function with full width at half maximum equal to that of the transmission spectrum Lorentzian. Once more, both spectra can be analyzed in order to measure the cavity finesse. Figure 3.3 shows these spectra for $s^2 = 0.007$ and two different values of R_m . As it can be seen, the curves corresponding to the high reflectance mirror are more affected by a non-vanishing s^2 . Also, it can be noted that the transmission peak is more attenuated than the reflection valley.

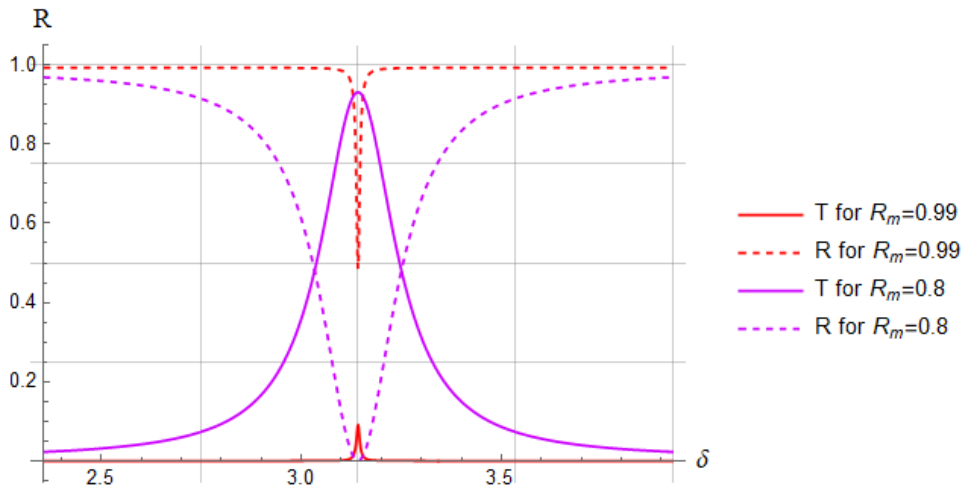


Figure 3.3: Transmission and reflection spectra for cavities formed by mirrors having the same loss coefficient, but different reflectances.

3.2 Gaussian beams and optical cavities

3.2.1 Cavity Modematching

As we've already pointed out, perfectly collimated beams are not solutions to the paraxial approximation. Therefore, if a Gaussian beam is used in a plane mirror cavity, the electric field interference explored in the last section will not occur: the beam will diverge after a few round trips. In order to avoid that from happening, the optical cavity must be formed by at least one concave mirror [37].

If one of the cavity mirrors is concave, a beam with appropriate waist will return to its original shape after one round trip in the cavity. In order to calculate what this waist must be, in terms of the radius of curvature of the mirrors and the cavity length, the $ABCD$ treatment introduced in Chapter 2 can be used.

In this work, only cavities formed by one plane mirror and one concave mirror and cavities formed by two concave mirrors with the same radius of curvature are of interest. Figure 3.4 shows those two kinds of cavities and the system of lenses that are equivalent to them for a beam that is reflected multiple times by the mirrors.

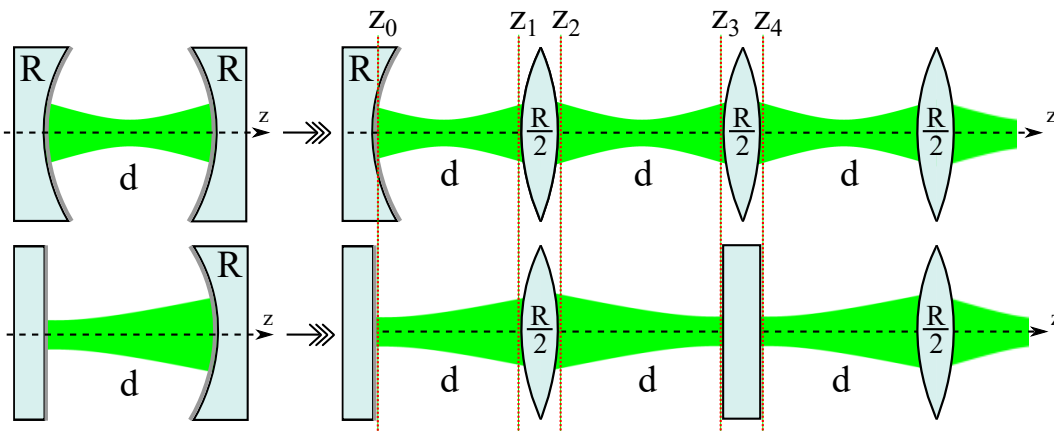


Figure 3.4: Representation of optical cavities as infinite arrays of lenses. Spherical mirrors are represented by thin lenses, while plane mirrors are represented as thin plates.

There are three kinds of propagation in the equivalent lens systems in Figure 3.4:

- propagation in air ($n = 1$) through a distance d ;
- propagation through a thin lens with focal length $R/2$;
- propagation through a thin plane element.

Using the matrices calculated for each of those elements in Chapter 2, we find that the matrices corresponding to the propagation from z_0 to z_4 for the plane-concave and the concave-concave cavities are, respectively, by:

$$M_{cc} = \begin{bmatrix} 1 & 0 \\ -2/R & 1 \end{bmatrix} \begin{bmatrix} 1 & d \\ 0 & 1 \end{bmatrix} \begin{bmatrix} 1 & 0 \\ -2/R & 1 \end{bmatrix} \begin{bmatrix} 1 & d \\ 0 & 1 \end{bmatrix} \quad (3-13a)$$

$$M_{pc} = \begin{bmatrix} 1 & 0 \\ 0 & 1 \end{bmatrix} \begin{bmatrix} 1 & d \\ 0 & 1 \end{bmatrix} \begin{bmatrix} 1 & 0 \\ -2/R & 1 \end{bmatrix} \begin{bmatrix} 1 & d \\ 0 & 1 \end{bmatrix} \quad (3-13b)$$

Since the beam must return to its initial shape after one round trip, we impose that $q_4 = q_0$, with q_4 being given by equation 2-26:

$$q_0 = \frac{Aq_0 + B}{Cq_0 + D} \quad (3-14)$$

where the values of A, B, C, D are given by the matrices M_{cc} or M_{pc} . By doing this, we find:

$$q_{0,cc} = \frac{1}{2} \left(-d \pm \sqrt{d(d - 2R)} \right) \quad (3-15a)$$

$$q_{0,pc} = \pm \sqrt{d(d - R)} \quad (3-15b)$$

According to the relations in equation 2-24, q must have a imaginary part. This leads to the necessary conditions for cavity stability: $d_{cc} < 2R$ for the concave-concave cavity and $d_{pc} < R$ for the concave-plane cavity. Also, from equation 2-24, the imaginary part must be positive. This leads to:

$$q_{0,cc} = \frac{1}{2} \left(-d_{cc} + i\sqrt{d_{cc}(2R - d_{cc})} \right) \quad (3-16a)$$

$$q_{0,pc} = i\sqrt{d_{pc}(R - d_{pc})} \quad (3-16b)$$

The beam waist is located at the point where $Re(q) = 0$. That means that in the concave-concave cavity, it is located in the middle of the cavity, and for the plane-concave, it is located at the surface of the plane mirror. Using equations 2-24 and 3-16 to calculate the waists of the cavity, we find [37]:

$$\omega_{0,cc}^2 = \frac{\lambda}{2\pi} \sqrt{d_{cc}(2R - d_{cc})} \quad (3-17a)$$

$$\omega_{0,pc}^2 = \frac{\lambda}{\pi} \sqrt{d_{pc}(R - d_{pc})} \quad (3-17b)$$

Therefore, the radius of curvature combined with the cavity length fully determine the cavity waist. Figure 3.5 shows the cavity waist as a function of cavity length for both types of cavity, for $\lambda = 780$ nm and $R = 5$ cm, which

are the values we are going to use later in this work. As it can be seen, the maximum waist is equal for both cavities, and is achieved for a cavity length equal to the maximum possible cavity length.

In order to achieve good cavity performance, the beam waist and the cavity waist must have the same size and same location. A beam that satisfies this condition is said to be modematched. Usually, modematching is done by placing a lens before the cavity, in order to change the initial beam waist and its location so that they match the cavity waist parameters. Alternatively, the beam waist size and location can be measured, and the cavity length can be chosen so that its waist match the measured beam waist.

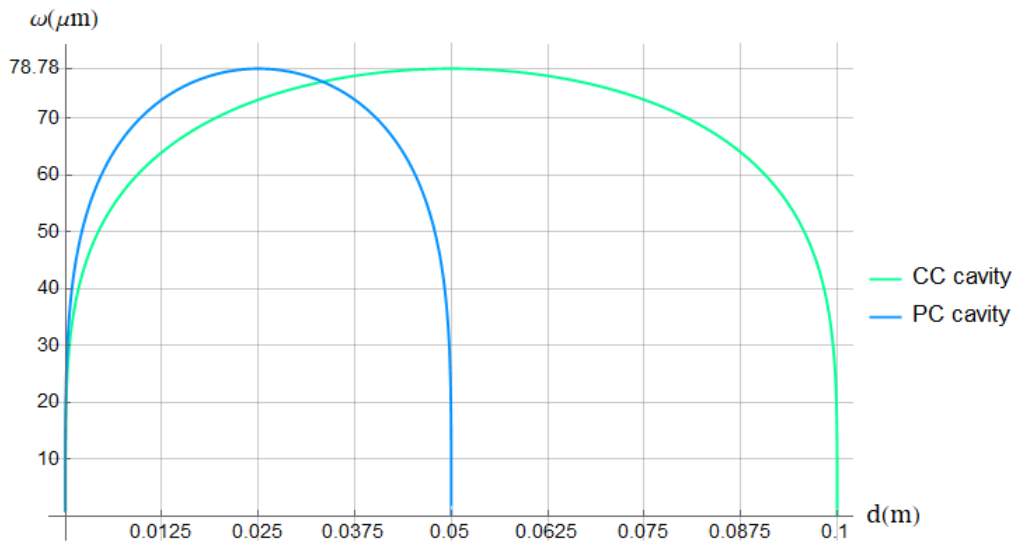


Figure 3.5: Cavity's waist as a function of the cavity's length.

Further modematching calculations involve taking into consideration the entry mirror thickness, as well as the lensing effect caused by it. For a plane mirror, the beam waist is not affected, but its location is. For a concave mirror, both the beam waist and the waist location are changed. These calculations are very specific, and we'll get into more details about them when the real cavity assembling is described in Chapter 4.

Finally, we note that, since calculations involving the parameter q also hold for Hermite-Gauss and Laguerre-Gauss modes, equation 3-17 also holds for higher order beams.

3.2.2 Higher order modes resonance

In the first section of this chapter we discussed the resonance condition for a plane wave inside a cavity. The condition we found $\delta = n\pi$ was derived from

the fact that the transmission coefficient had a maximum when this condition was satisfied. Had we performed the transmission and reflection coefficients calculations for a modematched beam - that is, a beam that would preserve its shape after any number of round trips, allowing interference to take place - the result would have been the same. The phase increment δ , though, would depend on the chosen beam.

This phase can be easily calculated from equations 2-17a and 2-17b for the electric fields of a Hermite-Gauss mode and a Laguerre-Gauss mode, respectively. In the case of a plane-concave cavity, the beam waist is located at the entry mirror surface, and the phase can be calculated by setting $z = d_{pc}$ in equations 2-17a and 2-17b:

$$\delta_{mn,pc}^{HG} = kd_{pc} - (1 + m + n) \arctan \frac{d_{pc}}{z_R} \quad (3-18a)$$

$$\delta_{lp,pc}^{LG} = kd_{pc} - (1 + 2p + l) \arctan \frac{d_{pc}}{z_R} \quad (3-18b)$$

Now, from the condition $\delta = n\pi$ and using equation 3-17b to substitute the ω_0^2 in z_R , we find the resonance conditions [38]:

$$\frac{\nu_{pc,jmn}}{\nu_{FSR}} = j + \frac{1}{\pi}(1 + m + n) \arcsin \sqrt{\frac{d_{pc}}{R}} \quad (3-19a)$$

$$\frac{\nu_{pc,jlp}}{\nu_{FSR}} = j + \frac{1}{\pi}(1 + 2p + l) \arcsin \sqrt{\frac{d_{pc}}{R}} \quad (3-19b)$$

where j is the number of half-wavelengths of the resonant wave inside the cavity and ν_{FSR} is the free spectral range of a plane mirror cavity with length d_{pc} . If we calculate the difference between two resonant frequencies either for a Hermite-Gauss mode or for a Laguerre-Gauss mode, we see that the free spectral range still is ν_{FSR} .

For a concave-concave cavity, because the beam waist is at the center of the cavity, the phase would be two times the phase we get by setting $z = d_{cc}/2$ in equations 2-17a and 2-17b. Performing a calculation similar to the one performed for the plano-concave cavity, using equation 3-17a for ω_0^2 , yields [38]:

$$\frac{\nu_{cc,jmn}}{\nu_{FSR}} = j + \frac{2}{\pi}(1 + m + n) \arcsin \sqrt{\frac{d_{cc}}{2R}} \quad (3-20a)$$

$$\frac{\nu_{cc,jlp}}{\nu_{FSR}} = j + \frac{2}{\pi}(1 + 2p + l) \arcsin \sqrt{\frac{d_{cc}}{2R}} \quad (3-20b)$$

Once again, the free spectral range is given by c/d_{cc} . It is clear from equations 3-19 and 3-20 that different order modes have different resonance

frequencies. Therefore, if the beam used to pump the cavity is not a pure Hermite-Gauss or Laguerre-Gauss mode, the resonant mode inside the cavity can be selected by varying the laser frequency.

Suppose, for example, that a Gaussian beam is used to pump a concave-concave cavity, but it is slightly misaligned by a small angle θ with the cavity axis - that is, the axis that join the two mirrors and is orthogonal to both of them - as shown in Figure 3.6(b). If we define the cavity's axis as the z -axis, the beam's electrical field can be written as a Gaussian beam $\vec{E}^G(x', y', z') = E_0 e^{ik_m z'} u_{00}(x', y', z') \hat{e}$ in a coordinate system $x'y'z'$ rotated by an angle θ around the y axis. Then, in the xyz coordinate system, the electrical field is given, to first order in θ , by $\vec{E}^G(x + z\theta, y, z - x\theta) = [E_0 e^{-ik_m \theta x} u_{00}(x + z\theta, y, z - x\theta)] e^{ik_m z} \hat{e}$.

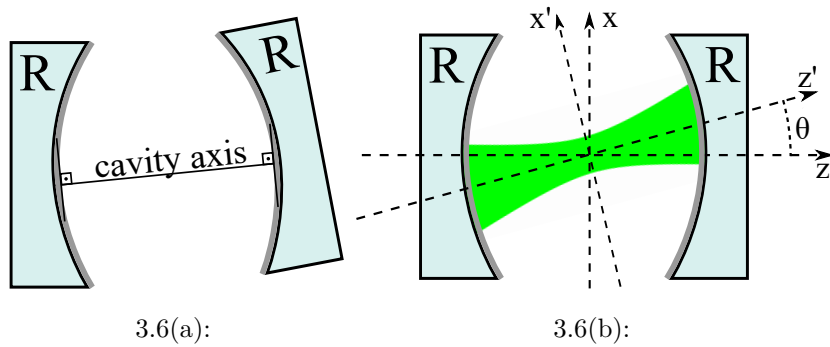


Figure 3.6: Representation of misalignment situations: (a) misalignment between two spherical mirrors, implying a new cavity axis; (b) misalignment between the beam and the cavity axis.

Now, as discussed in the first section of the second chapter of this work, the term $E_0 e^{-ik_m \theta x} u_{00}(x + z\theta, y, z - x\theta)$ beam can be decomposed in the Hermite-Gauss basis of the xyz coordinate system [36], resulting in Hermite-Gauss beams with different powers P_{mn} given by equation 2-22, with the coefficients C_{mn}^F calculated from equation 2-20 for $F(x, y, 0) = E_0 e^{-ik_m \theta x} u_{00}(x, y, -x\theta)$. Table 3.1 shows the ratio between the power P_{m0} contained in low order Hermite-Gauss modes and the total power in the $z = 0$ plane for different misalignment angles θ . For this simulation, we consider $\lambda = 780 \text{ nm}$ and $\omega_0 = 60 \mu\text{m}$.

$\theta \backslash m$	0	1	2	3
$0 \times 10^{-4} \text{rad}$	1.00	0.00	1.41×10^{-32}	1.55×10^{-36}
$1 \times 10^{-4} \text{rad}$	0.999	5.84×10^{-4}	1.70×10^{-7}	3.17×10^{-11}
$2 \times 10^{-4} \text{rad}$	0.998	2.33×10^{-3}	2.72×10^{-6}	2.10×10^{-9}
$3 \times 10^{-4} \text{rad}$	0.995	5.23×10^{-3}	1.37×10^{-5}	2.40×10^{-8}
$4 \times 10^{-4} \text{rad}$	0.991	9.26×10^{-3}	4.33×10^{-5}	1.34×10^{-7}

Table 3.1: Ratio between mode power and total power for different Hermite-Gauss modes and different angles between the beam's axis and the cavity's axis.

As it can be seen, as θ increases, more power is concentrated in modes with larger m index. If a frequency sweep is performed in the laser used to pump the cavity, as long as θ remains much smaller than the divergence angle of the beam in the far-field [36], secondary peaks will appear at the frequencies correspondent to these $m \neq 0$ Hermite-Gauss modes, as we will see in the next chapter when the experimental realizations are discussed. Similar calculations hold if the beam axis is slightly translated with respect to the cavity axis, if the beam waist doesn't match the cavity waist, or if the beam waist location doesn't match the cavity waist location [36]. In the case of a waist mismatch, Laguerre-Gauss modes would be produced.

4 Optical Cavities: Experiment

In this chapter we describe the experimental implementation of three types of optical cavities: a cavity formed by a plane mirror and a concave mirror, a cavity formed by two concave mirrors in a non-confocal configuration and a cavity formed by two concave mirrors in the confocal configuration. Based on the measurements of the finesse, the transmission and the reflectivity for each one of them, we discuss which type is more adequate for our future applications and how our setup might be further improved. We also present some small changes in the calculations presented in the last chapter that allows us to apply them to our specific experimental setups.

Figure 4.1 shows the setup used in the implementation of the three kinds of cavity. A 780nm laser beam is collimated by a lens with focal distance f_1 , passes through a quarter-wave plate (QWP) and a half-wave plate (HWP), acquiring linear polarization, and gets transmitted by a polarizing beam splitter (PBS). Then it passes through a quarter-wave plate, acquiring circular polarization, and is focused by a lens with focal distance f_2 in order to get modematched to the cavity. It is then reflected by two mirrors - SM1 and SM2 - which align the beam with the cavity axis.

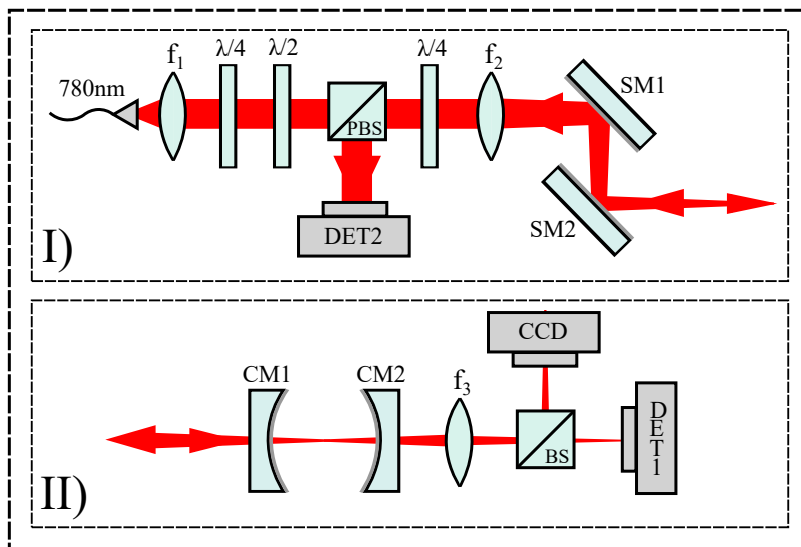


Figure 4.1: Schematic of the setup implemented in our laboratory in order to study different types of cavities.

The light transmitted by the cavity - formed by the mirrors CM1 and CM2 - is focused by a lens with focal distance f_3 , splitted by a beam splitter (BS), and half of it is focused on a CCD sensor, that allows for visualization of the transmitted mode, and half of it is focused on a detector DET1 that allows for measurement of the transmitted intensity. The light reflected by the cavity passes through the quarter-wave plate once more, acquiring linear polarization, and is reflected by the PBS onto a second detector DET2 that allows for the measurement of the reflected intensity.

The specific values regarding the optical elements used in each type of cavity are presented in the next sections of this chapter.

4.1

General aspects

4.1.1

Theory extensions

The laser we use is an external cavity laser (Toptica DL pro 780 nm). By changing the voltage applied to the diffraction grating's piezoelectric actuator, we can control the laser wavelength, which has a linear response to the applied voltage. Therefore, in our experiment, we measure the cavity's transmission and reflection as a function of this voltage. In the previous chapter our results were derived using the laser frequency as the variable. Thus, it is useful to derive the formulas replacing the frequency by the voltage applied to the piezoelectric actuator.

Since the wavelength response to the voltage is linear, we can write:

$$\lambda(V) = \lambda_0 + \alpha(V - V_0) \quad (4-1)$$

where V is the applied voltage, V_0 is the voltage offset, α is the proportionality constant, which might be positive or negative, and λ_0 is the wavelength when the voltage is equal to its offset value.

From equation 3-6, we know that that the n^{th} resonance frequency is given by $nc/2d$. Then, the n^{th} resonance wavelength is given by $2d/n$. Thus, the voltage difference between two resonance voltages is:

$$V_{FSR,n} = \frac{|\lambda_n - \lambda_{n+1}|}{|\alpha|} = \frac{2d}{|\alpha|n(n+1)} \approx \frac{\lambda_n^2}{2|\alpha|d} \quad (4-2)$$

where the absolute value of α is used due to the possibility of it being negative, which would lead to the resonance voltage V_n being smaller than the resonance voltage V_{n+1} . The approximation relies on the fact that $n \gg 1$, since it is the number of half wavelengths present in the stationary wave inside the cavity.

Now, for a small variation δv_n of the frequency around v_n , we have:

$$\delta v_n = -\frac{c\alpha\delta V_n}{(\lambda_0 + (V_n - V_0)\alpha)^2} = -\frac{c\alpha}{\lambda_n^2}\delta V_n \quad (4-3)$$

Therefore, we can replace $v - v_n = \delta v_n$ in Equation 3-7a by $-c\alpha\delta V_n/\lambda_n^2$, which will yield a Lorentzian function with full width at half maximum given by:

$$V_{FWHM,n} = \frac{\lambda_n^2}{|\alpha|c}v_{FWHM} \quad (4-4)$$

We then define the quantity $F = V_{FSR,n}/V_{FWHM,n}$, given by:

$$F_V = \frac{V_{FSR,n}}{V_{FWHM,n}} = \frac{\lambda_n^2}{|\alpha|c}v_{FWHM} \times \frac{2|\alpha|d}{\lambda_n^2} = \frac{v_{FWHM}}{v_{FSR}} = F \quad (4-5)$$

Therefore, we can measure the cavity finesse by dividing the voltage difference between two resonance voltages by the full width at half maximum of the transmission peak that appears in the measured transmission when scanning the applied voltage. Furthermore, we notice that, since $n \gg 1$, $\lambda_n - \lambda_{n+1} = 2d/(n(n+1)) \approx 0$, which implies that λ_n is approximately constant, and, therefore, so are $V_{FSR,n}$ and $V_{FWHM,n}$.

Another extension has to be made regarding the transmission and reflection coefficients. In the previous chapter, we assumed that both mirrors had the same parameters r^2 , t^2 and s^2 . For the plano-concave cavities, we use two mirrors with different coatings and, therefore, different parameters. This can be easily incorporated in the calculations previously presented. Let R_{m1} and s_1^2 be the reflection and loss coefficients, respectively, for the first mirror and R_{m2} and s_2^2 be the reflection and loss coefficients for the second mirror. Then, the cavity's transmission and reflection coefficients are given by:

$$T = \frac{(1 - s_1^2 - R_{m1})(1 - s_2^2 - R_{m2})}{(1 - \sqrt{R_{m1}R_{m2}})^2 + 4\sqrt{R_{m1}R_{m2}}\sin^2\delta} \quad (4-6a)$$

$$R = \frac{(\sqrt{R_{m1}} + \sqrt{R_{m2}}(s_1^2 - 1))^2 + 4(1 - s_1^2)\sqrt{R_{m1}}\sqrt{R_{m2}}\sin^2\delta}{(1 - \sqrt{R_{m1}R_{m2}})^2 + 4\sqrt{R_{m1}R_{m2}}\sin^2\delta} \quad (4-6b)$$

For a high finesse cavity, the same considerations made in section 3.1.2 can be applied, and the transmission coefficient near resonance will be given, approximately, by a Lorentzian function, while the reflection coefficient will be a constant value minus a Lorentzian function. In the present case, however, the full width at half maximum, in the frequency spectrum, is:

$$v_{FWHM} = 2\frac{(1 - \sqrt{R_{m1}R_{m2}})c}{4\pi\sqrt[4]{R_{m1}R_{m2}}} \quad (4-7)$$

which implies that the finesse will be:

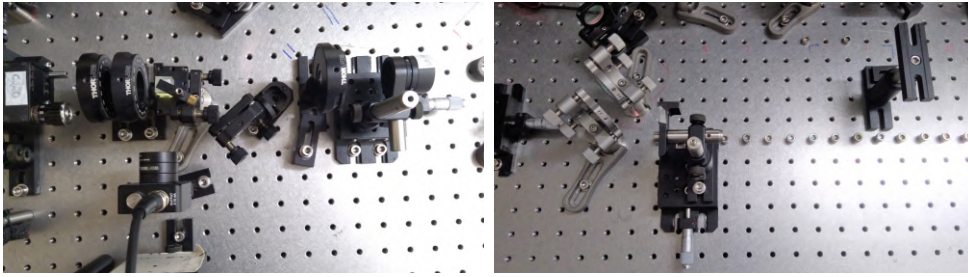
$$F = \frac{v_{FSR}}{v_{FWHM}} = \frac{\pi\sqrt[4]{R_{m1}R_{m2}}}{1 - \sqrt{R_{m1}R_{m2}}} \quad (4-8)$$

We are now ready to present our experimental results.

4.1.2

Experimental procedure

For all of our cavity setups we follow the same initial procedure. First, we start by placing all the optical elements shown in Part I of Figure 4.1, as shown in Figure 4.2(a). The mirrors SM1 and SM2, in particular, are mounted on stable mountings (Thorlabs Polaris K1) in order to have precision during the alignment procedure. The laser is coupled to a fiber in order to get a Gaussian mode from its initial elliptical mode, and then collimated by an aspheric lens. The achromatic quarter-wave plate and the half-wave plate are adjusted so that the transmission through the PBS is maximized.



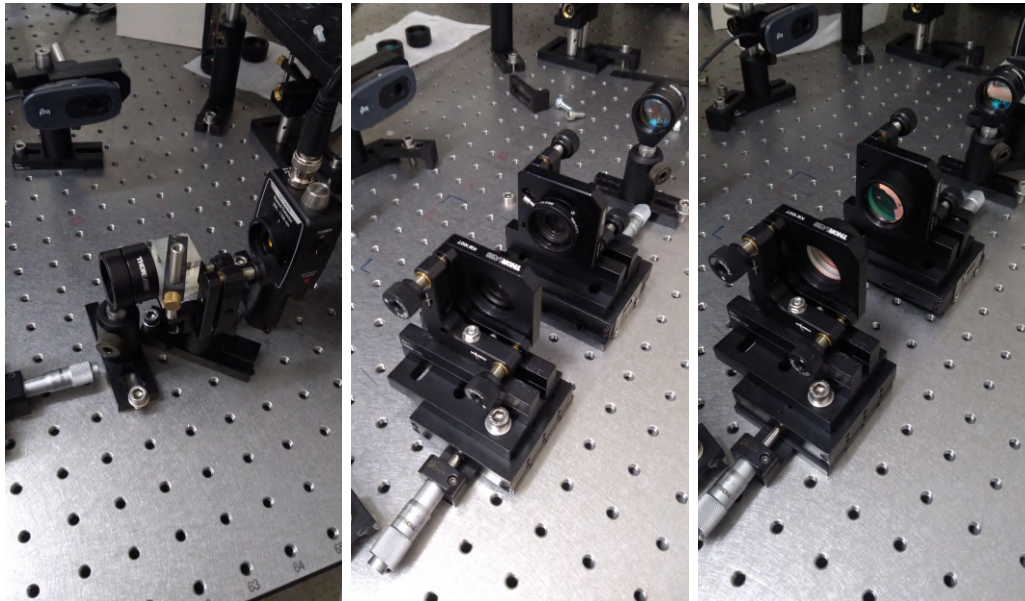
4.2(a):

4.2(b):

Figure 4.2: Initial steps for the implementation of the optical cavities. (a) Optical elements corresponding to Part I of Figure 4.1 (b) Measurement of the beam's waist and its location by the knife edging method.

A doublet lens with focal distance ranging from 200 mm to 300 mm is placed and the waist of the beam and its location are measured by applying the knife-edge method [39], as shown in Figure 4.2(b), after the steering mirrors SM1 and SM2, and fitting the data to the curve given by Equation 2-13a by means of the method of least squares. Based on the measured values, the cavity length is determined using Equations 3-17b or 3-17a.

Before placing the cavity mirrors, the remaining components shown in Part II of Figure 4.1 are placed, as shown in Figure 4.3(a). First, the lens ($f_3 = 75$ mm) and the beam splitter are placed. Then, the CCD camera (Logitech C310) and the detector DET1 (Thorlabs DET36A2) are placed so that the beam is focused in the center of both sensors.



4.3(a):

4.3(b):

4.3(c):

Figure 4.3: Optical elements corresponding to Part II of Figure 4.1. (a) Optical elements used to monitor the field transmitted by the cavity. (b) Cavity's mirrors are replaced by irises during the alignment procedure. (c) Implemented optical cavity.

The mounts for the mirrors CM1 and CM2 are placed, on top of translation stages, using a digital caliper rule in order to have more precision over their positions. We use threaded mirror mounts (Thorlabs KM100T) that allow for quick assemble of the mirrors whenever necessary, without the need to undo the setup. Also, it allows for placing an iris instead of the mirror, as shown in Figure 4.3(b), which is necessary during alignment.

For aligning the cavity, we follow an iterative procedure. First, the second mirror translation stage is moved until the cavity has the desired length, within 0.01 mm precision, provided by the digital caliper rule. Then, two irises are threaded to the mountings, and the steering mirrors are used in order to make the beam pass through both irises, which are then removed from the mountings. The second mirror is then threaded to its mount, which is used to make the reflected beam match the incoming beam. Then, the same thing is done for the first mirror. When the mounts are adjusted, the cavity length is changed. Thus, this procedure has to be repeated until three conditions are satisfied: the cavity length must be the desired one, the beam must pass through the irises and the reflection of both mirrors must match the incoming beam. Figure 4.3(c) shows the two concave mirrors in place.

The fine alignment is made using the signals from the CCD camera

(transmitted light image) and the detector DET1 (transmission as a function of the applied voltage). The cavity wavelength is scanned using a triangle waveform with a frequency chosen from a range between 1 Hz and 10 Hz and the transmitted modes are observed by the camera. The voltage scan amplitude and offset are set so that only the fundamental mode is transmitted. By doing so, a single peak is observed in the detector's signal. Then the steering mirrors are used to maximize the amplitude of this peak. After doing this, different voltage ranges can be scanned, and the secondary peaks can be minimized. The camera's image is useful in order to know the misalignment direction. The transmission of the $m = 1, n = 0$ Hermite-Gauss mode, for example, indicates that there is a horizontal misalignment.

Finally, the second quarter-wave plate is adjusted so that the beam reflected by the cavity is reflected by the PBS. The reflected beam is then focused on detector DET2 (Thorlabs DET100A2), which is used to measure the cavity reflection as the voltage is scanned. Since this reflected beam has a power of approximately 50 mW, two neutral density filters (Thorlabs NE04A and Thorlabs NE10A) are placed in front of the detector to avoid saturation. Figure 4.4 shows the complete setup.

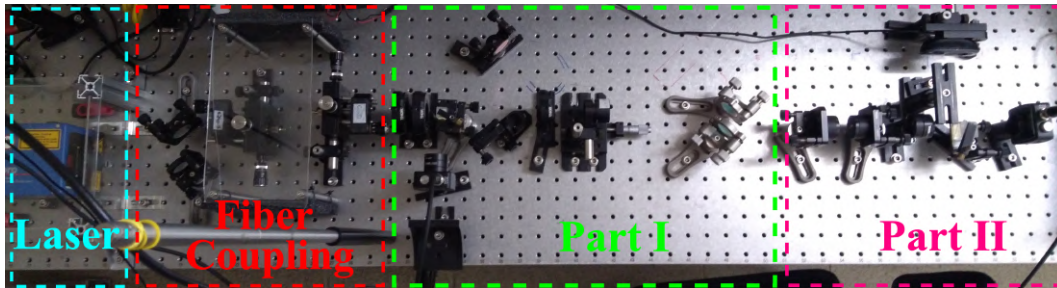


Figure 4.4: Complete optical setup used in the implementation of our optical cavities.

4.2

Plano-Concave cavity

The first cavity we implemented was a plano-concave cavity. In this implementation, the lens used to collimate the beam has a focal distance f_1 of 11.0 mm (Thorlabs C220TME-B), resulting in a collimated beam waist of 1.05 mm. The lens used for the modematching has a focal distance f_2 of 300 mm, resulting in a waist of $68.2 \mu\text{m}$ located at $z_0 = -12.81 \text{ cm}$, which is measured with relation to a pedestal that is fixed to the table and defined as the origin of our z axis.

Since the plane mirror (Thorlabs BB111-E03P-SP) has a thickness d of 6.0 mm, the q parameter is changed when the beam gets transmitted by the mirror, which acts like a thick plate. If the mirror front surface is placed at $z = z_{m1}$, as shown in Figure 4.5, then the back surface of the mirror is located at $z = z_{m1} - d$, and the q parameter before the mirror is given by:

$$q_{before} = q_0 - (z_0 - (z_{m1} - d)) \quad (4-9)$$

where q_0 is the q parameter at z_0 , that is, at the waist. Since the mirror acts as a thick plate, the q parameter after the mirror front surface is given by:

$$q_{after} = q_{before} + d/n = q_0 - z_0 + z_{m1} - d + d/n \quad (4-10)$$

where n is the plate's refractive index. Now, for a plano-concave cavity, the cavity waist is located at the plane mirror surface. Therefore, we want $\Re(q_{after}) = 0$, which leads to:

$$z_{m1} = z_0 + d \left(1 - \frac{1}{n}\right) \quad (4-11)$$

This is where the mirror's front surface should be located in order to achieve modematching between the cavity and the beam. For $n = 1.46$ (fused Silica) and $d = 6.00$ mm, this yields $z_{m1} = -12.62$ cm for our case.

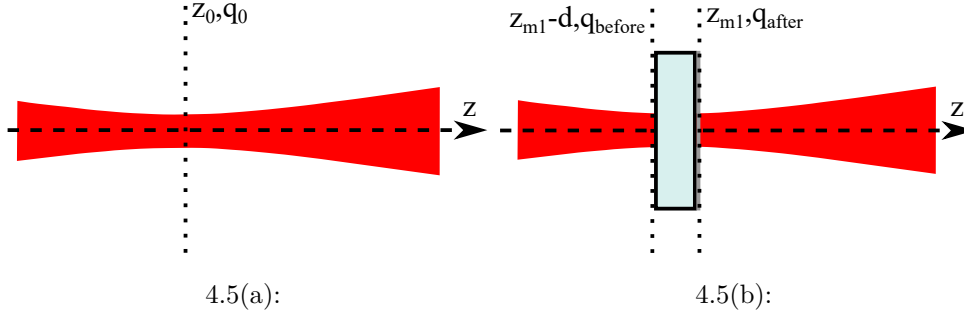


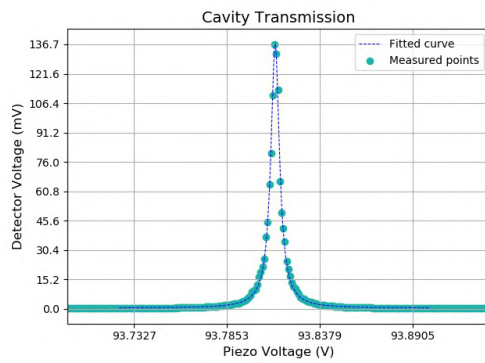
Figure 4.5: Schematic showing the coordinates and parameters used in the modematching calculation. (a) Parameter q_0 at the coordinate z_0 of the beam waist. (b) Parameter q before and after a plane mirror of thickness d .

The waist size doesn't get affected by the mirror, which means we want the cavity to have a waist of $68.3 \mu\text{m}$. Using Equation 3-17b, for a radius of curvature of the second mirror (Thorlabs CM254-025-E03P-SP) equals to 5.00 cm, we get that the cavity's length L should be 4.15 cm. Therefore, the second mirror's position should be $z_{m2} = -8.47$ cm.

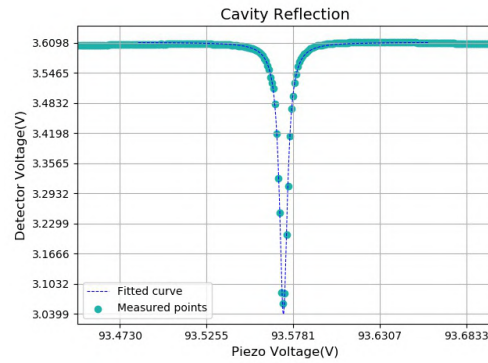
As we've said in the first section, we scan the piezoelectric's voltage and measure the cavity's transmission and the cavity's reflection intensities, and we observe the transmitted mode using the CCD camera. Both the transmission

peaks and the reflection valleys are fitted to a Lorentzian function plus a constant value. For the transmission, this constant valley is mainly due to the detector's noise, while for the reflection, it is mainly due to the light that is reflected when there is no resonance. From now on, we'll refer to the Lorentzian function's full width at half maximum, amplitude and center coordinate as A , δV and V_0 , respectively, and to the constant value as C_0 .

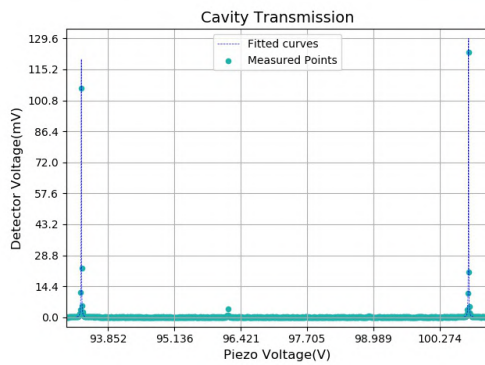
Figures 4.6(a), 4.6(b) and 4.6(c) show, respectively, a transmission main peak, a reflection main valley and two consecutive main peaks. For the transmission peak, we found $A = 137$ mV, $\delta V = 5.90$ mV, $V_0 = 93.8$ V and $C_0 = 0.297$ mV, and for the reflection valley, $A = -0.571$ V, $\delta V = 5.71$ mV, $V_0 = 93.6$ V and $C_0 = 3.61$ V. The distance between the two consecutive peaks was found to be 7.50 V.



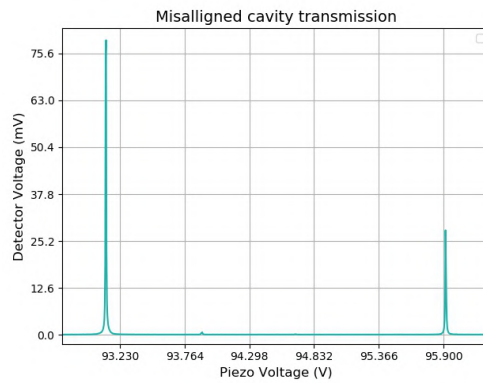
4.6(a):



4.6(b):



4.6(c):



4.6(d):

Figure 4.6: Transmission and reflection spectra for the plano-concave cavity. (a) Plano-concave cavity's single transmission peak. (b) Plano-concave cavity's single reflection valley. (c) Plano-concave cavity's consecutive transmission peaks. (d) Transmission and reflection spectra for the plano-concave cavity.

The cavity maximum transmission is measured in a two steps procedure.

The first of them is measuring the same transmission peak 20 times and averaging all the fitted A 's. This yielded a maximum transmission of 141 ± 5 mV. The second step is converting this value to power units and dividing it by the laser power measured by the detector before the cavity is placed, which was measured to be 22.2 mW. The voltage response of the detector DET1 is given by:

$$V_D = aP + b \quad (4-12)$$

where a was measured to be (4.70 ± 0.00) mV/ μ W and b was measured to be (-12.5 ± 2.2) mV. Therefore, the cavity transmission coefficient during resonance is $(0.147 \pm 0.005)\%$.

The cavity finesse is also measured in two steps. The first of them is measuring the same transmission peak 20 times and averaging all the fitted δV 's. This yielded (6.34 ± 0.58) mV. The second step is measuring two consecutive peaks 20 times and averaging all the voltage differences $V_{0,2} - V_{0,1}$. This yielded (7.42 ± 0.00) V. By dividing the averaged voltage difference by the averaged full width at half maximum, the finesse was calculated to be 1172 ± 101 .

Using the values measured for the maximum transmission and for the finesse, we can use Equations 4-6a and 4-8 to write down two equations relating R_{m1} , R_{m2} , s_1^2 and s_2^2 :

$$(1.47 \pm 0.05) \times 10^{-3} = \frac{(1 - s_1^2 - R_{m1})(1 - s_2^2 - R_{m2})}{(1 - \sqrt{R_{m1}R_{m2}})^2} \quad (4-13a)$$

$$1172 \pm 108 = \frac{\pi \sqrt[4]{R_{m1}R_{m2}}}{1 - \sqrt{R_{m1}R_{m2}}} \quad (4-13b)$$

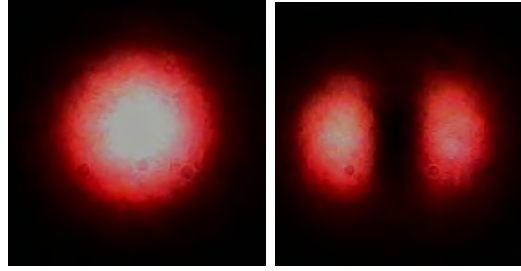
We'll solve equations 4-13 for R_{m1} and s_1^2 in the next section, when the two concave cavity mirrors are assumed to be identical, allowing for the calculation of R_{m2} and s_2^2 .

To exemplify the beam decomposition presented in Table 3.1, we misalign the cavity in the horizontal direction using the steering mirror SM2. Figure 4.6(d) shows the transmission curve for the misaligned cavity. The voltage difference between the two peaks is 2.80 V. By scanning each peak separately, we observe the transmitted modes shown in Figure 4.7, confirming that the largest peak is due to transmission of the fundamental Gaussian mode, while the other peak is due to resonance of the $m = 1, n = 0$ Hermite-Gauss mode.

We can find out whether the coefficient α in Equation 4-1 is positive or negative using Equation 3-19a and the ratio $2.8/7.4 \approx 0.378$ between the

distance between the secondary peak and the main peak shown in Figure 4.6(d) and the distance between two main peaks. First of all, we rewrite Equation 3-19a in terms of the resonance voltage:

$$V_{pc,jmn} = V_0 + \frac{1}{\alpha} \left[-\lambda_0 + \frac{c}{v_{FSR}} \left(j + \frac{1}{\pi} (1 + m + n) \arcsin \sqrt{\frac{d_{PC}}{R}} \right)^{-1} \right] \quad (4-14)$$



4.7(a):

4.7(b):

Figure 4.7: Cavity transmission patterns when the cavity is horizontally misaligned and the voltage is scanned around different resonant voltages. (a) Cavity transmission pattern corresponding to the fundamental mode. (b) Cavity transmission pattern corresponding to the $m = 1, n = 0$ Hermite-Gauss mode.

If $\alpha > 0$, a lower voltage implies a shorter wavelength, which implies a higher number of half wavelengths inside the cavity. In this case the lower voltage main peak would correspond to the mode $j + 1, 0, 0$, the secondary peak would correspond to the mode $j, 1, 0$ and the higher voltage main peak would correspond to the mode $j, 0, 0$. Then, the ratio would be given by:

$$\frac{V_{j,1,0} - V_{j+1,0,0}}{V_{j,0,0} - V_{j+1,0,0}} \approx 1 - \frac{1}{\pi} \arcsin \sqrt{\frac{d_{pc}}{R}} \quad (4-15)$$

which equals 0.635 for our case. On the other hand, if $\alpha < 0$, the lower voltage main peak would correspond to $j, 0, 0$, the secondary peak would correspond to $j, 1, 0$ and the higher voltage main peak would correspond to $j + 1, 0, 0$. The ratio, then, would be given by:

$$\frac{V_{j,1,0} - V_{j,0,0}}{V_{j+1,0,0} - V_{j,0,0}} \approx \frac{1}{\pi} \arcsin \sqrt{\frac{d_{pc}}{R}} \quad (4-16)$$

which is equal to 0.365 for our case. Since the measured value for this ratio is 0.378, we get that α is negative. Therefore, the higher the voltage, the shorter the wavelength.

We can also estimate the magnitude of α . We can use Equation 4-2 with $V_{FSR,n} = 7.42 \text{ V}$, $d = 4.15 \text{ cm}$ and $\lambda_n \approx 780 \text{ nm}$ to find that $\alpha \approx -1 \text{ pm/V}$

4.3

Concave-concave cavity

The second type of cavity we implemented was a concave-concave cavity formed by two identical concave mirrors (Thorlabs CM254-025-E03P-SP). The lens used to collimate the beam has a focal distance f_1 of 15.36 mm (Thorlabs C260TME-B), resulting in a collimated beam waist of 1.43 mm. The lens used for the modematching has a focal distance f_2 of 300 mm, resulting in a waist ω_0 of $52.6 \mu\text{m}$ located at $z_0 = 15.59 \text{ cm}$.

The modematching calculation for this case is more complex than in the plano-concave case. If the first mirror's front surface is placed at $z = z_{m1}$, then the back surface is located at $z = z_{m1} - d$, where d is the mirror's center thickness, and the q parameter just before the back surface is $q_{before} = q_0 - (z_0 - (z_{m1} - d))$. The concave mirror doesn't act just as a thick plate, but rather as a thick plate followed by a thin lens. According to the lens maker's equation, the focal distance of this lens is given by:

$$\frac{1}{f} = (n - 1) \left(\frac{1}{R_1} - \frac{1}{R_2} \right) \quad (4-17)$$

where n is the lens refractive index and R_1 and R_2 are the radius of curvature of the lens surfaces. In our case, $R_1 = \infty$ (plane surface), $R_2 = 50.0 \text{ mm}$ and $n = 1.53$.

The q parameter at a coordinate $z > z_{m1}$ can be calculated starting from q_{before} by calculating the matrix corresponding to the following propagation:

- propagation through a plate with thickness d ;
- propagation through a thin lens with focal distance f given by Equation 4-17;
- propagation through a distance $z - z_{m1}$.

This will yield a matrix $ABCD$ that depends on z_{m1} and z . Using Equation 2-26 for calculating $q(z)$ and making $\Re(q(z'_0)) = 0$ we can find the new waist location z'_0 as a function of z_{m1} . The new beam waist ω'_0 can be calculated from the imaginary part of $q(z'_0)$. Finally, we impose that ω'_0 is the waist corresponding to a cavity with length $L = 2(z'_0 - z_{m1})$, since the waist must be located at the center of the cavity. This is done using Equation 3-17a, yielding the coordinate z_{m1} where the first mirror's front surface must be placed. Substituting this value into z'_0 , we can calculate the cavity length $L = 2(z'_0 - z_{m1})$.

The calculation described in the above paragraph is quite extensive, and results in analytical expressions that are not very elusive. Therefore, the details regarding it are omitted here. For our case $d = 6.00$ mm, $n = 1.53$, $R_{m1} = R_{m2} = 50.0$ mm, $z_0 = 15.59$ cm and $\omega_0 = 52.6$ μ m which leads to $z_{m1} = 11.12$ cm, $\omega'_0 = 74.35$ μ m and $L = 7.27$ cm.

Figures 4.9(a), 4.9(b) and 4.9(c) show, respectively, a transmission main peak, a reflection main valley and two consecutive main peaks. For this particular transmission peak, we found $A = 7.85$ mV, $\delta V = 4.86$ mV, $V_0 = 92.1$ V and $C_0 = 0.0435$ mV, and for this particular reflection valley, $A = -41.2$ mV, $\delta V = 4.52$ mV, $V_0 = 931.5$ V and $C_0 = 3.04$ V. The distance between the two consecutive peaks was found to be 4.33 V.

We measure the cavity transmission during resonance following the same procedure described for the plano-concave mirror, which yielded a voltage of (8.24 ± 0.31) mV and, therefore, a laser power of (4.41 ± 0.47) μ W. The laser power measured without the cavity was again 22.2 mW, resulting in a transmission during resonance of $(0.0198 \pm 0.0021)\%$. The finesse was also calculated following the same procedure as the one used in the last section, yielding $V_{0,2} - V_{0,1} = (4.34 \pm 0.00)$ V, $\delta_v = (4.71 \pm 0.99)$ mV and, therefore, a finesse of 922 ± 193 .

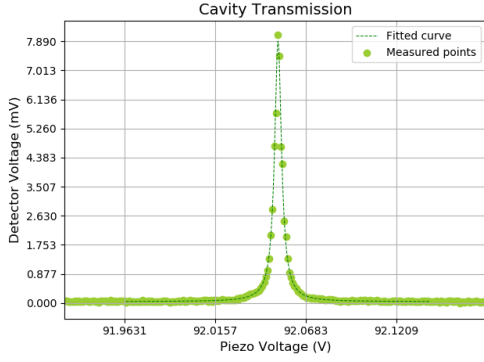
Substituting the measured transmission and finesse into Equations 3-10 and 3-9, respectively, we can write down:

$$(0.198 \pm 0.021) \times 10^{-3} = \frac{(1 - s^2 - R_m)^2}{(1 - R_m)^2} \quad (4-18a)$$

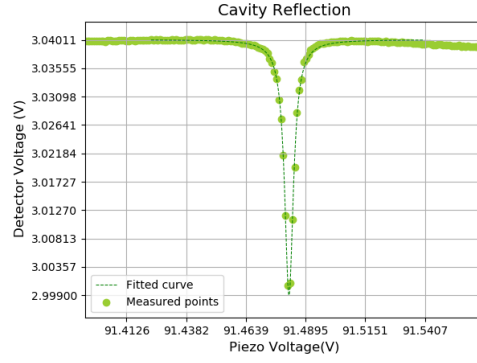
$$922 \pm 193 = \frac{\pi \sqrt{R_m}}{1 - R_m} \quad (4-18b)$$

Solving these equations for R_m and s^2 yields $R_m = 0.9965 \pm 0.0007$ and $s^2 = 0.0032 \pm 0.0007$. We can now substitute $R_{m2} = 0.9965 \pm 0.0007$ into Equation 4-13b and calculate R_{m1} . This yields $R_{m1} = 0.9981 \pm 0.0009$. Now, we can substitute the values of R_{m1} , R_{m2} and s_2^2 into Equation 4-13a and solve for s_1^2 , which leads to $s_1^2 = 0.0019 \pm 0.0009$.

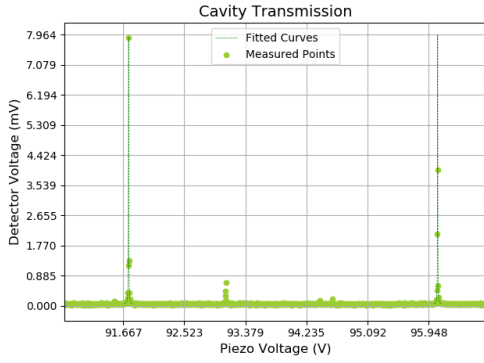
As it can be seen in Figure 4.9(c), there were two secondary peaks that couldn't be suppressed. To confirm that this didn't have any influence over the cavity's finesse, we increased the misalignment, leading to Figure 4.9(d), where the first peak is a secondary peak, and the right peak is the main peak. The finesse was then calculated using the same method described in the last paragraph, yielding 904 ± 173 , confirming that the presence of secondary peaks doesn't affect the finesse. This is consistent with the fact the finesse measures the losses in the cavity, and should depend solely on the mirror's reflection and loss coefficients.



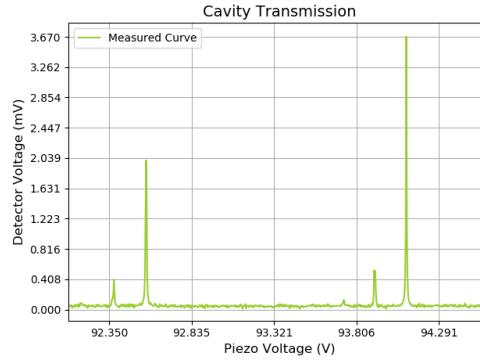
4.8(a):



4.8(b):



4.8(c):



4.8(d):

Figure 4.8: Transmission and reflection spectra for the concave-concave cavity. (a) Concave-concave cavity's single transmission peak. (b) Concave-concave cavity's single reflection valley. (c) Concave-concave cavity's consecutive transmission peaks. (d) Transmission peaks corresponding to the resonance of the fundamental mode and a higher order mode in the concave-concave cavity.

4.4 Confocal cavity

The last type of cavity we implemented was a concave-concave cavity in the confocal configuration. In the confocal configuration, the focus of both mirrors are coincident. Therefore, the cavity length must be equal to the radius of curvature. When this happens, the resonance frequencies are given by Equations 3-20 with $d_{cc} = R$:

$$\frac{\nu_{cc,jmn}}{\nu_{FSR}} = j + \frac{1}{2}(1 + m + n) = \frac{2j + k}{2} \quad (4-19a)$$

$$\frac{\nu_{cc,jlp}}{\nu_{FSR}} = j + \frac{1}{2}(1 + 2p + l) = \frac{2j + k}{2} \quad (4-19b)$$

where k is an integer.

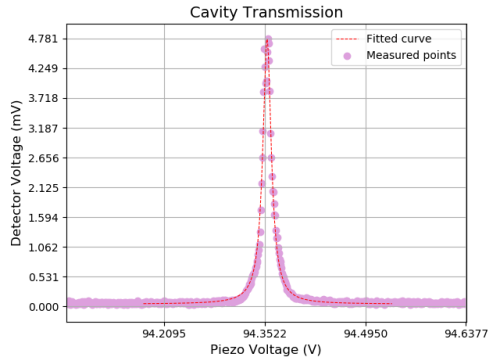
Equations 4-19 implies that the resonance frequencies are degenerate. A $m = 1, n = 0$ Hermite-Gauss mode ($k=2$) with $j = j_{HG}$ will have the same resonance frequency as a fundamental Gaussian mode with $j = j_{HG} + 1$. Therefore, if the beam is not properly aligned and/or modematched to the cavity, the main peak and secondary peaks will be superposed in the transmission spectrum. The frequency difference between two peaks then becomes:

$$v_{FSR,confocal} = v_{FSR} \left(\frac{2j+k}{2} - \frac{2j+k-1}{2} \right) = \frac{v_{FSR}}{2} \quad (4-20)$$

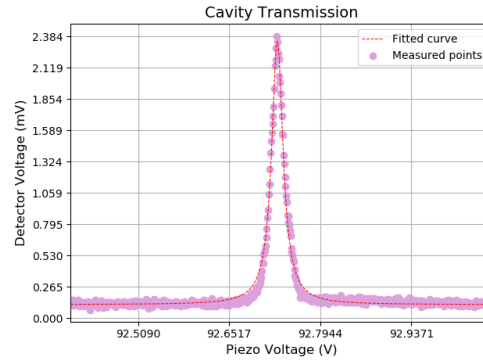
Therefore, the finesse, as defined by the ratio between the free spectral range and the full width at half maximum, is reduced by, at least, a factor of 2. In reality, the finesse is further reduced due to the fact that small deviations from the condition $d_{confocal} = R$ will cause the mode superposition to be defective, increasing the full width at half maximum of the transmission peak.

For our cavity, the lens used to collimate the beam has a focal distance f_1 of 11.00 mm (Thorlabs C220TME-B), while the modematching lens has a focal distance of $f_2=300$ mm. Differently from the situation we had for the plano-concave and the concave-concave cavities, when there were no restrictions for the cavity length, in the confocal configuration we wanted to have a cavity length L of 5.00 cm. Therefore, the position of the collimating lens with respect to the fiber output was set so that the beam waist after the modematching lens was the waist necessary for having a cavity with a length of approximately 5.00 cm. The waist of the beam was measured to be $\omega_0 = 61.0 \mu\text{m}$, and its location was found to be $z_0 = 11.91$ cm. From the concave-concave cavity modematching calculations, the position of the mirrors were calculated to be $z_{m1} = 8.67$ cm and $z_{m2} = 13.54$ cm. The second mirror was placed at $z_{m2} = 13.67$ cm to satisfy the confocal condition.

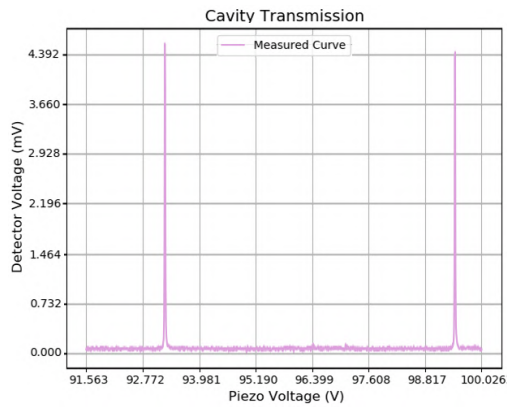
The cavity was then aligned following the procedure described in the first section of this chapter. Figure 4.9(a) shows a transmission peak and 4.9(c) shows two consecutive peaks when the cavity is aligned. For Figure 4.9(a), the fitted values are $\delta = 14.5$ mV, $V_0 = 94.4$ V, $C_0 = 0.044$ mV and $A = 4.72$ mV, while for Figure 4.9(c), the distance between the two peaks is 6.27 V. The finesse was measured to be 381.4 ± 48.2 . The larger peak width is due to the presence of higher order modes that resonate almost at the same frequency as the fundamental mode, as it can be seen in Figure 4.11(a), which shows the transmitted light during the resonance peak.



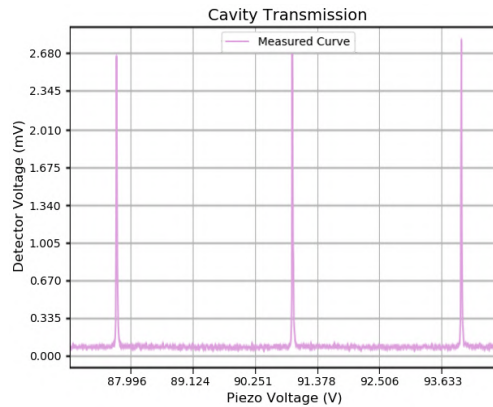
4.9(a):



4.9(b):



4.9(c):



4.9(d):

Figure 4.9: Transmission peaks for: (a) and (c) aligned confocal cavity; (b) and (d) misaligned confocal cavity.

The cavity was then misaligned by translating the beam horizontally. By doing this, an extra peak appeared between the two initial peaks, as shown in Figure 4.9(d), in which the distance between two consecutive peaks is 3.14 V. In order to guarantee the confocal condition, the transmission peak shape can be used. When the cavity's length is too large or too small, the transmission peak becomes asymmetric. Therefore, we translated the second cavity mirror until the transmission peak became symmetric. Figure 4.10 shows the transmission peak when the cavity is too short, too long and with the right length.

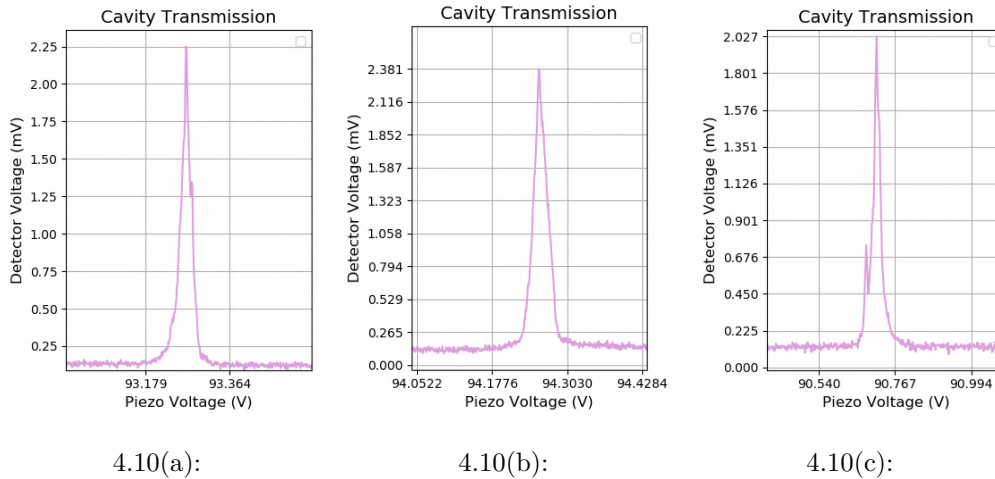


Figure 4.10: Comparison between the shape of transmission peaks when the cavity's length is varied. Confocal cavity's transmission peak when the cavity's length: (a) is greater than $2R$; (b) is equal to $2R$; (c) is less than $2R$.

By fitting a symmetric transmission peak, as the one shown in Figure 4.9(b), we found: $\delta V = 23.3$ mV, $V_0 = 94.3$ V, $C_0 = 0.114$ mV and $A = 2.19$ mV. The finesse was measured to be 138.2 ± 9.8 . This reduction in finesse was caused by the fact that the free spectral range was reduced to half of its original value, and by the superposition of many modes at each resonance peak, which caused the peaks to become larger. Figures 4.11(b) and 4.11(c) show the transmitted intensity pattern for two consecutive resonance peaks. As it can be seen, each of them is a different superposition of multiple modes.

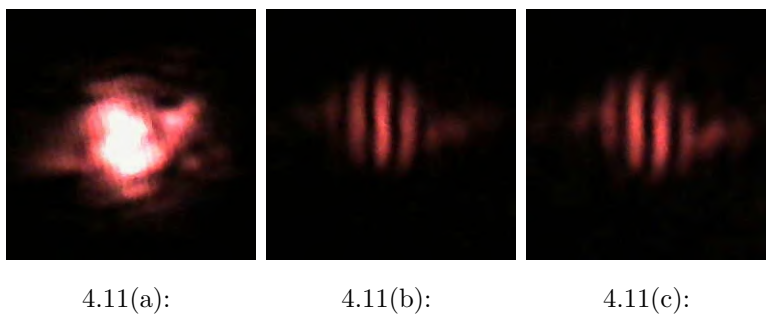


Figure 4.11: Confocal cavity's transmission pattern under different situations. (a) Transmission pattern when the cavity is aligned. (b) First type of transmission pattern when the cavity is misaligned. (c) Second type of transmission pattern when the cavity is misaligned.

At this point, it is useful to explain one of the reasons why we performed modematching between the beam and our confocal cavity. Usually, a collimated

beam can be used. By doing so, higher order Laguerre-Gauss modes would be excited [36], and, since they would be degenerated in the confocal configuration, a pattern of concentric rings would be observed at the output of the cavity when proper alignment was achieved [40]. In our setup this would not be possible, since using a collimated beam means larger diffraction loss due to beam divergence inside the cavity, and the cavity transmission, which is already small for our high reflectance mirrors, would become negligible. Therefore, we chose to modematch the beam, in order to reduce diffraction losses, and to demonstrate the degeneracy by misaligning the beam and exciting higher order Hermite-Gauss modes.

4.4.1 Discussions

The first important byproduct of this part of our experimental work was the knowledge on how to implement Fabry-Pérot cavities. We have successfully implemented the plano-concave cavity, the concave-concave cavity and the confocal cavity. Each of these cavities can be used in different setups that may be in the interest of our laboratory. The plano-concave cavity, for example, will be useful if a cavity with a membrane acting as a moveable mirror [31], as in Figure 4.12(a), or with a membrane attached to a plane mirror, as in Figure 4.12(b), is to be implemented. The concave-concave cavity will be useful if a *membrane in the middle* configuration, shown in Figure 4.12(c), is necessary in an experiment [27].

The second important byproduct regards the characterization of the equipment used in the implementation of our Fabry-Pérot cavity. Although functional, our setup had some drawbacks. The first of them, were the high mirror losses. Although our mirror's reflection was significantly high, as evidenced by the finesse of approximately 10^3 , the magnitude of the transmission peaks and reflection peaks were significantly reduced by the presence of losses other than the transmission through the mirror. In future experiments it might be necessary to achieve a finesse on the order of 10^4 , and, therefore, it will be even more important that the mirrors have not only high reflectance, but also that they transmit most of the light that is not reflected.

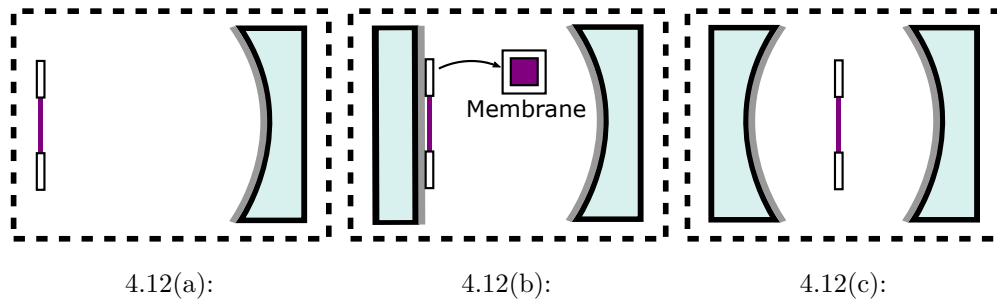


Figure 4.12: Possible configurations integrating a membrane to a Fabry-Pérot cavity: (a) Membrane acting as one of the cavity's mirrors; (b) Plano-concave analogous of the *membrane in the middle* configuration; (c) Membrane positioned in the middle of a cavity (*Membrane in the middle* configuration).

Improvements can also be made on the structure used to hold the cavity mirrors. The threaded mounts allowed for easier cavity alignment, but reduced the cavity stability, as evidenced by the large variance in the measured full width at half maximum of the transmission peaks. Therefore, it became evident that using a proper cavity etalon will be essential to achieve high cavity stability.

Finally, we conclude that the confocal cavity doesn't suit our needs for high finesse, due to the degeneracy of the modes and the consequent lowering in finesse. In the next chapter, we explore the theoretical background for the second part of our experimental work, which will be presented in Chapter 6.

5 Optical Tweezers

Optical tweezers are important tools currently employed not only in physics experiments, where they can be used to measure small forces [28, 29, 41, 42], but also in other branches of science, such as biology, where it can be used to manipulate living microorganisms [43–46].

The working principle of an optical tweezer is the transfer of momentum between a laser beam and a particle. When the laser beam is tightly focused, this transfer of momentum results in a force that pushes the particle towards the focal region, creating what is also called an optical trap. Figure 5.1 shows a simplified schematic of an optical tweezer: a laser beam is focused by an objective lens, resulting in the trapping of a dielectric sphere around the origin.

There are different ways to understand how a focused laser beam can generate an optical trap. In this chapter, we present three regimes under which optical trapping can happen, and calculate how parameters like the NA of the objective lens, the wavelength of the beam and the particle's size can affect the behaviour of an optical tweezer.

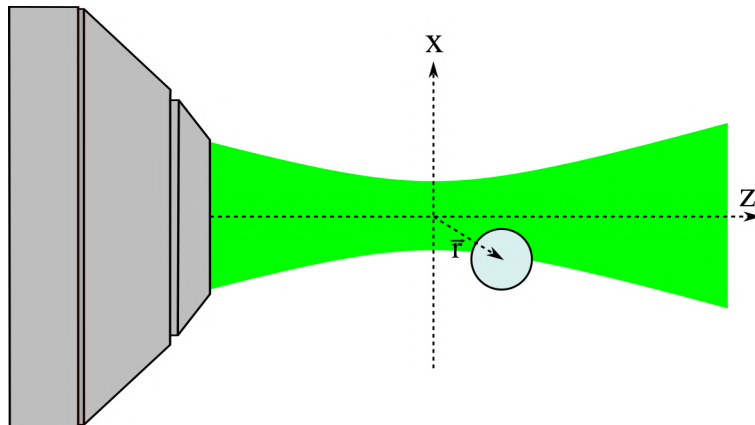


Figure 5.1: Schematic of an optical tweezer, showing an objective lens focusing a laser beam, causing a sphere to be trapped at the focal region.

5.1 Geometrical Optics Approximation

The easiest way to have an idea on how an optical tweezer works is to use the geometrical optics approach, which is valid when the wavelength is small

in comparison with the particle's size (in the case of a sphere, $R \gtrsim 10\lambda$, where R is the sphere's radius and λ is the wavelength) [47].

Consider a dielectric sphere, having a refractive index larger than that of the medium in which it is in, located exactly at the focus of a light beam, as shown in Figure 5.2(a), where only the beam's outer rays are displayed. In this situation, the rays are perpendicular to the sphere's surface and are not refracted.

Consider, now, that the particle moves slightly to the right, as shown in Figure 5.2(b). In this case, the light rays get refracted when they enter the sphere and then again when they exit it. As a result, if the sphere's refractive index is greater than that of the medium, the rays are deviated to the right. Since light carries momentum, that means that the rays must have transferred momentum in the opposite direction, causing a force that pushes the sphere back to the beam focus.

Similarly, if the sphere is slightly moved down, the light rays will get refracted and deviated as depicted in Figure 5.2(c), resulting, again, in a force that will push the sphere back to the focus. Therefore, at least for small displacements, the sphere is said to be "trapped": the force exerted by the light always tends to push the sphere back to the focal point.

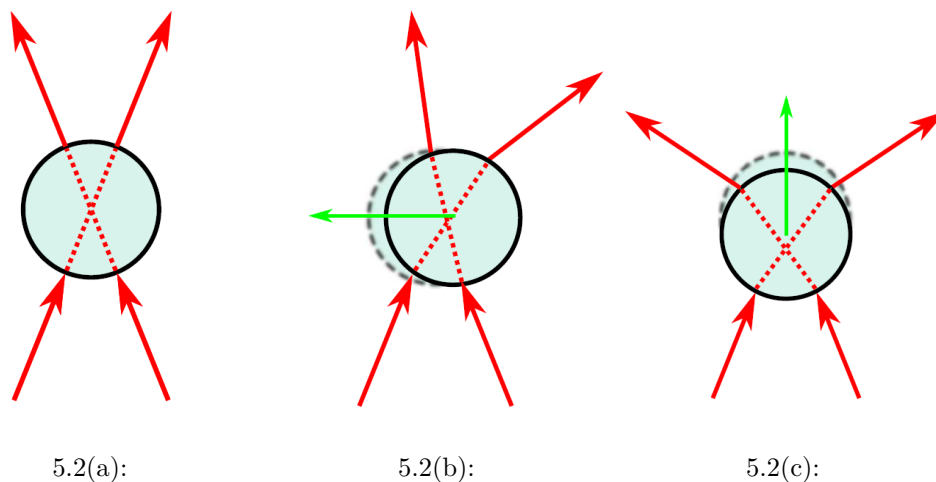


Figure 5.2: Refraction of light rays (red arrows) by a sphere under the geometrical optics approximation and the forces generated by it (green arrows) when: (a) the sphere is at the focus; (b) the sphere laterally displaced; (c) the sphere is vertically displaced. The green arrows indicate the force acting on the sphere.

In order to calculate the force acting on the sphere, not only refraction should be taken into account, but also reflection. When the beam hits the

sphere, part of it is reflected and, by the same argument of momentum exchange, the sphere is pushed in the direction of the propagation of the beam. Moreover, when a ray inside the sphere hits the sphere surface, it is both refracted and reflected back to the sphere interior. This process of multiple reflection and refraction is illustrated in Figure 5.3 for a single light ray.

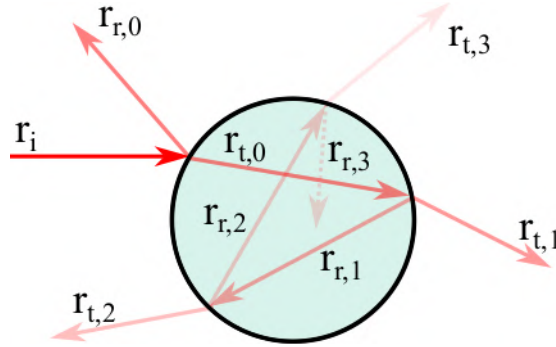


Figure 5.3: Multiple reflections and refractions of a light ray that hits a sphere.

We can calculate the force due to a single ray by considering the difference between its momentum before hitting the sphere and the total momentum of the reflected and transmitted rays. If the ray power is P_i and the medium refractive index is n_m , this force will be [34]:

$$\vec{F} = \frac{n_m P_i}{c} \hat{r}_i - \frac{n_m P_{r,0}}{c} \hat{r}_{r,0} - \sum_{n=1}^{\infty} \frac{n_m P_{t,n}}{c} \hat{r}_{t,n} \quad (5-1)$$

and the total force will be the sum of the forces caused by each individual ray.

Because the light intensity gets smaller after each refraction or reflection, most of the contributions to \vec{F} will come from the rays $r_{r,0}$ and $r_{t,1}$. If the sphere's center is positioned at the beam's central axis, the first reflection of the light rays will cause a scattering force in the direction of the beam's propagation. If this force is larger than the restoring force caused by the rays $r_{t,1}$, trapping won't be possible, and the sphere will be pushed away from the focal point. The fact that a larger refractive index difference between the medium and the sphere increases reflection is one of the reasons why it is harder to trap a sphere in air than in water.

A special situation happens when the sphere's refractive index is smaller than the medium's refractive index. In this case, the conclusions we draw from Figure 5.2 are not valid: the rays will be deviated in the opposite direction. This will cause the sphere to be pushed away from the focus both by the refraction and the reflection processes. This was first observed by Ashkin [8] through the use of air bubbles ($n \approx 1$) in a Glycerol ($n \approx 1.47$) sample.

5.2

Dipole Approximation

5.2.1

Forces on an electric dipole

In the last section we gave an overview on how one can calculate the forces that arise when a beam is focused on a sphere much larger than the beam's wavelength ($R \gtrsim 10\lambda$). Now, we move our focus to the approximate treatment one can use in order to calculate these forces when the sphere is much smaller than the beam's wavelength ($R \lesssim \lambda/10$) [47].

In this regime, the electric field inside the sphere, at any given instant of time, is approximately uniform. If the sphere is dielectric, this constant electric field induces an electric dipole. Because the light electromagnetic field oscillates as time evolves, the induced dipole will also oscillate, emitting electromagnetic radiation. The problem, then, is one of electromagnetic scattering. Here, we use the results given by [34] for this problem's solution.

In the following discussion, the subscripts md , sp and 0 refer to the quantities as measured in the propagation medium, the particle interior and the vacuum, respectively. The force acting on a dielectric particle is given by:

$$\vec{F}_d = \frac{1}{4} \Re \alpha_d \nabla |E_i|^2 + \frac{\sigma_{ext,d}}{2c_{md}} \Re(\vec{E}_i \times \vec{H}_i^*) - \frac{i\epsilon_{md}c_{md}}{4\omega} \sigma_{ext,d} \nabla \times (\vec{E}_i \times \vec{E}_i^*) \quad (5-2)$$

where α_d is the effective polarizability of the dielectric particle and $\sigma_{ext,d}$ is the extinction cross-section for this scattering process, which is given by:

$$\sigma_{ext,d} = \frac{k_0}{\epsilon_0} \Im \alpha_d \quad (5-3)$$

For a dielectric sphere, the effective polarizability is given approximately by:

$$\alpha_d \approx 3V \epsilon_{md} \frac{\epsilon_r - 1}{\epsilon_r + 2} \left[1 + i \frac{Vk_{md}^3}{2\pi} \left(\frac{\epsilon_r - 1}{\epsilon_r + 2} \right) \right] \quad (5-4)$$

where $\epsilon_r = \epsilon_{sp}/\epsilon_{md}$ and V is the sphere's volume.

Each of the three terms in Equation 5-2 can be analyzed separately. The first term is called the gradient force, and can be rewritten, using Equation 5-4 and the definition refractive index, $n_i = c/c_i$, as:

$$\vec{F}_{d,grad}(\vec{r}) = \frac{2\pi n_{md} R^3}{c} \left(\frac{m^2 - 1}{m^2 + 2} \right) \nabla I_i(\vec{r}) \quad (5-5)$$

where $m = n_{sp}/n_{md}$ is the relative refractive index between the sphere and the medium, I_i is the electromagnetic intensity and \vec{r} is the sphere's center position. For $m > 1$, the gradient force pushed the particle to the region of

highest intensity, while for $m < 1$, it pushes the particle out of that region, reproducing the behaviour found in the geometric optics regime.

The gradient force is a conservative force derived from the trapping potential:

$$V_d(\vec{r}) = -\frac{2\pi n_{md} R^3}{c} \left(\frac{m^2 - 1}{m^2 + 2} \right) I_i(\vec{r}) \quad (5-6)$$

In order to have a stable optical trap, the potential well must be much larger than the average kinetic energy of the trapped particle. This is because the thermal agitation of the molecules that constitute the medium causes the sphere to have a probability of having instant kinetic energy much larger than the average kinetic energy. According to statistical mechanics theory, the average kinetic energy of the sphere is $3k_B T/2$. Therefore, we require $|V_{min}| \geq 10 \times 3k_B T/2 = 15k_B T$ [47].

The second term is called the scattering force. It is a non-conservative force that occurs due to momentum transfer from the field to the sphere caused by scattering and absorption processes. For a wave travelling in the z direction, the scattering force can be rewritten, using Equation 5-4, the definition of refractive index and Equation 5-3 for the cross section, as:

$$\vec{F}_{d,scat}(\vec{r}) = \frac{128\pi^5 R^6}{3c\lambda_0^4} \left(\frac{m^2 - 1}{m^2 + 2} \right)^2 n_{md}^5 I_i(\vec{r}) \hat{z} \quad (5-7)$$

The scattering force doesn't reverse its direction when $m < 1$: it always points in the wave's propagation direction. Again, trapping will only be possible if the restoring gradient force is sufficient to counterbalance the scattering force.

Finally, the third term is called the spin-curl force. It is a result of polarization gradients in the electromagnetic field. It is usually small when compared to the other two force terms [48]. Also, since we'll only use laser beams with uniform polarization in this work, we won't need to get into more details about the spin-curl force.

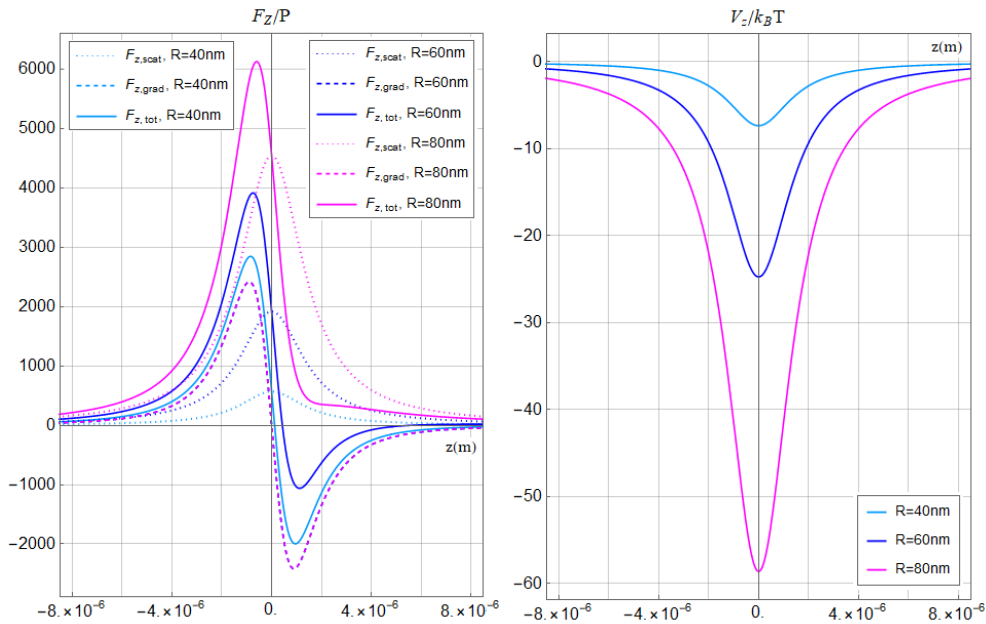
Equations 5-5, 5-6 and 5-7 are valid for any beam propagating in the z direction and could be adapted to other particle shapes by recalculating the effective polarizability. In this work we are especially interested in the forces arising from focusing a Gaussian beam in a dielectric sphere. In order to calculate these forces, all we have to do is substitute Equations 2-13a and 2-14 in the equations for the gradient force, the scattering force and the trapping potential.

5.2.2

Numerical simulations for the dipole approximation

In order to understand how the forces and the potential depend on the parameters n_{md} , n_{sp} , NA (which is directly related to ω_0), λ_0 and R , it is useful to plot those quantities as a function of the particle displacement. We consider a Gaussian beam propagating in the $+z$ direction with the waist located at the $z = 0$ plane and define: $F_{z,scat}(z) = F_{d,scat}(0, 0, z)$, $F_{z,grad}(z) = F_{d,grad}(0, 0, z)$, $F_{z,tot}(z) = F_{z,grad}(z) + F_{scat,z}$, $F_{x,grad}(x) = F_{d,grad}(x, 0, 0)$, $V_d(z) = V_d(0, 0, z)$ and $V_x(x) = V_d(x, 0, 0)$.

Figure 5.4(a) shows the forces in the z direction divided by the particle's weight for a Silica sphere trapped in water by a 20 mW laser beam at 780 nm. The numerical aperture is 0.4. As it can be seen, the gradient force is always opposite to the particle displacement. Since we divided it by the particle's weight, and it scales with R^3 , the curve is the same for the 3 particle sizes. The scattering force, on the other hand, scales with R^6 and is always positive. As a result, for sufficiently large R , the total force is always positive, meaning trapping is not possible, as it occurs for the 80 nm particle in Figure 5.4(a). Since an equilibrium position must exist, we require that $F_z(z) = 0$ to have a real solution in order for trapping to be possible, which sets an upper limit for the sphere's radius.



5.4(a):

5.4(b):

Figure 5.4: Dipole approximation: (a) force in the z direction; (b) potential in the z direction.

In order to estimate how the different parameters will affect the presence of an equilibrium position, it is useful to look at the ratio $(F_{scat,z})_{max}/(F_{grad,z})_{max}$. This ratio indicates how dominant the scattering force is. It is given by:

$$\frac{512\pi^3 n_{md}^3 R^3}{9\sqrt{3}\lambda_0^3 NA^2} \left(\frac{m^2 - 1}{m^2 + 2} \right) \quad (5-8)$$

Figure 5.4(b) shows the trapping potential as a function of the displacement in the z direction when $x = y = 0$. As it can be seen, the smaller the particle, the smaller the well. Because we require $|V_{min}| > 15k_B T$, this sets a lower limit for the sphere's radius. Therefore, we conclude that, in this example, only the sphere with radius $R = 60$ nm would be stably trapped. Mathematically, this lower bound can be calculated from:

$$|V_{min}| = \frac{4\pi^2 NA^2 n_{md}^3 R^3 P}{c\lambda_0^2} \left(\frac{m^2 - 1}{m^2 + 2} \right) \quad (5-9)$$

which is valid for a Gaussian beam.

Figure 5.5(a) shows the force in the x direction as a function of the particle displacement for the same parameter values as used before. Again, since we are dividing the force by the sphere's weight, the three curves are overlapped. As expected, the magnitude of the force is symmetric with respect to the z axis and always points to the position $x = 0$. Figure 5.5(b) shows the trapping potential as a function of the displacement in the x direction.

One important feature of the gradient force is that it has a linear range both in the z direction and in the radial direction. Therefore, for small displacements, the trapping potential can be approximated by a harmonic potential, and a spring constant can be calculated for the z and radial directions. Neglecting the scattering force, the spring constants are given, for a Gaussian beam trap, by:

$$\kappa_z = \frac{8\pi^4 NA^6 n_{md}^5 R^3 P}{\lambda_0^4} \left(\frac{m^2 - 1}{m^2 + 2} \right) \quad (5-10a)$$

$$\kappa_x = \kappa_y = \frac{16\pi^4 NA^4 n_{md}^5 R^3 P}{\lambda_0^4} \left(\frac{m^2 - 1}{m^2 + 2} \right) \quad (5-10b)$$

Since $NA \leq 1.3$ for most objective lenses used in optical tweezers, the trapping is generally stronger in the radial direction than in the z direction.

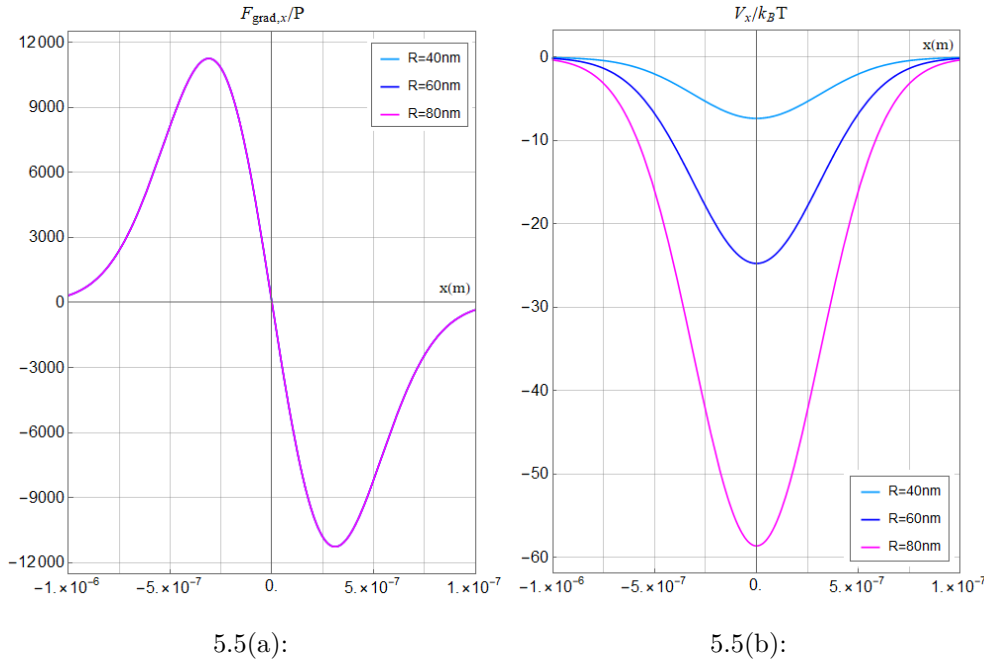


Figure 5.5: Dipole approximation: (a) force in the x direction; (b) potential in the x direction.

5.3 The intermediate regime

5.3.1 Generalized Mie theory

When the particle's radius is neither much smaller nor much larger than the wavelength, both the previous approximations break down. In this case, the forces acting on the particle must be calculated using Mie scattering theory. The full calculation is beyond the scope of this work and can be found in detail in references such as [34]. Here, we will only outline such calculations and use the toolbox provided by [49] to analyze the results when typical parameters are used.

The force on the trapped particle arises from the transfer of momentum from the electromagnetic field to the particle. Therefore, if we decompose the electromagnetic field in incoming waves that propagate towards the center of mass of the particle and outgoing waves that propagate out of the center of mass of the particle, the momentum transferred to the sphere can be found by calculating the momentum variation between the outgoing waves and the incoming waves. If we define the particle's center as the origin of the

coordinate system, this expansion can be made in terms of vector spherical wavefunctions [49]:

$$\vec{E}_{out} = \sum_{n=1}^{\infty} \sum_{m=-n}^n a_{nm}^{out} \vec{M}_{nm}^{(1)}(k\vec{r}) + b_{nm}^{out} \vec{N}_{nm}^{(1)}(k\vec{r}) \quad (5-11a)$$

$$\vec{E}_{in} = \sum_{n=1}^{\infty} \sum_{m=-n}^n a_{nm}^{in} \vec{M}_{nm}^{(2)}(k\vec{r}) + b_{nm}^{in} \vec{N}_{nm}^{(2)}(k\vec{r}) \quad (5-11b)$$

where the vector spherical wavefunctions are given by:

$$\vec{M}_{nm}^{(1,2)}(k\vec{r}) = N_n h_n^{(1,2)}(kr) \vec{C}_{nm}(\hat{r}) \quad (5-12a)$$

$$\vec{N}_{nm}^{(1,2)}(k\vec{r}) = \frac{h_n^{(1,2)}(kr)}{kr N_n} \vec{P}_{nm}(\hat{r}) + N_n \left(h_{n-1}^{(1,2)}(kr) - \frac{nh_m^{(1,2)}(kr)}{kr} \right) \vec{B}_{nm}(\hat{r}) \quad (5-12b)$$

where $N_n = [n(n+1)]^{-1/2}$, $h_n^{(1,2)}(kr)$ are the spherical Hankel functions of the first and second kinds and $\vec{C}_{nm}(\hat{r})$, $\vec{P}_{nm}(\hat{r})$ and $\vec{B}_{nm}(\hat{r})$ are the vector spherical harmonics, an orthonormal basis for vector fields in spherical coordinates that generalizes the more commonly encountered spherical harmonics [35].

Once the coefficients a_{nm}^{in} , b_{nm}^{in} , a_{nm}^{out} and a_{nm}^{out} have been calculated, either analytically, for the case of a sphere, or numerically, for the case of a non spherical particle, they can be used to determine the force in the axial direction, which is given by:

$$\begin{aligned} F_z = & \frac{2n_{md}P}{c} \left(\sum_{n=1}^{\infty} \sum_{m=-n}^n |a_{nm}^{in}|^2 + |b_{nm}^{in}| \right)^{-1} \\ & \times \sum_{n=1}^{\infty} \sum_{m=-n}^n \frac{m}{n(n+1)} \Re(a_{nm}^{in*} b_{nm}^{in} - a_{nm}^{out*} b_{nm}^{out}) - \\ & - \frac{1}{n+1} \left[\frac{n(n+2)(n-m+1)(n+m+1)}{(2n+1)(2n+3)} \right] \\ & \times \Re(a_{nm}^{in} a_{n+1,m}^{in*} + b_{nm}^{in} b_{n+1,m}^{in*} - a_{nm}^{out} a_{n+1,m}^{out*} - b_{nm}^{out} b_{n+1,m}^{out*}) \end{aligned} \quad (5-13)$$

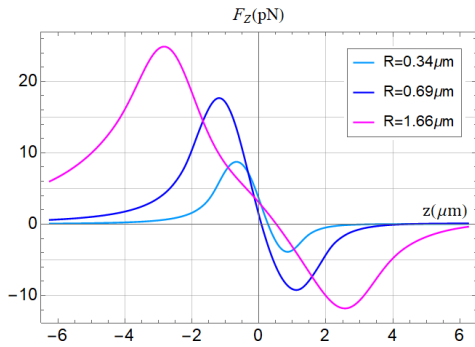
5.3.2

Numerical simulations for the intermediate regime

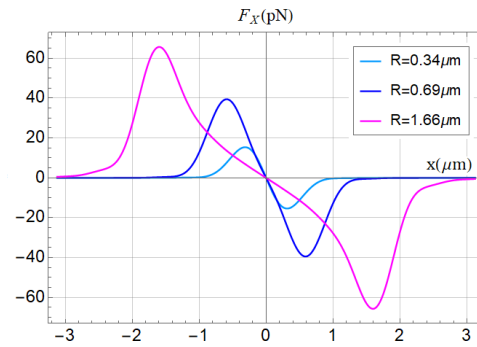
Figure 5.6(a) and 5.6(b) shows the forces in the z and x directions, respectively, for three different Silica spheres trapped in water. The laser power is 50 mw, the numerical aperture is 0.95 and the wavelength is 780nm. As it can be seen, the equilibrium position in the z direction exists for the three particle sizes chosen for the simulation, but it is different for each size. The force in the x direction is antisymmetric, as expected from the radial symmetry of the situation. Just like in the dipole approximation, both forces have a linear

range around the equilibrium position and, therefore, a spring constant can be attributed to each direction.

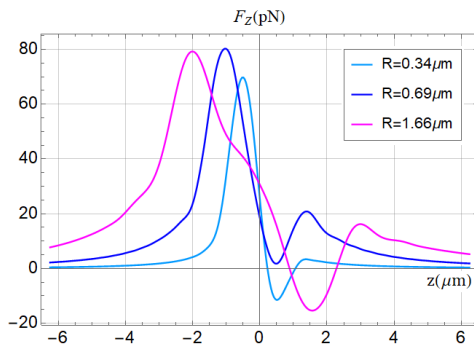
Figure 5.6(c) and 5.6(d) shows the forces in the z and x directions, respectively, for three different Silica spheres trapped in air. The laser parameters are the same as the ones used in the water trap simulations. In the case of air trapping, a new situation arises: an equilibrium position exists for $R = 0.34 \mu\text{m}$ and $R = 1.66 \mu\text{m}$, but not for $R = 0.69 \mu\text{m}$. Differently from what happened in the dipole approximation, there isn't an upper limit for the particle radius above which trapping is not possible and below which trapping is possible.



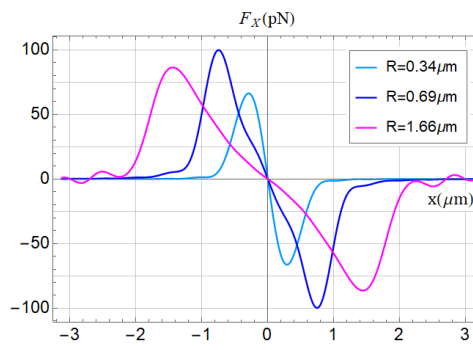
5.6(a):



5.6(b):



5.6(c):



5.6(d):

Figure 5.6: Forces in the z and x direction under the intermediate regime for a particle trapped in: (a) and (b) water; (c) and (d) air. Aside from the medium's refractive index, all other parameters are the same.

A necessary condition for trapping to be possible is that the force in the z direction is null for some z . We can evaluate if that is the case by looking at the minimum value of this force: if the minimum value is positive, no equilibrium position will exist. Figure 5.7(a) shows the minimum force in the z direction for a sphere trapped in air by a 780 nm, 50 mW laser as a function of the particle's radius for three different numerical apertures. As it can be seen, for $\text{NA} = 0.7$, the minimum force is positive for almost all values of R . As the numerical aperture

increases, the minimum force decreases, and trapping becomes possible for more values of R . Figure 5.7(b) shows the minimum force for spheres made of two different materials trapped in water by a 780 nm, 50 mW laser when a 0.7 numerical aperture is used. As it can be seen, there are several values of R for which trapping is not possible in the case of Polystyrene spheres, while in the case of Silica spheres, the minimum force is always negative.

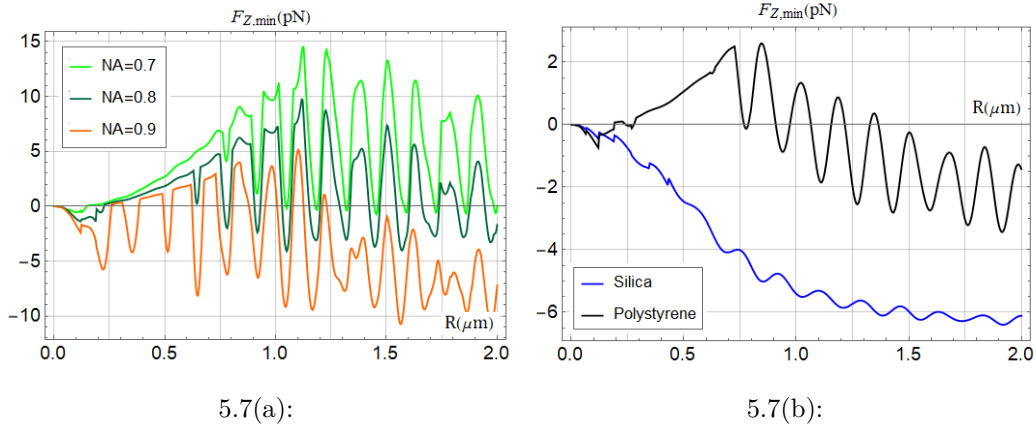


Figure 5.7: Minimum force in the z direction as a function of the sphere's radius for : (a) spheres trapped in air by beams having different numerical apertures; (b) spheres made of different materials trapped in water.

5.4 Trapped Particle Motion

5.4.1 Equations of motion for a trapped particle

So far, we have been concerned only with analysing the existence of an equilibrium position given the trapping parameters. But even when an equilibrium position exists, a trapped particle undergoes a constant motion due to the collisions with the molecules of the medium in which they are immersed. This motion can be described by considering the three forces that act on the particle.

The first of them is the force exerted by the trapping laser. As we've already said, for small displacements from the equilibrium position, the trap acts as a harmonic potential and, therefore, the force on the particle is proportional to its displacement. In three dimensions, this takes the form of a force $\vec{F}_{harmonic} = -\kappa_x x \hat{x} - \kappa_y y \hat{y} - \kappa_z z \hat{z}$, where κ_{xi} are the spring constants of the trap.

The second of them is a drag force exerted by the fluid in which the particle is immersed. This force always opposes the motion and its magnitude is, approximately, proportional to the particle velocity. Therefore, it takes the form of a force $\vec{F}_{drag}(t) = -\gamma\vec{v}(t)$. The γ coefficient is the drag coefficient, and depends on the particle size and on the fluid viscosity, which, in turn, depends on the temperature. For a spherical particle it can be determined by Stoke's law:

$$\gamma(T) = 6\pi\eta(T)a \quad (5-14)$$

where T is the fluid's temperature, $\eta(T)$ is the fluid's viscosity at temperature T and a is the particle's radius.

Finally, we have a random force caused by the collisions between the fluid's molecules and the trapped particle. This force is responsible for the Brownian motion and takes the form of $\vec{\beta}(t) = \gamma\sqrt{2D}(W_x(t)\hat{x} + W_y(t)\hat{y} + W_z(t)\hat{z})$, where D is the diffusion coefficient and $W_x(t)$, $W_y(t)$ and $W_z(t)$ are independent white noises [34]. The diffusion coefficient is given by:

$$D = \frac{k_B T}{\gamma} \quad (5-15)$$

where k_B is the Boltzmann coefficient, and the white noise has the following properties:

- $\langle W(t) \rangle = 0$ for each t , where the brackets denote an average over ensembles;
- $\langle W(t)W(t') \rangle = \delta(t - t')$ for each t and t' ;

Therefore, the equations of motion for a trapped particle is:

$$m\ddot{x}_i(t) = -\kappa_{x_i}x_i(t) - \gamma\dot{x}_i(t) + \beta_{x_i}(t) \quad (5-16)$$

where $x_i = x, y, z$.

The velocity of a particle moving in a fluid decreases exponentially, with a characteristic time m/γ . If this characteristic time is sufficiently small, the particle will rapidly lose its kinetic energy, and the particle's inertia becomes negligible [50]. For the case of a trapped sphere, this ratio is proportional to a^2 . Therefore, for sufficiently small spheres, the inertial term can be dropped. For a sphere with a radius of $1\ \mu\text{m}$ trapped in water, for example, $m/\gamma \approx 10^{-10}\text{s}$, which, as we'll see, is much smaller than the time scales in which we are interested. The equations of motion, then, become:

$$0 = -\kappa_{x_i}x_i(t) - \gamma\dot{x}_i(t) + \sqrt{2\gamma k_B T}W_{x_i}(t) \quad (5-17)$$

It is also useful to consider this equation in Fourier space:

$$\sqrt{2\gamma k_B T} \tilde{W}_{x_i}(\omega) = k_{x_i} \tilde{X}_i(\omega) + i\gamma\omega \tilde{X}_i(\omega) \quad (5-18)$$

where the fourier transforms $\tilde{X}(\omega)$ and $\tilde{W}(\omega)$ are to be calculated during a finite time interval:

$$\tilde{F}(\omega) = \int_{-T_m/2}^{T_m/2} e^{i\omega t} f(t) dt \quad (5-19)$$

where T_m is the measuring time and $\omega = 2\pi n/T_m$, with $n \in \mathbb{Z}$.

Figure 5.8(a) shows the first 100 positions of a trapped particle during a simulation, while 5.8(b) shows all of the 50×10^3 positions. The values used for this simulation were $\kappa_x = \kappa_y = 1 \text{ fN/nm}$, $a = 1 \mu\text{m}$, $T = 295 \text{ K}$, $\eta = 9.85 \times 10^{-4} \text{ sPa}$ and the time step was $4 \times 10^{-5} \text{ s}$, resulting in a total time of 2 s. In Figure 5.8(b) we can clearly observe the randomness of the resulting particle movement, and in Figure 5.8(b) we can see the confinement of the particle around the origin.

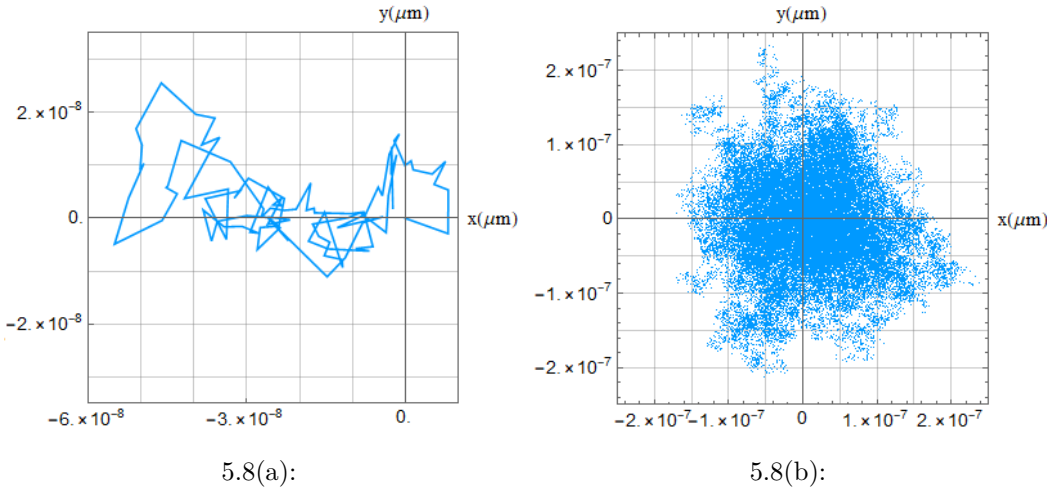


Figure 5.8: Brownian motion simulation considering the existence of a harmonic force around the origin: (a) the first hundred points of the simulation; (b) all of the fifty thousand points of the simulation

5.4.2

Autocorrelation analysis of the trapped motion

Due to the random behaviour of the particle position, the best way to analyse the movement of a trapped particle is using statistics. One of the quantities that might be used is the autocorrelation function (ACF) of the particle position in a given direction, which is given by:

$$C_{x_i}(\tau) = \langle x_i(t)x_i(t + \tau) \rangle \quad (5-20)$$

where the brackets refer to an ensemble average and $x_i = x, y, z$.

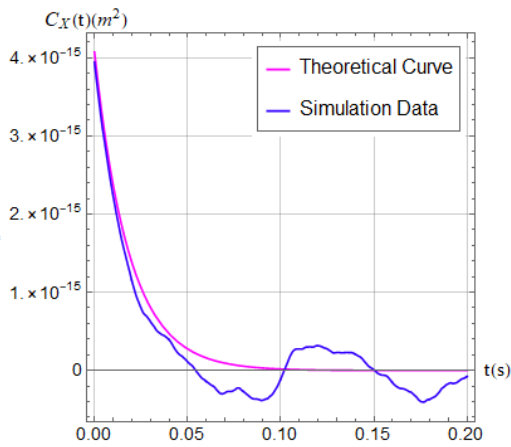
For a trapped particle, this quantity can be calculated from the equation of motion, yielding [34]:

$$C_{x_i}(\tau) = \frac{k_B T}{\kappa_{x_i}} e^{-\kappa\tau/\gamma} \quad (5-21)$$

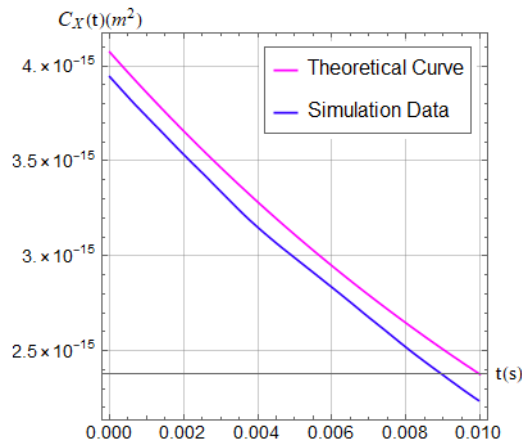
Therefore, the autocorrelation decreases exponentially with a characteristic time γ/κ_{x_i} (or, equivalently, characteristic frequency κ_{x_i}/γ). The larger the spring constant, the faster the autocorrelation approaches 0. For $\tau = 0$, Equations 5-20 and 5-21 tells us that $C_{x_i}(0) = \langle x_i(t)^2 \rangle = k_B T/\kappa_{x_i}$. This is the result we expect from the equipartition theorem, that asserts that the expected values for the kinetic and potential energies in each direction are equal:

$$\frac{m\langle \dot{x}_i^2 \rangle}{2} = \frac{\kappa_{x_i}\langle x_i^2 \rangle}{2} = \frac{k_B T}{2} \quad (5-22)$$

Figure 5.9(a) shows the theoretical autocorrelation function for the values used in the previous simulation, as well as the calculated autocorrelation function. The value of $C_x(\tau)$ was calculated by taking the average of $x(t)x(t+\tau)$ for each t , which approaches the average over ensembles indicated by Equation 5-20 for an ergodic system. By fitting the first 250 points, shown in Figure 5.9(b) to an exponential Ae^{-Bt} , we find $A = 3.95 \times 10^{-15} \text{m}^2$ and $B = 56.2 \text{Hz}$, while the theoretical values are $A = 4.07 \times 10^{-15} \text{m}^2$ and $B = 53.9 \text{Hz}$.



5.9(a):



5.9(b):

Figure 5.9: Comparison between the ACF calculated using the points from the previous simulation and the ACF predicted by the theory: (a) first 0.2 seconds; (b) first 0.01 seconds.

5.4.3 Power Spectral Density

Another quantity that might be used for analysing the trapped motion is the Power Spectral Density (PSD) of the particle's position. It is defined as:

$$P_{x_i}(\omega) = \frac{\langle \tilde{X}_i^*(\omega)\tilde{X}_i(\omega) \rangle}{T_m} \quad (5-23)$$

that is, the squared absolute value of the Fourier transform of $x(t)$ averaged over ensembles divided by the measuring time T_m .

Solving Equation 5-18 for $\tilde{X}_i(\omega)$ and substituting in Equation 5-23 we can write:

$$P_{x_i}(f) = \frac{D/(2\pi^2 T_m) \langle \tilde{W}_{x_i}^*(\omega)\tilde{W}_{x_i}(\omega) \rangle}{f_{c,x_i}^2 + f^2} \quad (5-24)$$

where D is the previously defined diffusion coefficient, and $f_{c,x_i} = \kappa_{x_i}/2\pi\gamma$ is called the corner frequency. From the white noise properties, it is easy to show that $\langle \tilde{W}_{x_i}^*(\omega)\tilde{W}_{x_i}(\omega) \rangle = T_m$. Therefore, the PSD for a trapped sphere is given by [51]:

$$P_{x_i}(f) = \frac{D/(2\pi^2)}{f_{c,x_i}^2 + f^2} \quad (5-25)$$

In a log-log plot, for $f \ll f_{c,x_i}$, P_{x_i} is approximately constant ($\log P_{x_i} \approx \log(D/2\pi^2 f_{c,x_i}^2)$), while for $f \gg f_{c,x_i}$, it decreases linearly ($\log P_{x_i} \approx \log(D/2\pi^2) - 2\log f$).

Figure 5.10 shows the PSD for the position in the x direction for the previously described simulation. In order to average the spectrum over ensembles, the simulation was extended to cover 10 seconds instead of 2, resulting in a data set of 250×3 points. The data was then divided in a 100 smaller sets of 2500 points. The simulation data in Figure 5.10 (orange points) is the average of the PSDs calculated for each of the 100 smaller sets. This average PSD was fitted to a function $P(f) = A/(f_c^2 + f^2)$ (dashed curve), which gave a value of $f_c = 8.30Hz$ for the corner frequency, which is consistent with the theoretical value $f_c = 53.9/2\pi = 8.59Hz$.

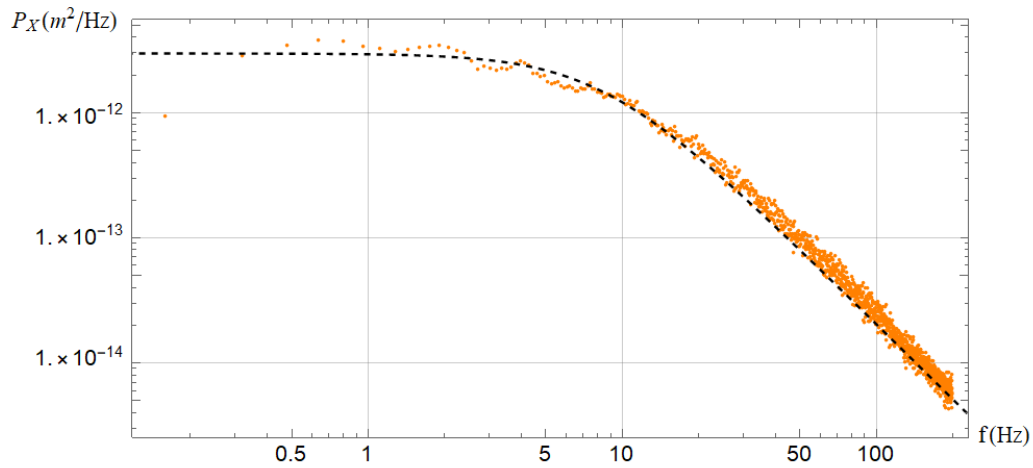


Figure 5.10: PSD calculated using the points from the previous simulation and a Lorentzian function fitted to it.

In the next chapter, we'll present an optical tweezer capable of trapping micro-spheres in a water medium in the intermediate regime described in Section 5.3, as well as the application of the motion analyses presented in Section 5.4.

6 Optical Tweezers: Experiment

In this chapter we describe the implementation of an optical tweezer capable of trapping particles in a water medium in the intermediate regime (size range from $0.5\ \mu\text{m}$ to $5\ \mu\text{m}$) using a laser with a wavelength of $780\ \text{nm}$. We also use the motion analysis presented in the last chapter to obtain information about the optical trap. Finally, we present our work under progress on an optical tweezer capable of trapping particles in vacuum.

The setup we used for trapping micron-sized spheres is shown in Figure 6.1. On Part I, the laser is collimated, passes through a QWP and a HWP, in order to acquire linear polarization in a specific direction and is reflected by a steering mirror *SM1*. On Part II, the beam is expanded by two lenses (omitted in the figure) in a configuration as the one shown in Figure 2.9(b), reflected by a second steering mirror *SM2* into the vertical direction and gets transmitted by a PBS. Then, an objective lens *O1* focuses the beam on a sample formed by a solution of micro-spheres dispersed in water, creating the optical trap itself.

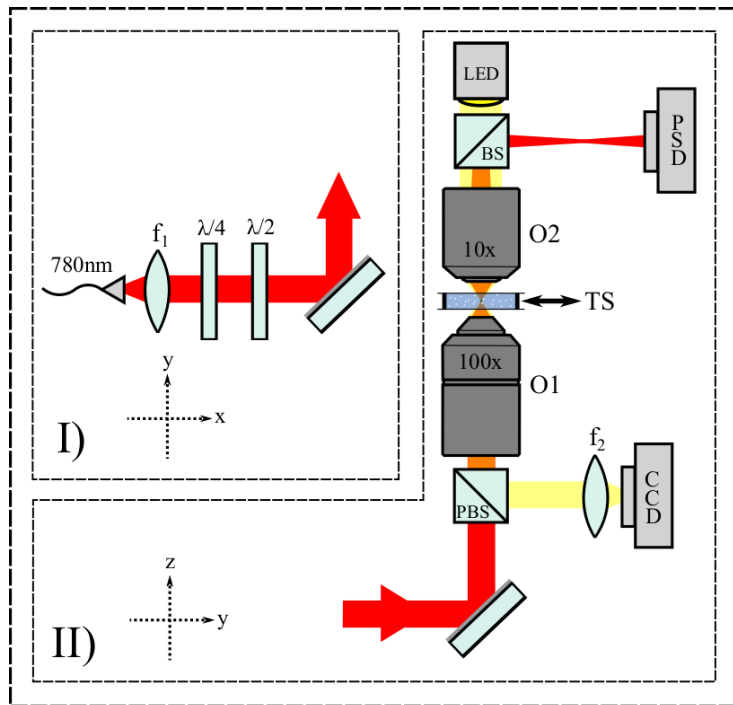


Figure 6.1: Schematic showing the optical setup we used in the implementation of our optical tweezer.

In order to visualize the micro-spheres, the light emitted by a Light Emitting Diode (LED) is partially transmitted by a BS and focused on the sample by a second objective lens O_2 , which acts as a microscope condenser. The first objective then acts as a typical microscope objective, collecting the light from the LED and creating an image of the sample. This collected light is reflected by the PBS and focused on a CCD camera sensor.

Finally, in order to measure the trapped particle's motion, we use an interferometry scheme. The laser beam transmitted by the trapped particle is collected by the objective lens O_2 and partially reflected by the BS onto a Position Sensitive Detector (PS Detector), which provides information about the particle's position, by means that will be explained in the next section.

6.1

General Aspects

6.1.1

Real position measurements

One of the main applications for optical tweezers the measurement of tiny forces [23, 29]. In such applications, an unknown force is applied to a trapped particle and the response of the particle is used to get information about the applied force. In order to do so, the trapped particle's dynamics must be well known, which involves knowing the trap stiffness κ , the drag coefficient γ and the medium's temperature T [52].

In the previous chapter we presented two quantities that can be calculated from the measurement of the particle's position in a given direction. In a real situation, rather than directly measuring the particle's position, a quantity that is proportional to the particle's position is measured. One might, for example, record a video of the trapped particle using a fast camera and then find out the particle's position at each frame using a software. Provided that the image is free of distortions, this would directly yield the particle's position in units of pixels, which would be proportional to the particle's real position.

An alternative method is to collect the light that is scattered by the trapped particle in the forward direction by placing an objective lens facing the objective lens responsible for creating the trap, as shown in Figure 6.1. Then, small displacements of the particle from the equilibrium position cause the collected light to be deviated by a small angle that is proportional to the particle's displacement [34]. To detect this deviation, a Position Sensitive Detector can be used.

A PS Detector is a device whose outputs are three different voltage signals

X, Y and SUM. The signal X (Y) is proportional to the total light power hitting the detector multiplied by the coordinate x_D (y_D) at which the light hits the detector. The signal SUM is simply proportional to the total power hitting the detector. Therefore:

$$X = c_X P x_D \quad Y = c_Y P y_D \quad SUM = c_{SUM} P \quad (6-1)$$

where c_X , c_Y and c_{SUM} are constants of proportionality.

When the beam is deviated due to the particle's displacement, the coordinate at which the light hits the detector changes. Therefore, measuring the signals X and SUM simultaneously, and then dividing X by SUM at each instant of time, yields a number \mathbb{X} proportional to the particle's position in the x direction, that is: $\mathbb{X} = \beta_x x$. The displacement of the point at which the beam hits the PS detector depends on several variables, such as the objective lens used to collect the forward scattered light, the distance from this objective lens to the trapped particle and to the PS detector and the particle's size. Therefore, the constant of proportionality β_x is, a priori, unknown.

Using the definitions given by Equations 5-20 and 5-23, it is easy to see that the autocorrelation function and the power spectral density for \mathbb{X} are given, respectively, by:

$$C_{\mathbb{X}}(\tau) = \beta_x^2 \frac{k_B T}{\kappa_x} e^{-\kappa_x \tau / \gamma} \quad (6-2a)$$

$$P_{\mathbb{X}}(f) = \beta_x^2 \frac{D / (2\pi^2)}{f_{c,x}^2 + f^2} \quad (6-2b)$$

Provided that the particle's size and the medium's temperature are well known, the drag coefficient γ can be calculated using Equation 5-14. If the particle is trapped near a surface, which is often the case when dealing with liquid media, the drag coefficient becomes:

$$\gamma_s(T) = \frac{\gamma(T)}{1 - \frac{9}{16} \left(\frac{R}{h}\right) + \frac{1}{8} \left(\frac{R}{h}\right)^3 - \frac{45}{256} \left(\frac{R}{h}\right)^4 - \frac{1}{16} \left(\frac{R}{h}\right)^5} \quad (6-3)$$

where R is the sphere's radius and h is the distance from the sphere center to the surface.

Once γ has been calculated from Equation 6-3, the spring constant κ_x can be determined from either measuring the corner frequency on the power spectral density, or the exponential characteristic time of the autocorrelation function. Finally, the constant β_x can be determined using the value of the autocorrelation function, given by Equation 5-21, for $\tau = 0$:

$$\beta_x^2 = \frac{C_x(0)\kappa_x}{k_B T} \quad (6-4)$$

Since the ACF is defined as an ensemble average, in order to calculate it, we measure the position of the particle with a sampling rate of 25 kHz over intervals of time of 0.1 s twenty times with an interval of about 2 s between each measurement. Since, as we'll see, the correlation time is much smaller than 2 s, each measurement can be considered a different realization of the experiment. Then, we average the twenty autocorrelation functions calculated for each interval of 0.1 s and take the result of this average to be one measurement of the autocorrelation function.

For the PSD, which is also defined as an ensemble average, we measure the position of the particle over intervals of 0.1 s fifty times, with an interval of about 2 s between each measurement. Then, a single measurement of the PSD is taken to be the average of the fifty power spectral densities calculated for each interval of 0.1 s.

As a final remark, it is necessary to say that we assume a perfectly Gaussian beam, implying equal spring constants in the x and y direction. Therefore, the measurements are made in only one direction. Also, since the position is given by the division between the voltages from signal X and signal SUM, the position is measured in arbitrary units (a.u.).

6.1.2 Experimental procedure

In our setup, a laser with a wavelength of 780 nm is collimated using an aspheric lens with a focal distance f_1 of 15.36 mm, resulting in a beam waist of 1.43 mm, which is further expanded by two lenses with focal distances 35.0 mm and 60.0 mm, resulting in a beam waist of about 2.5 mm. The wave plates are then rotated in order to maximize the transmission through the PBS. The alignment of the beam consists of 5 steps.

First, both objectives are removed from their mountings. As shown in Figure 6.2(a), the objective $O1$ (Olympus UPlanFLN 100x, NA=1.3) is replaced by a 2 inches tube having an iris threaded to it, while a second iris is placed before the PBS. The two steering mirrors are then used to make the beam pass through the centers of both irises, which is sufficient to provide coarse alignment.

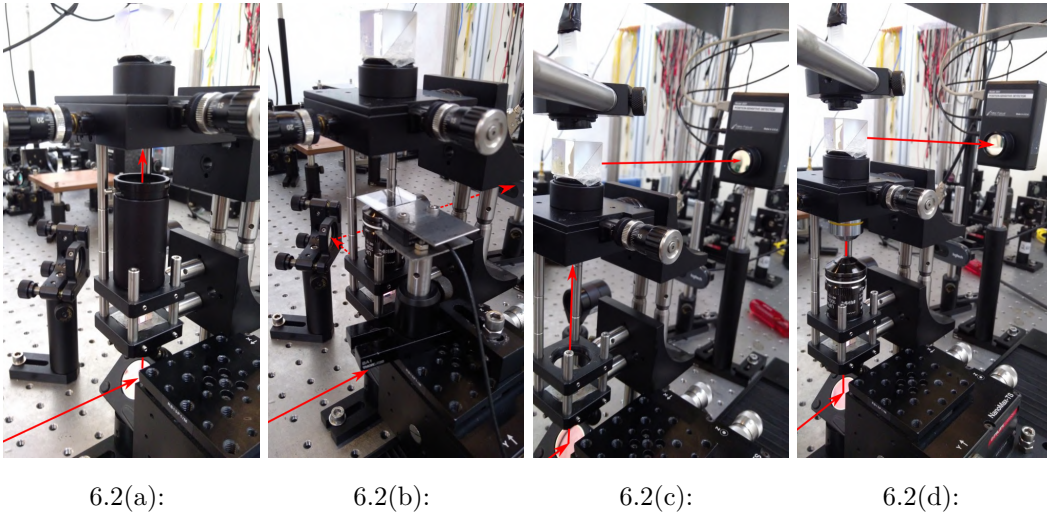
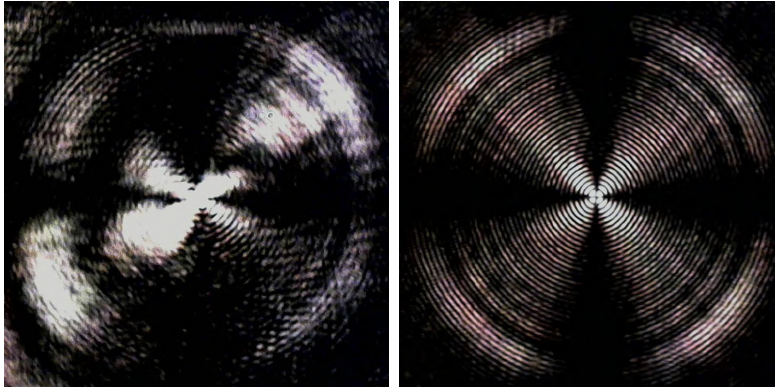


Figure 6.2: Alignment procedure used in our implementation: (a) Coarse alignment of the beam and the objective's longitudinal axis; (b) Positioning of the camera and fine alignment of the beam; (c) Positioning of the PS detector; (d) Positioning of the second objective lens. The solid red arrows represent the trapping laser beam, while the dashed red arrows represent the back reflection.

Then, the objective $O1$ is positioned and a coverslip is placed after it, as shown in Figure 6.2(b), causing the beam to be partially reflected back to the objective. The distance between the coverslip and the objective is adjusted in order to cause the back reflection to be collimated. Then, a lens with focal distance f_2 of 150 mm is used to focus the back reflection, and the CCD camera sensor (Logitech C270) is placed so that the beam is focused at the center of it. This ensures that the plane whose image is going to be formed at the CCD sensor is the same plane where the laser beam is focused. By moving the coverslip closer or further from the objective, fine alignment of the beam can be performed by using the steering mirrors to make the back reflection's pattern symmetric. Figure 6.3 shows the image seen on the camera when the beam is misaligned and when it is properly aligned.

After these two steps, the beam is aligned to the trapping objective, and the camera is properly placed. It is necessary then to place both the PS detector and the second objective lens. To do so, the first objective is once more removed and the PS detector is placed so that the beam reflected by the BS hits it in the center, as shown in Figure 6.2(c). Then, the two objectives are placed. The vertical position of the objective $O2$ (Olympus PlanN 10x, NA=0.25) is adjusted, by threading it more or less to its mounting, so that the beam is focused between the BS and the detector and fills almost all of the PS detector's sensor when hitting it. The horizontal position of the second

lens is adjusted, using the mount's knobs, which can be seen in Figure 6.2(d), to translate it, so that the beam hits the PS detector's sensor at its center.

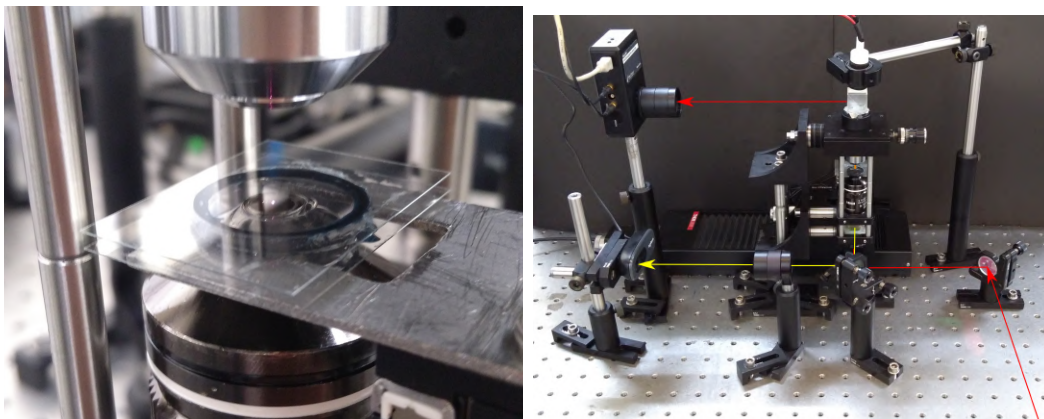


6.3(a):

6.3(b):

Figure 6.3: Back reflection pattern observed in the camera when: (a) the beam is not properly aligned; (b) the beam is properly aligned.

Finally, the sample containing the spheres can be placed. We use a sample such as the one shown in Figure 6.4(a): the water with spheres is placed between two coverslips that are partially fixed to a rubber ring using grease. The sample is held on a xyz translation stage (Thorlabs Max313/M), providing micrometric precision over the sample's position. Figure 6.4(b) shows our complete setup.



6.4(a):

6.4(b):

Figure 6.4: Final configuration of the optical setup with a sample in place: (a) sample containing spheres immersed in water; (b) complete optical tweezer setup. The red arrows represent the trapping laser beam, while the yellow ones represent the light emitted by the LED.

6.2

Initial tests

In order to test our optical tweezer we attempt to trap several different spheres. Once a sample containing a specific size of sphere was positioned, the translation stage was used to move one of the many spheres contained in the sample towards the laser focus. Figure 6.6 shows trapped spheres of seven different sizes and two different materials: Polystyrene spheres with diameters of $0.505 \mu\text{m}$, $0.746 \mu\text{m}$, $1.925 \mu\text{m}$, $3.00 \mu\text{m}$ and $4.52 \mu\text{m}$ and Silica spheres with diameters of $1.15 \mu\text{m}$ and $2.47 \mu\text{m}$.

In order to test if a sphere is stably trapped, we use the translation stage to move the sample. If a particle is stably trapped, the sample moves, together with all spheres that are not trapped, while the trapped particle remains still. This can be seen in Figure 6.5, that shows four frames of a video recorded while sphere (Silica, $2.47 \mu\text{m}$), marked by a red circle, was stably trapped and the sample was moved in the direction pointed by the arrow. As it can be seen, the spheres that are not trapped, marked by yellow circles, move together with the sample, while the trapped sphere remains in place.

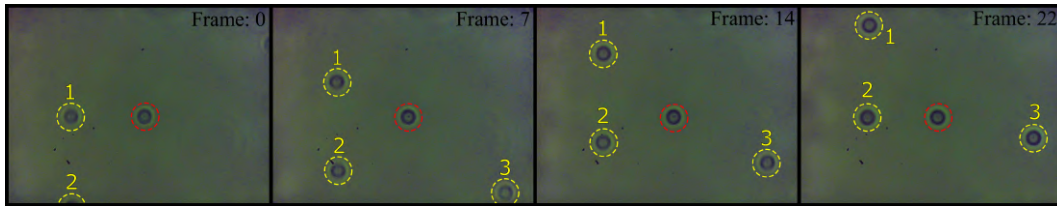


Figure 6.5: Trapped $2.47 \mu\text{m}$ Silica sphere. The time interval between frames is $1/15$ seconds and the sample is moving upwards. The red circle highlights the trapped particle, while the yellow circles highlight particles that are not trapped.

One interesting observed fact was the existence of two stable trapping positions when the $0.505 \mu\text{m}$ Polystyrene sphere was used, which are shown in Figures 6.6(a) and 6.6(b). This is due to the existence of multiple z 's satisfying $F_z(z) = 0$ and $F(z) < 0$, which are the conditions for stable trapping, when small particles are used [53].

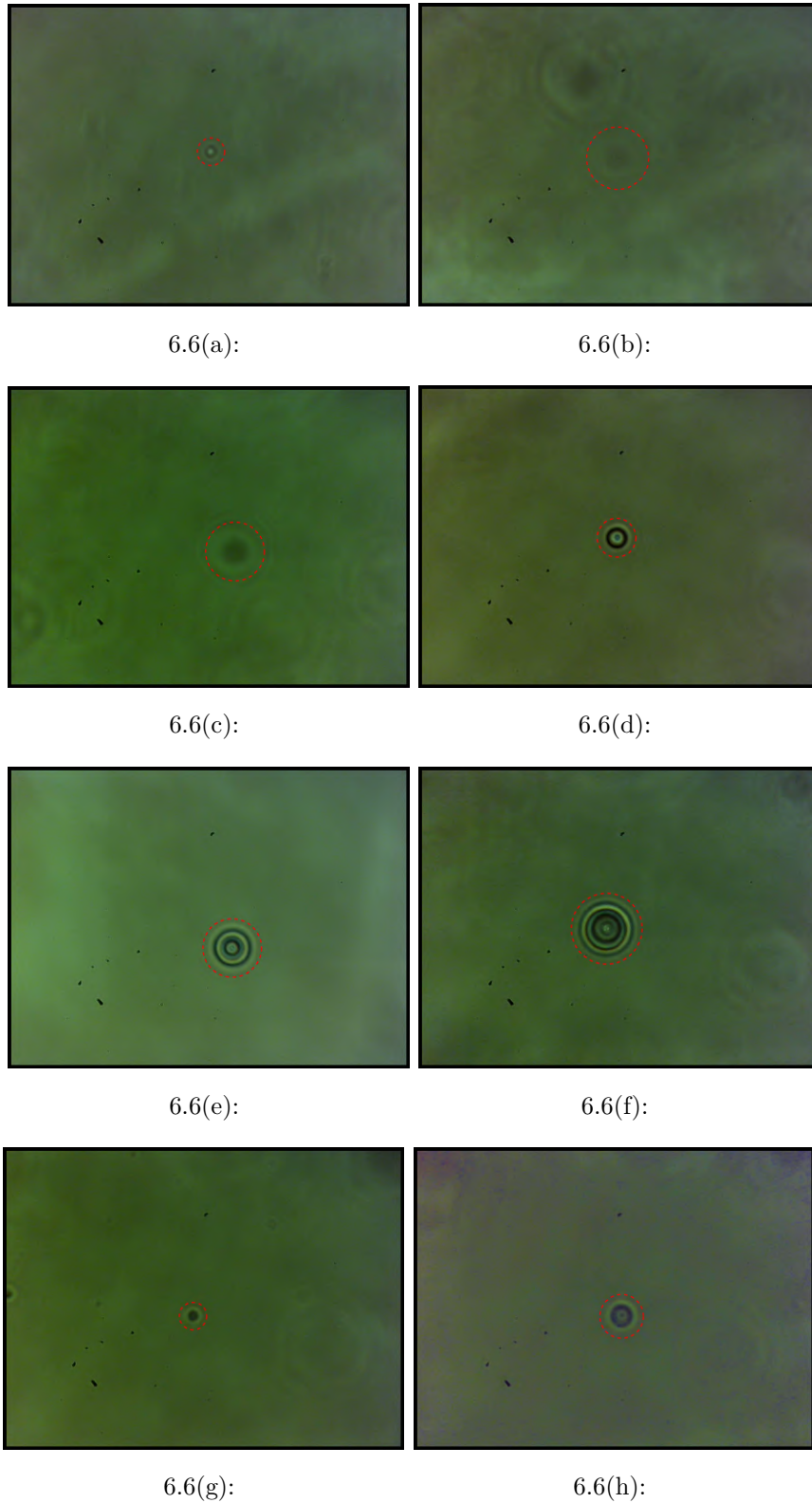


Figure 6.6: Micro-spheres of different diameters and materials in our optical trap. Polystyrene spheres: (a) $0.505\ \mu\text{m}$ at the first stable position; (b) $0.505\ \mu\text{m}$ at the second stable position; (c) $0.746\ \mu\text{m}$; (d) $1.925\ \mu\text{m}$; (e) $3.00\ \mu\text{m}$; (f) $4.52\ \mu\text{m}$. Silica spheres: (g) $1.15\ \mu\text{m}$; (h) $2.47\ \mu\text{m}$.

Besides the already mentioned spheres, we also tried to trap $0.99\ \mu\text{m}$ Polystyrene spheres, but stable trapping was not observed. Figure 6.7 shows an attempt of trapping one of those spheres. Initially, the sphere is positioned below the focus. Then, it is pulled by the optical force in the direction of the focus, but it ends up being pushed away from the focus. Thus, we can conclude that the force pushing the sphere in the direction of the propagation of the beam was greater than the force pulling the sphere towards the focus.

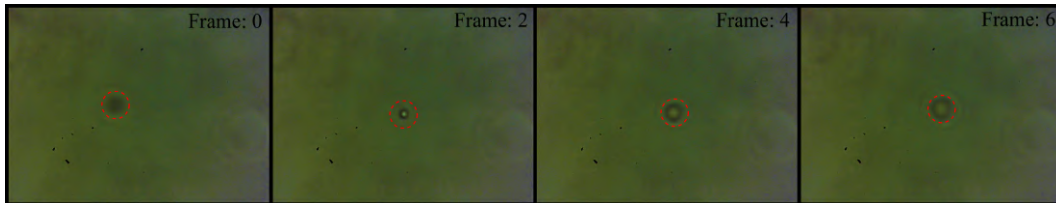


Figure 6.7: Attempt of trapping a $0.99\ \mu\text{m}$ Polystyrene sphere. The time interval between frames is $1/15$ seconds and the red circle indicates the particle's position.

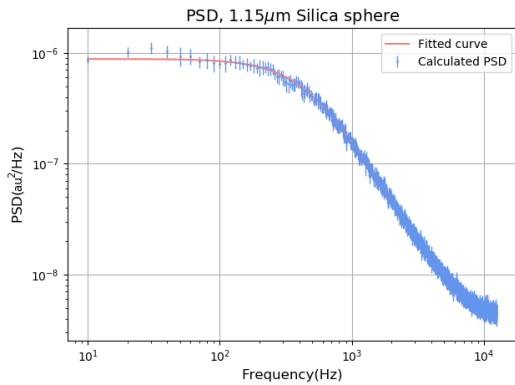
This behaviour was observed for other sizes of Polystyrene spheres we tested, but, differently from the $0.99\ \mu\text{m}$ one, they could be trapped after a few attempts. The same was not true for Silica spheres. This is justified by the refractive index of each material: while the refractive index is about 1.46 for Silica, it is equal to 1.59 for Polystyrene. The fact that the scattering force scales faster with the refractive index than the gradient force implies that it should be easier to trap Silica spheres than Polystyrene spheres.

6.3 Position Measurements

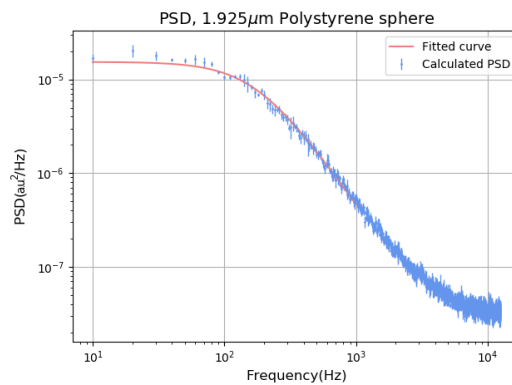
6.3.1 Power Spectral Density Analysis

The first method we used to study our optical tweezer was the power spectral density. Figure 6.8 shows the PSD for four different spheres: Polystyrene spheres with diameters of $1.925\ \mu\text{m}$ and $3.00\ \mu\text{m}$ and Silica spheres with diameters of $1.15\ \mu\text{m}$ and $2.47\ \mu\text{m}$. The laser power was $50\ \text{mW}$, the spheres were kept about $5\ \mu\text{m}$ away from the bottom coverslip (measured from the center of the sphere to the top surface of the coverslip) and the temperature of the room was $295\ \text{K}$. The plotted points represent the average of different PSD's (each of them calculated following the procedure described in the first section

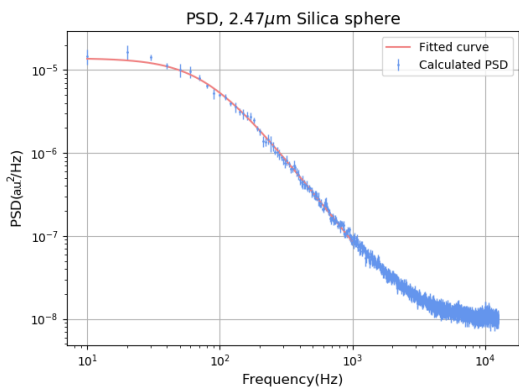
of this chapter), while the error bars represent the standard deviation for these averages.



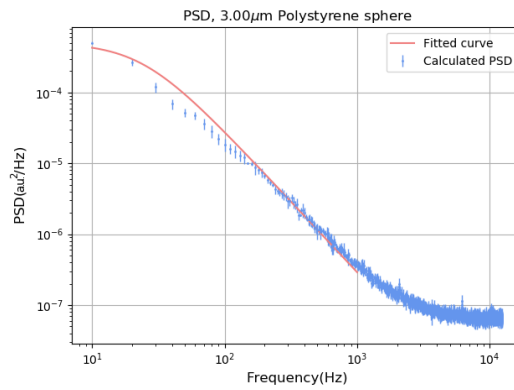
6.8(a):



6.8(b):



6.8(c):



6.8(d):

Figure 6.8: Power spectral density of the position of the trapped particle in one direction for four different micro-spheres: (a) $1.15 \mu\text{m}$ Silica sphere; (b) $1.925 \mu\text{m}$ Polystyrene sphere; (c) $2.47 \mu\text{m}$ Silica sphere; (d) $3.00 \mu\text{m}$ Polystyrene sphere.

By fitting each of these spectra to a Lorentzian, as given by equation 6-2b, we could get the values of the corner frequencies f_c , and, by using Equation 6-3 to calculate the drag coefficient, we could get the spring constants. We assumed an uncertainty of $0.5 \mu\text{m}$ in the distance between the sphere and the coverslip. Table 6.1 summarizes the results we obtained. The curves were fitted for frequencies up to 1 kHz. For larger frequencies, the PSD, which is supposed to decay linearly in a log-log plot, starts to decay not linearly due to low signal to noise ratio, until it becomes flat for frequencies larger than about 10 kHz.

Diameter (μm)	Averaged PSD's	$f_c(\text{Hz})$	$\kappa(\text{fN/nm})$
1.15	10	463.9 ± 7.0	32.18 ± 0.53
1.925	5	175.7 ± 0.5	21.39 ± 0.26
2.47	6	78.58 ± 2.04	12.70 ± 0.39
3.00	5	24.07 ± 0.29	4.89 ± 0.11

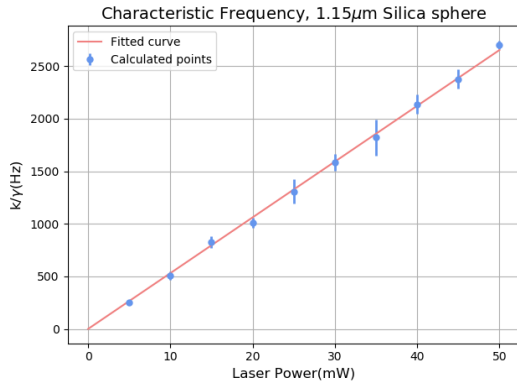
Table 6.1: Results obtained in the PSD analyses for four different spheres.

Also, since the PSD is discrete and is only evaluated for frequencies $f = n \times 10 \text{ Hz}$, where n is an integer, the fitted curve and the calculated PSD show poor agreement when the corner frequency is small, once the fitting process gets dominated by the linearly decaying part of the PSD. This can be seen in part D of Figure 6.8 for the $3.00 \mu\text{m}$ sphere ($f_c = 24.07 \pm 0.29 \text{ Hz}$).

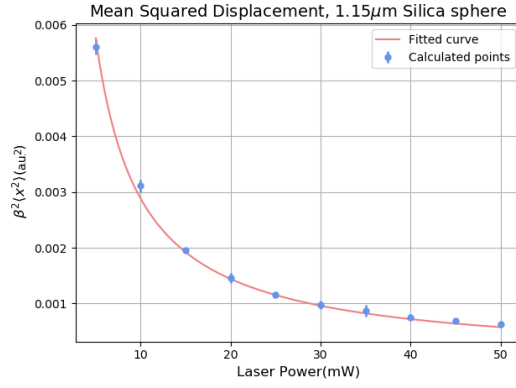
6.3.2 Autocorrelation Function Analysis

For the ACF analysis, we scanned the laser power from 5 mW to 50 mW, using 5 mW steps, and calculated the ACF, as described in the first chapter of this chapter, for each laser power value. Then, each ACF was fitted to the exponential given by Equation 6-2a. This yielded one value for κ/γ and one value for $C_{\mathbb{X}}(0) = \beta^2 \langle x^2 \rangle$ for each laser power. Figure 6.9 displays the fitted values for these two quantities. The points represent the values obtained by averaging the fitted values obtained by repeating the measurement four times, while the error bars represent the standard deviation for these averages.

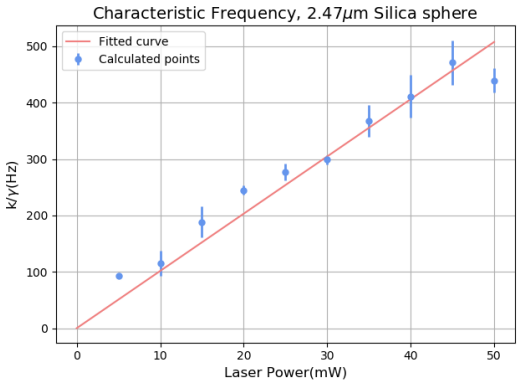
Since the force exerted by the laser beam is due to the transfer of momentum from the laser photons to the sphere and the laser power is proportional to the number of photons in the laser beam, we expect the spring constant to be proportional to the laser power. Therefore, we expect $\kappa/\gamma = aP$ and $C_{\mathbb{X}}(0) = b/P$, where a and b are constants and P is the laser. By fitting the plotted points to these curves, we can find expressions for $[\kappa/\gamma](P)$ and $[C_{\mathbb{X}}(0)](P)$.



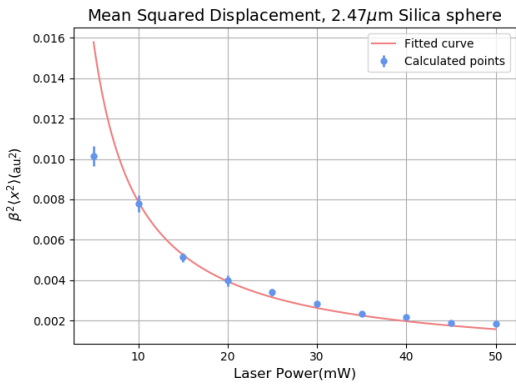
6.9(a):



6.9(b):



6.9(c):



6.9(d):

Figure 6.9: Characteristic frequency (κ/γ) as a function of the laser power for: (a) $1.15\ \mu\text{m}$ Silica and (c) $2.47\ \mu\text{m}$ Silica spheres; and mean squared displacement for: (b) $1.15\ \mu\text{m}$ and (d) $2.47\ \mu\text{m}$ Silica spheres.

Using Equation 6-3 to calculate γ_s for both spheres, we can get expressions for $\kappa(P)$, and by using these expressions together with Equation 5-22, we can get expressions for $\langle x^2 \rangle(P)$. Finally, dividing the expressions for $(C_x(0))(P)$ and $\langle x^2 \rangle(P)$, we can get the values of the parameters β that allows for the conversion between arbitrary units and particle displacement. Table 6.2 summarizes the obtained results.

D(μm)	A(fN/mW.nm) ($\kappa(P)=AP$)	B(nm^2mW) ($\langle x^2 \rangle=B/P$)	$\beta(10^{-3}/\text{nm})$
1.15	$(5.86 \pm 0.06) \times 10^{-1}$	$(6.95 \pm 0.07) \times 10^3$	5.23 ± 0.04
2.47	$(2.61 \pm 0.10) \times 10^{-1}$	$(1.56 \pm 0.06) \times 10^4$	2.34 ± 0.05

Table 6.2: Results obtained in the ACF analyses for two different spheres.

Using the value of A for each sphere, we find that $\kappa(50\ \text{mW}) = 29.3 \pm 0.3\ \text{fN}/\text{nm}$ for the $1.15\ \mu\text{m}$ and $\kappa(50\ \text{mW}) = 13.1 \pm 0.5\ \text{fN}/\text{nm}$ for the $2.47\ \mu\text{m}$,

which shows reasonable agreement between the PSD and the ACF analyses.

6.3.3

Discussions

The optical tweezer we implemented was capable of stably trapping spheres of different sizes and materials. Also, the measurement system based on forward scattering interferometry yielded good position measurements, that showed reasonable agreement with the theoretical analysis when both the PSD and the ACF were calculated [51].

One of the main difficulties in performing the measurements was the long time interval it took to perform data acquisition. This was mainly due to the use of an oscilloscope as the interface between the detector and the computer. Long measurement time imply higher probability of a second sphere entering the trap, which causes measurements to be interrupted. If an equipment capable of acquiring more data in less time is used in the future, we expect more precision in the measurements, due to increased number of data to be averaged.

7

Conclusions and Perspectives

In this work we presented the progress made towards the realization of a small force sensor based in the interaction between a membrane and a micro sphere inside a cavity. We studied cavities in different configurations, achieving a cavity finesse of about 1000. Also, we observed valleys in the reflection of the cavity that allows us to proceed to the stabilization of the cavity. We have also presented an optical tweezer capable of trapping micro-spheres of different sizes in a water medium, as well as the setup needed to measure the position of trapped particles. These achievements directly allows us to take the next steps, which are summarized in the rest of this chapter.

Cavity stabilization and subsequent implementations

In order to stabilize the cavity, we will use a Pound-Drever-Hall scheme, which is briefly summarized in Figure 7.1 [54]. A local oscillator LO generates a signal that is uses by a frequency modulator FM to modulate the laser's frequency. If the laser frequency is less than the cavity's resonance frequency, an increase in the frequency will decrease the cavity's reflection, which is measured by a detector DET. Therefore, the signal from DET will oscillate out of phase with the modulation signal. If the frequency is greater than the resonance frequency, the opposite will happen. Therefore, by using a mixer to compare the phases between the local oscillator's signal and the detector's signal, an error signal can be generated and used by a PID actuator to make the laser's frequency match the cavity's resonance frequency.

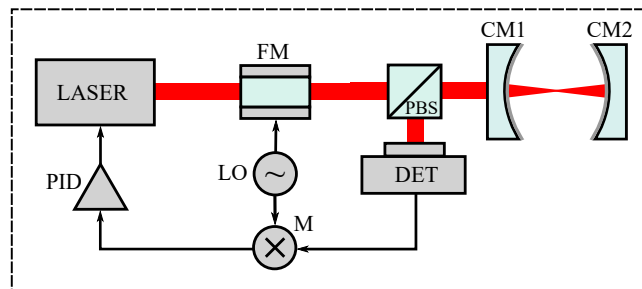


Figure 7.1: Simplified setup for implementing a Pound-Drever-Hall stabilization scheme.

Once that is done, we will be able to place the cavity inside a vacuum chamber, which we already have, and insert the membrane (Norcada NX5050CS) into the cavity in order to study its dynamics. When the membrane is placed, a cavity detuning $\omega_{cav}(x) = (c/L) \cos^{-1}[|r_c| \cos(4\pi x/\lambda)]$, where x is the membrane's position, L is the cavity's length, r_c is the membrane's reflection coefficient and λ is the wavelength, is introduced [55]. Therefore, by looking at the error signal generated by the PDH scheme, it is possible to get information about the membrane's position [27].

If the membrane is placed between two cavity's nodes, the detuning will be proportional, to lowest order, to x^2 [56, 57]. In this case, the Hamiltonian commutes with the membrane's phonon number operator, allowing for a quantum-non-demolition [58] measurement of the membrane's eigenstate [59].

The knowledge regarding optical cavities we acquired through this work together with the stabilization of the cavity will also be applied to implement a squeezed light source by placing a type-I nonlinear crystal inside the optical cavity. Since the uncertainty in the electric field of squeezed light is smaller than that of coherent light, it is possible that this light source can be used to improve the sensitivity of our final force sensor [60]. Another possibility is to use the *membrane in the middle* setup to create squeezed light [61].

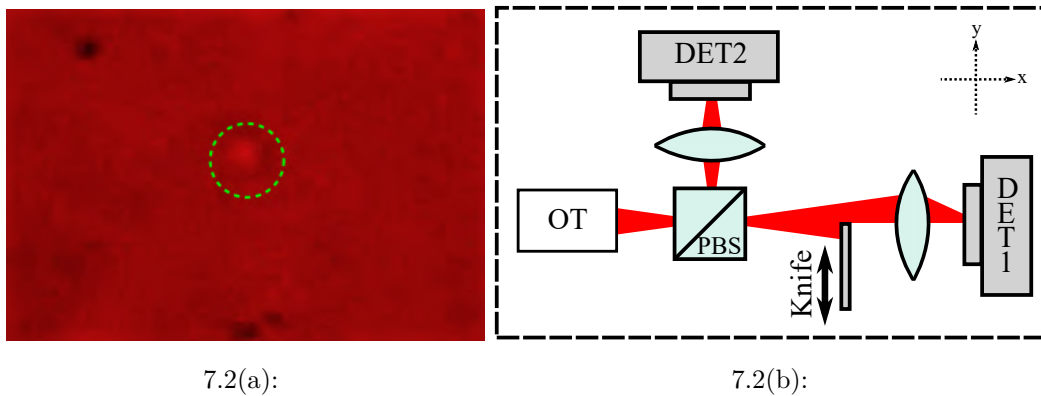
Future work with optical traps in liquid media

Although we need an optical tweezer capable of trapping spheres in vacuum, the optical tweezer we implemented offers interesting possibilities to be explored in the future. First of them, is the implementation of an optical tweezer using general-purpose optical elements, which would be of interest to the Optics community [62].

In this setup, the high numerical aperture objective lens, which is an expensive element and is often not encountered in optics laboratories, is replaced by an aspheric lens having a small focal distance. We have performed some tests using this kind of lens (Thorlabs C330TM-A) in our tweezer, and $2.47 \mu\text{m}$ Silica particles could be trapped for several seconds by a 532 nm laser, which was confirmed by moving the sample and observing that the sphere remained still. Figure 7.2(a) shows a sphere trapped under those conditions. The laser used was a commercial laser pointer coupled to a fiber in order to spatially filter it, which could mean even further cost reduction.

The PS detector can also be replaced by a pair of lenses, a beam splitter and a pair of silicon detectors, all of which are commonly encountered in optics laboratories. This equivalent system is illustrated in Figure 7.2(b). The forward

scattered light collected in an optical tweezer is splitted into two beams, one of which is focused on a detector DET 1, while the other is partially blocked by a knife placed so that only half of the beam gets to the detector DET2. In this configuration, the signal of DET1 measures the total collected power, while the detector DET2 outputs a voltage that is proportional to the total power and to the beam deviation. Therefore, this setup generates signals that are analogous to the signals X (or Y, depending on which arm the knife is placed) and SUM from a PS detector.



7.2(a):

7.2(b):

Figure 7.2: Reduced cost optical tweezer implementation: (a) $2.47 \mu\text{m}$ Silica sphere trapped by an aspheric lens; (b) alternative setup for measuring a trapped particle's position.

Another possibility we would like to explore is the trapping of particles that have a refractive index smaller than that of the medium in which they are in. If the particle's refractive index is smaller than the medium's refractive index, the particles will get expelled from the regions in which the laser intensity is higher [8]. Therefore, in order to trap a particle in this regime, we have to use laser beams that have a dark spot surrounded by a high intensity region at its focus.

Figure 7.3 shows the transverse intensity pattern at the focal plane resulting from the interference of a Gaussian mode and a $l = 0, p = 1$ Laguerre-Gauss mode having a phase difference of π at the focal plane. As it can be seen, the intensity is null at the center of the beam. If the right modes are interfered, this behaviour can be extended to the longitudinal intensity pattern [63, 64], and the a sphere having refractive index smaller than the medium's refractive index could, at least in principle, be trapped in the dark focal region, encapsulated by a high intensity light layer. This might useful in biology applications when dealing with microorganisms that are damaged by the high intensity present in the focus of a regular optical tweezer [65, 66].

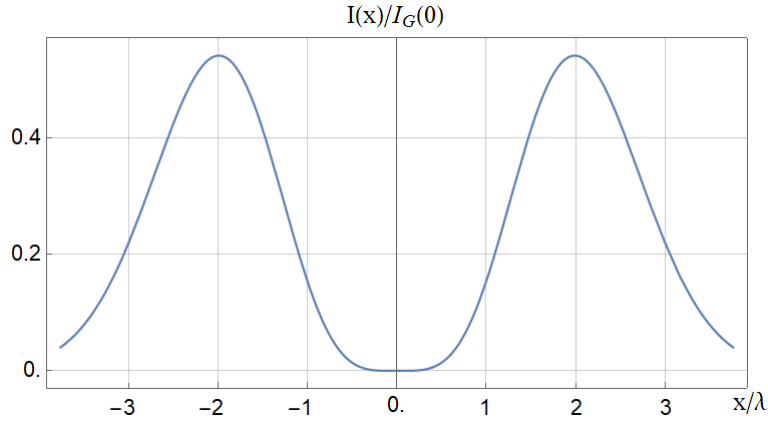


Figure 7.3: Intensity pattern resulting from the interference between a Gaussian beam and a $l = 0, p = 1$ Laguerre-Gauss beam having a phase difference of π .

Optical tweezers in vacuum

We have already started implementing an optical tweezer in vacuum, using a setup as the one shown in Figure 7.4. The system can be broken down into three parts. First, there is the optical trap itself. A 780 nm laser beam is collimated using a lens f_1 reflected by two steering mirrors $SM1$ and $SM2$, transmitted by a dichroic mirror $DM1$ and focused by an objective lens, which is inside a vacuum chamber, creating the optical trap.

In order to see the trapped particle, a 405 nm laser is focused by a lens f_2 at the objective lens focal region. If a particle is trapped, it will scatter the 405 nm beam, and this scattered light will be collected by the objective lens. This collected is then reflected by the dichroic mirror and focused by a lens f_3 on a CCD camera sensor. In order to measure the particle position, we can split the collected 405 nm light into two beams and focus one of them in a PS detector. Alternatively, we can place a second objective, as we did in our optical tweezer in water, and collect the forward scattered light.

Finally, we have the system that carries the spheres into the vacuum chamber [67]. With the valve $V1$ open, while the valve $V2$ is closed, the vacuum pump reduces the pressure inside the vacuum chamber to a pressure of 1 mbar. Then, a nebulizer NB nebulizes a solution made of spheres and isopropyl alcohol, creating a cloud of spheres inside a glass dome. The valve $V1$ is closed and the valve $V2$ is opened. The pressure difference between the vacuum chamber and the dome, then, pushes cloud to the chamber's interior. Once a sphere is trapped, the pressure can be once again reduced.

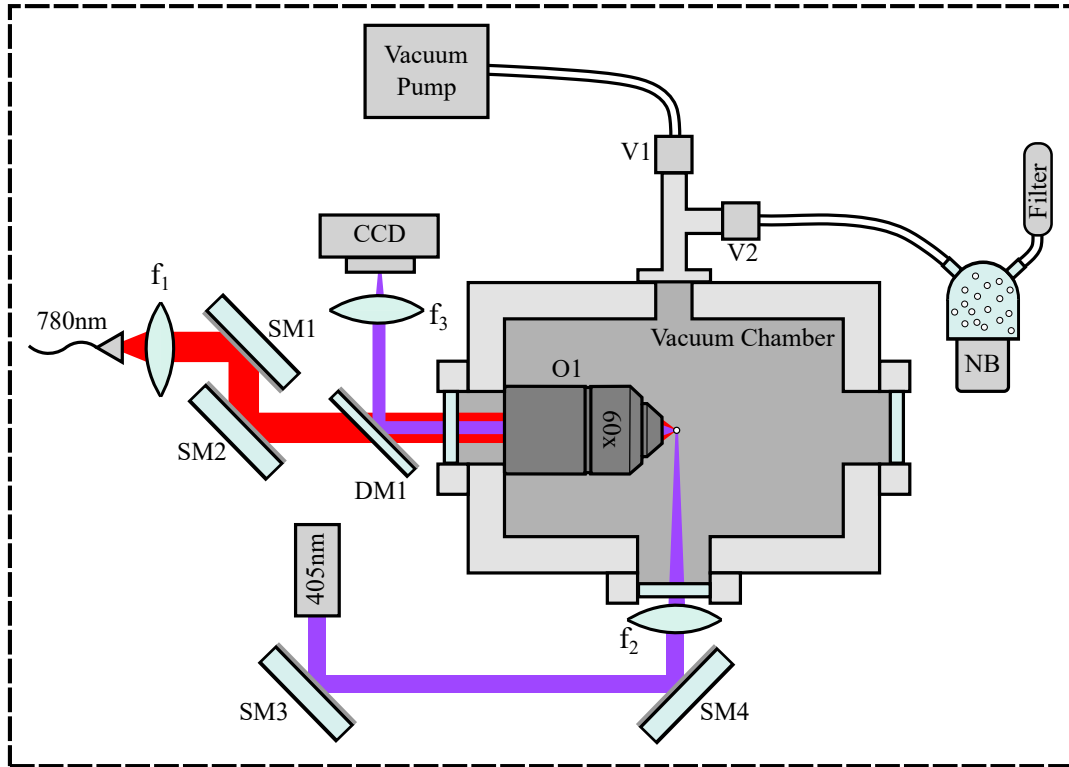


Figure 7.4: Intensity pattern resulting from the interference between a Gaussian beam and a $l = 0, p = 1$ Laguerre-Gauss beam having a phase difference of π .

Up to now, we haven't been able to observe stably trapped particles in our system. This is mainly due to two factors. First, we do not have an objective with high enough numerical aperture to use in vacuum [68]. The objective used in the optical tweezer in water is an oil immersion objective, having poor performance when used to focus light in a gas (or vacuum) medium. Therefore, we have only tested our system using an objective with a numerical aperture of 0.7 (Olympus LUCPlanFLN 60x). One possible solution for that would be the use of a custom made objective lens, which would also allow for the achievement of lower pressures inside the vacuum chamber [69].

The second factor regards the laser power we use and the size of the particle we are trying to trap. The 780 nm laser provides a power of $50mW$, which is further reduced due to the necessity of overfilling [70], and the Silica particle has a radius of 73 nm. This means we would be working in the dipole regime and, therefore, the laser power would have to be high enough in order to create a potential much larger than the particle's average kinetic energy [47].

For the time being, we have been using the image system to observe the motion of the particles inside the chamber in order to study them in terms

of statistical mechanics [71, 72]. Another student is currently developing a software capable of tracking the spheres in the image provided by the CCD camera and differentiate their masses by analysing their trajectories. We hope this will clarify if the particles we observe are the 73 nm Silica spheres or a droplet consisting of the particle immersed in isopropyl alcohol. Figure 7.5 shows four spheres, with their trajectories traced out by this software.

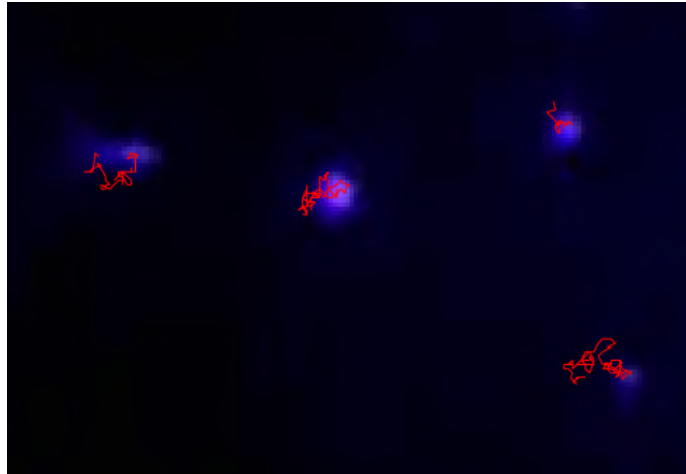


Figure 7.5: Spheres inside our chamber and their trajectories, traced out by a software. Image courtesy of Igor Brandão.

The capability to trap nanospheres in vacuum, together with the realization of a setup having a membrane inside a cavity, will allow us to proceed with the implementation of the force sensor. Building this sensor would be a great achievement, since a setup that integrates a membrane, a trapped sphere and a Fabry-Perót cavity is yet to be studied, although progress has been made in this direction over the past few years.

As we've already pointed out, the interaction between membranes and a cavities has been extensively studied [25, 27, 73], as well as between levitated spheres and cavities [26, 74, 75]. The levitation of a nanosphere near a membrane has also been realized, with subwavelength distances being achieved [76]. Therefore, combining these three elements in a single setup would be of great interest to the community.

One possible way to do so would be to apply a reflective coating to the front end of an objective lens and use it as the output mirror of a Fabry-Pérot cavity. This configuration is shown in Figure 7.6. The reflective coating - represented in a light grey tonality - has high transmission for the wavelength of the trapping laser - represented by the blue beam - and high reflectivity for the wavelength of the cavity laser - represented by the red beam. The membrane is positioned near the focal point, so that the particle is trapped close to it. In

a configuration like this, the cavity's optical field, the membrane's motion and the sphere's motion would be coupled.

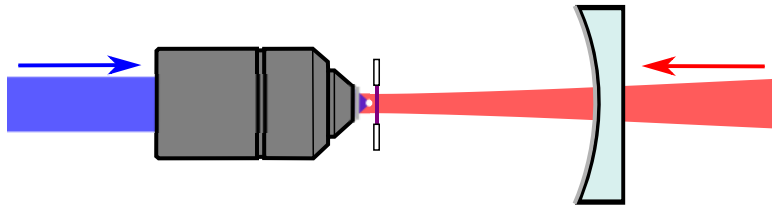


Figure 7.6: Schematic of a setup in which the cavity's optical field, the membrane's motion and the sphere's motion are coupled.

Bibliography

- [1] SABRA, A. I. **Theories of Light: From Descartes to Newton**. Cambridge University Press, 1981.
- [2] FRISCH, R. **Zeitschrift für Physik**. Experimenteller nachweis des einsteinschen strahlungsdruckes, journal, v.86, n.1-2, p. 42–48, jan 1933.
- [3] BETH, R. A. **Physical Review**. Mechanical detection and measurement of the angular momentum of light, journal, v.50, p. 115–125, Jul 1936.
- [4] MAIMAN, T. H. **Nature**. Stimulated optical radiation in ruby, journal, v.187, n.4736, p. 493–494, aug 1960.
- [5] WEICHEL, H.; DAVID, C. D. ; AVIZONIS, P. V. **Applied Physics Letters**. EFFECTS OF RADIATION PRESSURE ON a LASER-PRODUCED PLASMA, journal, v.13, n.11, p. 376–379, dec 1968.
- [6] ASHKIN, A. **Physical Review Letters**. Atomic-beam deflection by resonance-radiation pressure, journal, v.25, n.19, p. 1321–1324, nov 1970.
- [7] HORA, H. **Physics of Fluids**. Nonlinear confining and deconfining forces associated with the interaction of laser radiation with plasma, journal, v.12, n.1, p. 182, 1969.
- [8] ASHKIN, A. **Physical Review Letters**. Acceleration and trapping of particles by radiation pressure, journal, v.24, n.4, p. 156–159, Jan. 1970.
- [9] ASHKIN, A.; DZIEDZIC, J. M.; BJORKHOLM, J. E. ; CHU, S. **Optics Letters**. Observation of a single-beam gradient force optical trap for dielectric particles, journal, v.11, n.5, p. 288, may 1986.
- [10] GAO, D.; DING, W.; NIETO-VESPERINAS, M.; DING, X.; RAHMAN, M.; ZHANG, T.; LIM, C. ; QIU, C.-W. **Light: Science & Applications**. Optical manipulation from the microscale to the nanoscale: fundamentals, advances and prospects, journal, v.6, n.9, p. e17039–e17039, mar 2017.
- [11] DIENEROWITZ, M. **Journal of Nanophotonics**. Optical manipulation of nanoparticles: a review, journal, v.2, n.1, p. 021875, sep 2008.

- [12] APPLGATE, R. W.; MARR, D. W. M.; SQUIER, J. ; GRAVES, S. W. **Optics Express**. Particle size limits when using optical trapping and deflection of particles for sorting using diode laser bars, journal, v.17, n.19, p. 16731, sep 2009.
- [13] HODGSON, N.; WEBER, H. **Optical Resonators**. Springer London, 1997.
- [14] FABRY, C.; PEROT, A. **The Astrophysical Journal**. On a new form of interferometer, journal, v.13, p. 265, may 1901.
- [15] FABRE, C.; DEVOE, R. G. ; BREWER, R. G. **Optics Letters**. Ultrahigh-finesse optical cavities, journal, v.11, n.6, p. 365, jun 1986.
- [16] VAUGHAN, M. **The Fabry-Perot Interferometer: History, Theory, Practice and Applications (Series in Optics and Optoelectronics)**. CRC Press, 1989.
- [17] FAVERO, I.; MARQUARDT, F. **New Journal of Physics**. Focus on optomechanics, journal, v.16, n.8, p. 085006, aug 2014.
- [18] CORBITT, T.; OTTAWAY, D.; INNERHOFER, E.; PELC, J. ; MAVALVALA, N. **Physical Review A**. Measurement of radiation-pressure-induced optomechanical dynamics in a suspended fabry-perot cavity, journal, v.74, n.2, aug 2006.
- [19] ASPELMEYER, M.; KIPPENBERG, T. J. ; MARQUARDT, F. **Reviews of Modern Physics**. Cavity optomechanics, journal, v.86, n.4, p. 1391–1452, dec 2014.
- [20] BOWEN, W. P. **Quantum optomechanics**. In: CLEO PACIFIC RIM CONFERENCE. OSA, 2018.
- [21] WILSON, D. J.; REGAL, C. A.; PAPP, S. B. ; KIMBLE, H. J. **Physical Review Letters**. Cavity optomechanics with stoichiometric SiN films, journal, v.103, n.20, nov 2009.
- [22] FONSECA, P.; ARANAS, E.; MILLEN, J.; MONTEIRO, T. ; BARKER, P. **Physical Review Letters**. Nonlinear dynamics and strong cavity cooling of levitated nanoparticles, journal, v.117, n.17, oct 2016.
- [23] HEBESTREIT, E.; FRIMMER, M.; REIMANN, R. ; NOVOTNY, L. **Physical Review Letters**. Sensing static forces with free-falling nanoparticles, journal, v.121, n.6, aug 2018.

- [24] JAIN, V.; GIESELER, J.; MORITZ, C.; DELLAGO, C.; QUIDANT, R.; NOVOTNY, L. **Physical Review Letters**. Direct measurement of photon recoil from a levitated nanoparticle, journal, v.116, n.24, jun 2016.
- [25] PIERGENTILI, P.; CATALINI, L.; BAWAJ, M.; ZIPPILLI, S.; MALOSSI, N.; NATALI, R.; VITALI, D.; GIUSEPPE, G. D. **New Journal of Physics**. Two-membrane cavity optomechanics, journal, v.20, n.8, p. 083024, aug 2018.
- [26] DELIĆ, U.; GRASS, D.; REISENBAUER, M.; DAMM, T.; WEITZ, M.; KIESEL, N.; ASPELMEYER, M. Levitated cavity optomechanics in high vacuum, journal, 2019.
- [27] THOMPSON, J. D.; ZWICKL, B. M.; JAYICH, A. M.; MARQUARDT, F.; GIRVIN, S. M.; HARRIS, J. G. E. **Nature**. Strong dispersive coupling of a high-finesse cavity to a micromechanical membrane, journal, v.452, n.7183, p. 72–75, Mar. 2008.
- [28] GERACI, A. A.; PAPP, S. B.; KITCHING, J. **Physical Review Letters**. Short-range force detection using optically cooled levitated microspheres, journal, v.105, n.10, p. 101101, Aug. 2010.
- [29] RIDER, A. D.; MOORE, D. C.; BLAKEMORE, C. P.; LOUIS, M.; LU, M.; GRATTA, G. **Physical Review Letters**. Search for screened interactions associated with dark energy below the 100 μm length scale, journal, v.117, n.10, p. 101101, Aug. 2016.
- [30] ETHER, D. S.; PIRES, L. B.; UMRATH, S.; MARTINEZ, D.; AYALA, Y.; PONTES, B.; DE S. ARAÚJO, G. R.; FRASES, S.; INGOLD, G.-L.; ROSA, F. S. S.; VIANA, N. B.; NUSSENZVEIG, H. M.; NETO, P. A. M. **EPL (Europhysics Letters)**. Probing the casimir force with optical tweezers, journal, v.112, n.4, p. 44001, nov 2015.
- [31] PATERNOSTRO, M.; GIGAN, S.; KIM, M. S.; BLASER, F.; BÖHM, H. R.; ASPELMEYER, M. **New Journal of Physics**. Reconstructing the dynamics of a movable mirror in a detuned optical cavity, journal, v.8, n.6, p. 107–107, jun 2006.
- [32] JACKSON, J. D. **Classical electrodynamics; 2nd ed.** New York, NY: Wiley, 1975.
- [33] MANDEL, L.; WOLF, E. **Optical Coherence and Quantum Optics.** Cambridge University Press, 1995.

- [34] JONES, P. H.; MARAGÒ, O. M. ; VOLPE, G. **Optical Tweezers: Principles and Applications**. Cambridge University Press, 2015.
- [35] BUTKOV, E. **Mathematical physics**. Addison-Wesley series in advanced physics. Addison-Wesley Pub. Co., 1968.
- [36] ANDERSON, D. Z. **Applied Optics**. Alignment of resonant optical cavities, journal, v.23, n.17, p. 2944, sep 1984.
- [37] KOGELNIK, H.; LI, T. **Appl. Opt.** Laser beams and resonators, journal, v.5, n.10, p. 1550–1567, Oct 1966.
- [38] SALEH, B. E. A. **Fundamentals of Photonics**. Wiley-Blackwell, 2019.
- [39] RODRIGUES, R. B. **Simetria de momento angular orbital entre feixes gêmeos produzidos por um oscilador paramétrico Ótico tipo ii**. Rio de Janeiro, RJ, 2018. Master's thesis - Universidade Federal Fluminense.
- [40] HERCHER, M. **Applied Optics**. The spherical mirror fabry-perot interferometer, journal, v.7, n.5, p. 951, may 1968.
- [41] MONTEIRO, F.; GHOSH, S.; FINE, A. G. ; MOORE, D. C. **Physical Review A**. Optical levitation of 10-ng spheres with nano- g acceleration sensitivity, journal, v.96, n.6, p. 063841, Dec. 2017.
- [42] MOORE, D. C.; RIDER, A. D. ; GRATTA, G. **Physical Review Letters**. Search for millicharged particles using optically levitated microspheres, journal, v.113, n.25, p. 251801, Dec. 2014.
- [43] ASHKIN, A.; DZIEDZIC, J. M. ; YAMANE, T. **Nature**. Optical trapping and manipulation of single cells using infrared laser beams, journal, v.330, n.6150, p. 769–771, Dec. 1987.
- [44] PANG, Y.; SONG, H.; KIM, J. H.; HOU, X. ; CHENG, W. **Nature Nanotechnology**. Optical trapping of individual human immunodeficiency viruses in culture fluid reveals heterogeneity with single-molecule resolution, journal, v.9, n.8, p. 624–630, Aug. 2014.
- [45] BLOCK, S. M.; BLAIR, D. F. ; BERG, H. C. **Nature**. Compliance of bacterial flagella measured with optical tweezers, journal, v.338, n.6215, p. 514–518, Apr. 1989.

- [46] WANG, X.; CHEN, S.; KONG, M.; WANG, Z.; COSTA, K. D.; LI, R. A.; SUN, D. **Lab on a Chip**. Enhanced cell sorting and manipulation with combined optical tweezer and microfluidic chip technologies, journal, v.11, n.21, p. 3656, 2011.
- [47] LI, T. **Fundamental Tests of Physics with Optically Trapped Microspheres**. Springer New York, 2013.
- [48] ALBALADEJO, S.; MARQUÉS, M. I.; LAROCHE, M.; SÁENZ, J. J. **Physical Review Letters**. Scattering forces from the curl of the spin angular momentum of a light field, journal, v.102, n.11, mar 2009.
- [49] NIEMINEN, T. A.; LOKE, V. L. Y.; STILGOE, A. B.; KNÖNER, G.; BRAŃCZYK, A. M.; HECKENBERG, N. R.; RUBINSZTEIN-DUNLOP, H. **Journal of Optics A: Pure and Applied Optics**. Optical tweezers computational toolbox, journal, v.9, n.8, p. S196–S203, jul 2007.
- [50] PURCELL, E. M. **American Journal of Physics**. Life at low Reynolds number, journal, v.45, n.1, p. 3–11, jan 1977.
- [51] BERG-SØRENSEN, K.; FLYVBJERG, H. **Review of Scientific Instruments**. Power spectrum analysis for optical tweezers, journal, v.75, n.3, p. 594–612, mar 2004.
- [52] JUN, Y.; TRIPATHY, S. K.; NARAYANAREDDY, B. R.; MATTSON-HOSS, M. K.; GROSS, S. P. **Biophysical Journal**. Calibration of optical tweezers for in vivo force measurements: How do different approaches compare?, journal, v.107, n.6, p. 1474–1484, sep 2014.
- [53] VIANA, N. B.; ROCHA, M. S.; MESQUITA, O. N.; MAZOLLI, A.; NETO, P. A. M.; NUSSENZVEIG, H. M. **Physical Review E**. Towards absolute calibration of optical tweezers, journal, v.75, n.2, feb 2007.
- [54] BLACK, E. D. **American Journal of Physics**. An introduction to Pound–Drever–Hall laser frequency stabilization, journal, v.69, n.1, p. 79–87, jan 2001.
- [55] JAYICH, A. M.; SANKEY, J. C.; ZWICKL, B. M.; YANG, C.; THOMPSON, J. D.; GIRVIN, S. M.; CLERK, A. A.; MARQUARDT, F.; HARRIS, J. G. E. **New Journal of Physics**. Dispersive optomechanics: a membrane inside a cavity, journal, v.10, n.9, p. 095008, sep 2008.
- [56] HAUER, B. D.; METELMANN, A.; DAVIS, J. P. **Physical Review A**. Phonon quantum nondemolition measurements in nonlinearly coupled optomechanical cavities, journal, v.98, n.4, p. 043804, Oct. 2018.

- [57] LUDWIG, M.; SAFAVI-NAEINI, A. H.; PAINTER, O. ; MARQUARDT, F. **Physical Review Letters**. Enhanced quantum nonlinearities in a two-mode optomechanical system, journal, v.109, n.6, p. 063601, Aug. 2012.
- [58] BRAGINSKY, V. B.; VORONTSOV, Y. I. ; THORNE, K. S. **Science**. Quantum nondemolition measurements, journal, v.209, n.4456, p. 547, Aug. 1980.
- [59] MIAO, H.; DANILISHIN, S.; CORBITT, T. ; CHEN, Y. **Physical Review Letters**. Standard quantum limit for probing mechanical energy quantization, journal, v.103, n.10, p. 100402, Sept. 2009.
- [60]
- [61] PURDY, T. P.; YU, P.-L.; PETERSON, R. W.; KAMPEL, N. S. ; REGAL, C. A. **PRX**. Strong optomechanical squeezing of light, journal, v.3, n.3, p. 031012, Sept. 2013.
- [62] CANDIA, C. N. H.; MARTÍNEZ, S. T. ; GUTIÉRREZ-MEDINA, B. **PLoS ONE**. A minimal optical trapping and imaging microscopy system, journal, v.8, n.2, p. e57383, feb 2013.
- [63] ARLT, J.; PADGETT, M. J. **Opt. Lett.** Generation of a beam with a dark focus surrounded by regions of higher intensity:the optical bottle beam, journal, v.25, n.4, p. 191–193, Feb. 2000.
- [64] DU, T.; WANG, T. ; WU, F. **Optics Communications**. Generation of three-dimensional optical bottle beams via focused non-diffracting bessel beam using an axicon, journal, v.317, p. 24–28, apr 2014.
- [65] RASMUSSEN, M. B.; ODDERSHEDE, L. B. ; SIEGUMFELDT, H. **Applied and environmental microbiology**. Optical tweezers cause physiological damage to escherichia coli and listeria bacteria, journal, v.74, n.18310432, p. 2441–2446, Apr. 2008.
- [66] KALANTARIFARD, F.; ELAHI, P.; MAKEY, G.; MARAGÒ, O. M.; ILDAY, F. M. ; VOLPE, G. **Nature Communications**. Intracavity optical trapping of microscopic particles in a ring-cavity fiber laser, journal, v.10, n.1, p. 2683, June 2019.
- [67] SUMMERS, M. D.; BURNHAM, D. R. ; MCGLOIN, D. **Opt. Express**. Trapping solid aerosols with optical tweezers: A comparison between gas and liquid phase optical traps, journal, v.16, n.11, p. 7739–7747, May 2008.

- [68] LI, N.; ZHU, X.-M.; LI, W.-Q.; FU, Z.-H.; HU, M.-Z. ; HU, H.-Z. **Frontiers of Information Technology & Electronic Engineering**. Review of optical tweezers in vacuum, journal, v.20, n.5, p. 655–673, May 2019.
- [69] ROBENS, C.; BRAKHANE, S.; ALT, W.; KLEISSLER, F.; MESCHEDÉ, D.; MOON, G.; RAMOLA, G. ; ALBERTI, A. **Opt. Lett.** High numerical aperture ($na=0.92$) objective lens for imaging and addressing of cold atoms, journal, v.42, n.6, p. 1043–1046, Mar. 2017.
- [70] VIANA, N. B.; ROCHA, M. S.; MESQUITA, O. N.; MAZOLLI, A. ; NETO, P. A. M. **Appl. Opt.** Characterization of objective transmittance for optical tweezers, journal, v.45, n.18, p. 4263–4269, June 2006.
- [71] LI, T.; KHEIFETS, S.; MEDELLIN, D. ; RAIZEN, M. G. **Science**. Measurement of the instantaneous velocity of a brownian particle, journal, v.328, n.5986, p. 1673, June 2010.
- [72] LI, T.; RAIZEN, M. G. **Annalen der Physik**. Brownian motion at short time scales, journal, v.525, n.4, p. 281–295, jan 2013.
- [73] NEWSOM, D. C.; LUNA, F.; FEDOSEEV, V.; LÖFFLER, W. ; BOUWMEESTER, D. Optimal optomechanical coupling strength in multi-membrane systems, journal, 2019.
- [74] WINDEY, D.; GONZALEZ-BALLESTERO, C.; MAURER, P.; NOVOTNY, L.; ROMERO-ISART, O. ; REIMANN, R. **Physical Review Letters**. Cavity-based 3d cooling of a levitated nanoparticle via coherent scattering, journal, v.122, n.12, mar 2019.
- [75] TEBBENJOHANNNS, F.; FRIMMER, M.; MILITARU, A.; JAIN, V. ; NOVOTNY, L. **Physical Review Letters**. Cold damping of an optically levitated nanoparticle to microkelvin temperatures, journal, v.122, n.22, jun 2019.
- [76] DIEHL, R.; HEBESTREIT, E.; REIMANN, R.; TEBBENJOHANNNS, F.; FRIMMER, M. ; NOVOTNY, L. **Physical Review A**. Optical levitation and feedback cooling of a nanoparticle at subwavelength distances from a membrane, journal, v.98, n.1, jul 2018.